Neurovascular Coupling in the Basolateral Amygdala Modulates Negative Emotions

Jiayu Ruan[1, 2, 3, 5], Xinghua Quan[3], Huiqi Xie[3], Yiyi Zhang[3], Dongdong Zhang[2], Wentao Wang[3], Bingrui Zhao[3], Danping Lu[2], Yuxiao Niu[6], Mengyuan Diao[7], Wei Hu[7], Jie-Min Jia[2, 3, 4, 5*]

Affiliations

[1]College of Life Sciences, Zhejiang University, Hangzhou, Zhejiang, China.

[2]Westlake Laboratory of Life Sciences and Biomedicine, Hangzhou, China.

[3]Laboratory of Neurovascular Biology, School of Life Sciences, Westlake University, Hangzhou, China.

[4]State Key Laboratory of Gene Expression, School of Life Sciences, Westlake University, Hangzhou, Zhejiang, China.

[5]Laboratory of Neurovascular Biology, Institute of Basic Medical Sciences, Westlake Institute for Advanced Study, Hangzhou, China.

[6]Laboratory of Computational and Functional Genomics, School of Life Sciences, Westlake University, Hangzhou, China

[7]Department of Critical Care Medicine, Affiliated Hangzhou First People's Hospital, School of Medicine, Westlake University, Hangzhou, China.

*Correspondence: jiajiemin@westlake.edu.cn

ABSTRACT

Emotion induces changes in regional cerebral blood flow (CBF), a manifestation of neurovascular coupling (NVC), yet whether NVC might feed back to modulate emotion actively remains unexplored. Here, we demonstrate that NVC actively and bidirectionally modulates stress-induced negative emotions. We established bidirectional manipulations of NVC in freely moving mice by employing integrated pharmacological, genetic, and arteriolar optogenetic approaches. Our results showed that both systemic and basolateral amygdala (BLA) region-specific NVC deficiencies heightened emotional responses when mice transitioned from a safe, familiar environment to anxiogenic environments, and local restoration of NVC in the BLA normalized these responses. Mechanistically, NVC dysfunction impairs the capacity of BLA neuronal scaling during state transitions, manifesting as a characteristic biphasic pattern of c-Fos topology. Namely, the NVC-deficient animal aberrantly adopts high-stress configurations under mild stress but regresses to low-stress templates during high-demand survival threats, thereby compromising defensive sustainability. Notably, the genetic NVC-enhancement model counteracts NVC impairments caused by chronic stress, thereby alleviating stress-driven emotional distress. These findings established NVC in the BLA as an allostatic program that fine-tunes neural circuit activity for emotional responses, with implications for understanding and treating emotional disorders.

INTRODUCTION

Emotion is a complex, integrative response to changes in internal and external environments.[1] Emotional flexibility—the capacity to dynamically regulate and adapt these responses—is fundamental for mental health and survival.[2] Conversely, deficits in this adaptive capacity result in emotional rigidity, a hallmark of dysregulation strongly associated with psychiatric disorders such as depression and post-traumatic stress disorder (PTSD).[3, 4] Therefore, delineating the molecular and cellular mechanisms that govern the balance between emotional flexibility and rigidity is critical for elucidating the biological basis of resilience.[5, 6]

Neurovascular coupling (NVC), the core physiological foundation of blood oxygen level-dependent (BOLD) functional MRI (fMRI) signals, has long been categorized as a passive neural proxy.[7-10] Clinical observations in the basolateral amygdala (BLA)—a pivotal hub for processing negative affect—reveal pervasive neurovascular dysregulation across diverse psychiatric landscapes.[11] Specifically, exaggerated BOLD responses occur in post-traumatic stress disorder (PTSD), bipolar disorder, high body mass index (BMI), and early-life stress-exposed cohorts;[8, 12-15] In contrast, autosomal recessive Urbach-Wiethe disease, stemming from *ECM1* (coding extracellular matrix protein 1) gene mutations, is marked by a lack of hemodynamic responsiveness: Such patients exhibit BLA vascular perturbations leading to localized calcification, alongside a selective deficit in fear perception when confronted

with threat.[16, 17]

Consistent with this clinical phenotype, NVC impairments are recapitulated in animal models, where acute, chronic, and neuroendocrine stressors significantly impair NVC fidelity within stress-sensitive circuits.[18-20] Yet, a fundamental question of causality remains: do these deficits merely reflect secondary consequences of neuronal dysfunction, or do they actively drive emotional pathology?

Emerging evidence indicates that vascular-derived cues actively modulate diverse neural processes. For instance, nitric oxide generated during NVC promotes adult hippocampal neurogenesis,[21] while vascular-derived nitric oxide depolarizes the membrane potential of the optic nerve.[22] In the hypothalamus, salt-loading-induced vasoconstriction during NVC exerts positive feedback to boost local parvalbumin interneuron activity.[23] Additionally, whole-cell patch recordings in brain slices demonstrate that altered parenchymal arteriolar tone modulates nearby neuronal firing–decreasing pyramidal neuron activity and increasing interneuron activity, with effects depending on the mechanosensitive cation channel.[24] These observations imply that NVC possesses an intrinsic capacity, likely via chemical and/or mechanical cues, to actively regulate neural circuits, extending beyond its traditional role in metabolic support.[25]

However, its potential as a real-time gatekeeper of emotional circuitry remains unexplored. To address this gap, we investigated NVC within the BLA

as a model system. We hypothesize that BLA NVC functions as a critical regulatory checkpoint that calibrates the intensity of negative emotions, thereby maintaining emotional flexibility.[26]

In this study, employing a multidimensional emotion assessment framework combined with cell-type-specific genetic manipulations and arteriolar optogenetics, we demonstrate that NVC in the BLA actively and bidirectionally modulates emotional reactivity. Unlike its non-contribution in the somatosensory barrel cortex (S1BF), we reveal that neurovascular decoupling in the BLA precipitates emotional rigidity—a maladaptive state defined by a collapse in the dynamic range of emotional responses—manifesting as a distinctive biphasic dysregulation where physiological and behavioral outputs are pathologically exaggerated under mild stress, yet paradoxically blunted under intense stress. Mechanistically, we demonstrate that this behavioral rigidity is underpinned by corresponding biphasic shifts in BLA neural activity across graded stressors. Notably, the enhanced NVC model confers emotional resilience against chronic stress by normalizing BLA neural circuit activity. These findings establish NVC as an intrinsic regulatory gain controller in emotional processing and suggest that targeting circuit-specific neurovascular communication offers a novel therapeutic strategy for psychiatric dysregulation.

RESULTS

Validation of a quantitative behavioral framework linking graded BLA activation to escalating spatial stress levels

To dissect the neurovascular mechanisms actively modulating emotion, we first established a robust, quantifiable behavioral paradigm that scales linearly with stress intensity. We exposed male age-matched wild-type (*WT*) mice to contexts for 15 min with graded anxiogenic potential: the home cage (HC; minimal stress), the 40 cm, 35 cm, and 10 cm open field tests (OFTs; mild-to-moderate stress), and acute restraint stress (ARS; intense stress) (Fig. 1a).[27-31] We verified BLA neuronal activation 90 min post-assay by assessing c-Fos expression (Fig. 1b). Immunofluorescence mapping revealed that c-Fos intensity increased in a stress-dependent manner (Fig. 1c). Crucially, this graded BLA activation was mirrored by a stepwise increase in defecation bouts (Fig. 1d), showing a robust linear correlation with BLA c-Fos intensity (R = 0.8160, P < 0.0001; Fig. 1e). Furthermore, we quantified serum corticosterone levels, the primary stress-responsive glucocorticoid in rodents, in a parallel cohort of mice at 5 min post-assay (Fig.1a). Serum corticosterone concentrations exhibited a stress-dependent trend mirroring that of BLA neural c-Fos (Fig. 1f). Likewise, defecation bouts also showed a strong positive correlation with serum corticosterone concentrations (R = 0.7765, P = 0.0004; Fig. 1g). Collectively, these results establish defecation as a reliable, robust, and non-invasive marker that accurately tracks systemic and spatially graded

128 stress levels in free-moving live mice.[31-33]

129 Reducing the arena size from 40 cm to 35 cm prominently increased
130 defecation bouts (Fig. 1d). Although the shift in linear dimensions from 40 cm
131 to 35 cm appears modest, this modification represents a ~33% reduction in total
132 cubic volume, significantly intensifying the degree of spatial confinement.[34] This
133 compressed environment provoked a more potent stress state than the 40 cm
134 OFT, characterized by a multi-dimensional escalation in BLA c-Fos density (Fig.
135 1c), serum corticosterone levels (Fig. 1f), locomotor activity (Fig. 1h), coupled
136 with reductions in classic readouts of exploration, specifically center time (Fig.
137 1i) and unsupported rearing (Fig. 1j). Spatial mapping further revealed that
138 more than 90% of defecation behavior in the 40 cm OFT occurred in the
139 peripheral zone, consistent with thigmotaxis behavior (Fig. 1k, l).[27, 35] Together,
140 converging behavioral, neural, and hormonal readouts confirm that the 35 cm
141 OFT elicits a stronger stress response than the standard 40 cm OFT.[36]

142 To determine whether BLA neuronal activity is necessary for this response,
143 we chemogenetically silenced BLA excitatory neurons using the inhibitory
144 DREADD hM4Di (Fig. 1m).[37] In mice expressing hM4Di in BLA excitatory
145 neurons treated with the agonist C21 effectively blunted stress-induced BLA c-
146 Fos expression in ARS (Fig. 1n, o). Intriguingly, this also suppressed defecation
147 bouts in both the 40 cm OFT and ARS contexts compared to vehicle-treated
148 control mice (Fig. 1p). Furthermore, BLA silencing significantly reduced the
149 defecation rate (the incidence of mice that defecated) and prolonged the

150 defecation latency (the time elapsed before the production of the first fecal
151 pellet) (Fig. 1q) in the 40 cm OFT. Interestingly, neither center preference nor
152 locomotor activity was altered in the 40 cm OFT following chemogenetic
153 inhibition of the BLA (Fig. 1r-s). Control mice expressing EGFP alone (sham
154 group) exhibited no alterations in defecation metrics (Fig. 1q, t).

155 Collectively, these data establish a validated, BLA-dependent quantitative
156 framework—the "negative emotion indices"—encompassing BLA neural
157 activation, multi-dimensional defecation metrics (bouts, rate, latency),
158 unsupported rearing, and serum corticosterone concentration to dynamically
159 assess emotional states.

160

161 **A genetic model of cerebral SMC-specific GluN2D deficiency exhibits BLA**
162 **neurovascular decoupling**

163 Equipped with this multi-dimensional assessment framework, we next sought
164 to identify the specific molecular substrates within the BLA neurovascular unit
165 (NVU) that govern these emotional responses. We previously identified that the
166 core N-methyl-D-aspartate (NMDA) receptor subunit GluN1 (encoded by *Grin1*)
167 in smooth muscle cells (SMCs) is essential for NVC at the neuro-smooth
168 muscle junction (NsMJ; Fig. 2a),[38] but the other regulatory NMDA subunits in
169 SMCs remained to be characterized. To address this, we screened mRNA
170 expression of all NMDA receptor subunits in cultured SMCs sorted from

171 postnatal day 0 (P0) brain parenchymal tissue and identified *Grin2d* (encoding
172 GluN2D) as the sole regulatory subunit detectably expressed (Fig. 2b). High-
173 resolution RNAscope further confirmed that *Grin2d* colocalized specifically with
174 SMC markers in cerebral arterioles with high colocalization coefficients
175 (visualized via *SMA-creER:Ai14* reporter mice; Fig. 2c). To rigorously validate
176 the specificity of our RNAscope probes, we leveraged the well-documented
177 developmental divergence of NMDA subunits in the cerebellum as an internal
178 biological control. We exploited the distinct trajectories where *Grin1* expression
179 increases from P0 to P60, while *Grin2d* expression follows a reciprocal
180 decline.[39, 40] Our probes accurately recapitulated these age-dependent patterns,
181 thereby confirming their high target specificity (Supplementary information, Fig.
182 S1a, b). This biological validation was further extended to the protein level; our
183 anti-GluN2D antibody successfully distinguished the differential GluN2D protein
184 abundance between P0 and P60 stages in cerebellum tissue, mirroring the
185 transcriptomic data (Supplementary information, Fig. S1c).

186 Using this validated antibody, immunofluorescence analysis of isolated
187 middle cerebral arteries (MCA) (Fig. 2d, e) and cultured SMCs sorted from P0
188 brain parenchymal tissue (Supplementary information, Fig. S1d) confirmed the
189 specific ablation of GluN2D in the cerebral SMCs in *SMA-creER:Grin2d*$^{f/f}$
190 (*Grin2d*-cKO) mice. Furthermore, Western blot analysis of whole-cortical
191 lysates revealed that *Grin2d*-cKO did not affect GluN2D expression in other
192 non-SMC populations (Supplementary information, Fig. S1e), confirming the

193 cell-type specificity of our genetic model. To assess the global impact of this
194 genetic depletion, we examined GluN2D expression in the SMCs of peripheral
195 organs, including the heart, liver, spleen, lung, kidney, intestine, and bladder
196 (Supplementary information, Fig. S2a). Notably, GluN2D expression seemed
197 restricted to cerebral SMCs and absent in these peripheral tissues' SMCs,
198 suggesting that our *Grin2d*-cKO model exerts a brain-restricted impact
199 (Supplementary information, Fig. S2b, c). Furthermore, we systematically
200 verified the physiological status of *Grin2d*-cKO mice; no differences were
201 observed in systemic metabolic homeostasis (Supplementary information, Fig.
202 S3a-g), blood pressure (Supplementary information, Fig. S3h), gastrointestinal
203 function (Supplementary information, Fig. S3i-n), and blood-brain barrier (BBB)
204 integrity[41, 42] (Supplementary information, Fig. S3o-p) compared to littermate
205 controls. Finally, we assessed key contractile proteins, finding that α-SMA and
206 smoothelin expression remained unaltered (Supplementary information, Fig.
207 S4). These data demonstrate that the basic metabolic functions,
208 gastrointestinal system, and basic contractile structural integrity of SMCs are
209 preserved in *Grin2d*-cKO mice.

210 To assess the functional impact of SMC-specific *Grin2d* deletion and
211 facilitate a direct, one-to-one comparison with our previously reported *Grin1*-
212 cKO model, we employed the same classical paradigm: measuring whisker
213 stimulation-evoked hemodynamic responses in the somatosensory barrel
214 cortex (S1BF) (Fig. 2f).[38] Consistently, *Grin2d*-cKO mice exhibited a ~66%

215 attenuation in functional hyperemia upon whisker stimulation (Fig. 2g),
216 confirming that GluN2D is functionally comparable to GluN1 in regulating
217 cerebral NVC. Control experiments confirmed that tamoxifen administration
218 alone in *Grin2d*$^{f/f}$ mice did not alter NVC responses (Supplementary information,
219 Fig. S5).

220 Having established the NVC deficit in the cortex, we sought to determine
221 whether this NVC dysfunction extends to the BLA. To this end, we developed a
222 *de novo* system based on previous strategies[43, 44] to simultaneously record
223 neuronal activity and blood supply within the BLA of freely moving mice, thereby
224 enabling direct assessment of NVC. First, we mapped the BLA arteriolar
225 topology by superimposing 3D-reconstructed arterioles in the tissue-cleared
226 brain on a schematic cerebral vasculature. This analysis identified that the
227 corticoamygdaloid artery (coamg) penetrates the BLA, making it suitable for
228 photometric monitoring (Supplementary Information, Fig. S6, Video S1).
229 Second, we validated the fidelity of our cerebral blood volume (CBV) recording
230 method: fiber photometry-based blood plasma fluorescence intensity recording
231 locally in the BLA showed a robust linear correlation with orbital Rhodamine
232 injection concentration (Supplementary information, Fig. S7a, b; $R = 0.8946$, P
233 < 0.0001). Signal stability was achieved 15 min post-injection (Supplementary
234 information, Fig. S7c), and this time point was designated as the initiation time
235 for the behavior assay.

236 Using this optimized paradigm, after tamoxifen administration, we injected

237 *AAV2/9-hSyn-GCaMP8f* into the BLA and implanted optic fibers at the injection
238 site two weeks before the recordings. After three days of habituation (one trial
239 per day for a continuous 3-day period), we monitored NVC during the 40 cm
240 OFT (Fig. 2h-k). Consistent with our earlier c-Fos data (Fig. 1c), the 40 cm OFT
241 elicited robust BLA Ca^{2+} transients that were temporally matched by CBV
242 elevations, indicating tight local NVC in littermate control mice (Fig. 2i-k). In
243 contrast, *Grin2d-cKO* mice exhibited a dissociated neurovascular phenotype,
244 where augmented BLA neuronal Ca^{2+} signals were paradoxically paired with a
245 blunted hemodynamic response (Fig. 2i-k). This inverse pattern—hyperactive
246 neurons coupled with hypoperfused blood supply—was further corroborated by
247 increased c-Fos expression in the BLA 90 min post-assay (Fig. 2l, m).
248 Furthermore, we confirmed that the observed attenuation in functional
249 hyperemia was not attributable to differences in basal perfusion, locomotor
250 activity, or spatial preference within the 40 cm OFT (Supplementary information,
251 Fig. S8)

252 Collectively, these findings demonstrate robust NVC within the BLA during
253 40 cm OFT exposure and validate that SMC-specific *Grin2d*-cKO mice exhibit
254 an NVC deficit in this region.

255

256 **BLA-target pharmacological restoration of NVC reversed emotional**
257 **hyper-reactivity in *Grin2d-cKO* mice under mild stress**

258 Building on the BLA's established role as one of the central hubs for stress
259 responses, we next utilized our negative emotion indices (Fig. 1) to evaluate
260 whether the BLA neurovascular decoupling observed in *Grin2d*-cKO mice (Fig.
261 2) results in behavioral and physiological impairments. Notably, we observed
262 that *Grin2d*-cKO mice exhibited a ~12-fold increase in defecation bouts during
263 the first 5 min of the 40 cm OFT, a trend sustained throughout the session (Fig.
264 3a). This phenomenon was not observed in the home cage context
265 (Supplementary information, Fig. S3c-e, n). Littermate control mice (*Grin2d*$^{f/f}$)
266 displayed a graded increase in defecation bouts in response to escalating
267 spatial stress, consistent with the pattern observed in *WT* mice (Figs. 1d and
268 3b). In contrast, *Grin2d*-cKO mice failed to show this graded response; instead,
269 they exhibited an abrupt rise to a maximal plateau level of defecation bouts, a
270 response typically elicited by intense ARS stress (Fig. 3b). This hyper-reactivity
271 was further reflected in an increased defecation rate, reduced latency (Fig. 3c),
272 a more than 3-fold reduction in unsupported rearing, and a ~1.3-fold increase
273 in serum corticosterone levels in the 40 cm OFT (Fig. 3d). Importantly, basal
274 stress levels in the home cage remained indistinguishable between genotypes
275 (Supplementary information, Fig. S9a). Altogether, *Grin2d*-cKO mice displayed
276 a unified shift across multiple-dimensional stress metrics, indicating a robust,
277 exaggerated negative emotional response to mild stressors, such as those
278 encountered in OFTs.

279 Given that *Grin2d*-cKO mice showed NVC dysfunction beyond the BLA, to

280 determine the contribution of BLA local NVC in hyper-reactivity, we employed
281 administration of HET0016, a selective inhibitor of CYP450ω-hydroxylases that
282 suppresses the synthesis of 20-HETE (a potent vasoconstrictor), thereby
283 facilitating vasodilation to compensate for the NVC deficit.[45, 46]

284 To strictly validate the pharmacological efficacy of HET0016 before its site-
285 specific delivery to the BLA, we first replicated the systemic administration
286 protocol described in our previous study.[38] Systemic HET0016 administration
287 dose-dependently reduced ARS-induced defecation bouts (Supplementary
288 Information, Fig. S10a). This behavioral rescue provided a clear rationale for
289 selecting 1 mg/kg as the optimal dose for subsequent investigations. Under this
290 condition, we confirmed that 1 mg/kg HET0016 produced a ~3-fold increase in
291 whisker-evoked functional hyperemia amplitude in the S1BF compared with
292 saline controls (Supplementary Information, Fig. S10b, c)

293 Notably, HET0016 effectively rescued the hyper-reactive phenotype in
294 *Grin2d*-cKO mice, both in systemic (Fig. 3e-j) and local (Fig. 3k-p)
295 administrations in the 40 cm OFT. Both administration routes effectively
296 normalized BLA neural activation and multi-dimensional defecation metrics—
297 including bouts, rate, and latency—to littermate control levels (Fig. 3f-i and l-o).
298 Importantly, this vascular intervention also significantly normalized unsupported
299 rearing bouts and reduced serum corticosterone concentrations (Fig. 3j and p)
300 in the 40 cm OFT. In contrast, in the home cage, neither systemic nor BLA local
301 HET0016 impacted serum corticosterone levels (Supplementary information,

302 Fig. S9b, c).

303 Collectively, local pharmacological compensation in the BLA sufficiently
304 normalized the hyper-reactivity features in the *Grin2d*-cKO genetic model,
305 despite NVC deficits in other brain regions, thereby establishing that intact NVC
306 in the BLA is essential for maintaining appropriate emotional responses to mild
307 stress.

308 We observed consistent behavioral phenotypes in the 40 cm OFT across
309 various mechanistically distinct models of NVC dysfunction, each targeting
310 different nodes of the NVU (Supplementary information, Fig. S11, S12).
311 Specifically, either perturbing upstream neural signaling (*Emx1-cre:Ptgs2*$^{f/f}$)
312 (Supplementary information Fig. S11a-h, and S12o-p)[47-49] or disrupting the
313 neurovascular interface–achieved via pan-mural cell-specific *Grin2d*-cKO
314 (*Pdgfrβ-creER:Grin2d*$^{f/f}$) or SMC-specific *Grin1-Grin2d* double-cKO (*SMA-*
315 *creER:Grin1*$^{f/f}$*:Grin2d*$^{f/f}$) (Supplementary information Fig. S11i-r and S12o-p)–
316 consistently recapitulated the NVC deficits and behavioral phenotypes
317 observed in the primary *Grin2d*-cKO mice in the 40 cm OFT (Fig. 2, 3).

318 To ultimately disturb contractile protein machinery within SMC, we targeted
319 the *Acta2* gene (encoding α-SMA).[50, 51] This model (*Pdgfrβ-creER:Acta2*$^{f/f}$ mice,
320 shorten as *Acta2*-cKO) indistinguishably mirrored the hyper-reactive
321 phenotypes of the signaling-deficient models in the 40 cm OFT (Supplementary
322 information, Fig. S11s-v, x-aii, and S12o, p). Surprisingly, a high-fat diet

323 (HFD)—known to diminish NVC in both animals and humans via multiple
324 factors[14, 52]—produced an identical phenotype of *Grin2d*-cKO mice in the 40 cm
325 OFT (Supplementary information, Fig. S12a-d, g-h, j-n, o, and p). These
326 findings indicate that this emotional hyper-reactivity was not restricted to the
327 single *Grin2d*-cKO model but represented a universal consequence of
328 neurovascular dysfunction within the 40 cm OFT, reinforcing the universality of
329 NVC-driven emotional dysregulation.

330 Although local HET0016 delivery to the BLA successfully restored
331 emotional metrics in other models (Fig. 3k-p, Supplementary information, Fig.
332 S12i-n) in the 40 cm OFT, it failed to produce similar effects in *Acta2*-cKO mice
333 (Supplementary information, Fig. S11w-aii) in the same context. This indicates
334 that once the downstream contractile apparatus is disrupted, upstream
335 regulators are unable to exert their regulatory functions. Finally, we confirmed
336 that these convergent effects did not involve BBB leakage (Supplementary
337 information, Fig. S3o, p; S12e, f).[53] Together, these findings establish that NVC
338 integrity per se is indispensable for emotional homeostasis.

339

340 **Caldesmon acts as the downstream effector of GluN2D in NVC thereby**
341 **modulating emotional reactivity**

342 Given that direct disruption of the vascular contractile apparatus (*Acta2*-cKO)
343 phenocopies the emotional hyper-reactivity of *Grin2d*-cKO mice (Fig. 3;

344 Supplementary information, Fig. S11; Fig. S12), we hypothesized that GluN2D
345 couples to the SMC cytoskeletal machinery. To this end, we performed co-
346 immunoprecipitation (Co-IP) followed by mass spectrometry to map the
347 GluN2D interactome in vascular SMCs. This unbiased screen identified
348 caldesmon (encoded by *Cald1*), an actin-binding protein critical for regulating
349 actomyosin contractility, as a top candidate enriched in *Vascular Smooth*
350 *Muscle Contraction* pathway (Fig. 4a).[54, 55] This physical association between
351 GluN2D and caldesmon was further confirmed by Western blotting of the
352 immunoprecipitated complex (Fig. 4b).

353 Caldesmon serves as a "blocker" on smooth muscle cells' contraction; its
354 disruption is predicted to impair cross-bridge cycling and thereby compromise
355 NVC. To test this, we employed siRNA-mediated knockdown (KD). Unlike
356 GluN2D, caldesmon expression was restricted exclusively to vascular mural
357 cells (Fig. 4c–e),[56] allowing for vascular-specific manipulation without the risk
358 of direct neuronal off-target effects. We validated the efficacy and spatial
359 specificity of this approach: both whole-brain and local BLA siRNA delivery
360 robustly reduced caldesmon expression in background-matched groups (both
361 established in *Grin2d*$^{f/f}$ mice) (Fig. 4f-i). Crucially, gene silencing was spatially
362 restricted to the injection site with anatomical precision: local BLA *Cald1* KD did
363 not impact caldesmon levels in the adjacent Ventromedial Hypothalamus (VMH)
364 (Fig. 4g–i), nor did S1BF-restricted *Cald1* KD alter expression in the BLA
365 (Supplementary information, Fig. S13).

366 Functionally, local S1BF *Cald1* KD—but not local BLA *Cald1* KD—
367 attenuated whisker-evoked functional hyperemia in the barrel cortex (Fig. 4j, k),
368 confirming *Cald1* KD as an effective tool for disrupting NVC with regional
369 precision. We then focused on the emotional circuit. Behaviorally, both whole-
370 brain and local BLA *Cald1* KD recapitulated the hyper-reactive phenotype of
371 *Grin2d*-cKO mice in the 40 cm OFT: *Cald1* KD mice exhibited exaggerated
372 negative emotional responses, characterized by BLA neuronal hyperactivation
373 (c-Fos), reduced unsupported rearing, elevated serum corticosterone
374 concentrations, and intensified defecation dynamics (increased bouts/rate,
375 decreased latency) (Fig. 4l–q). In contrast, local S1BF *Cald1* KD did not alter
376 the above parameters, confirming regional specificity (Supplementary
377 information, Fig. S14).

378 To elucidate the functional relationship between GluN2D and caldesmon,
379 we applied the local BLA *Cald1* KD approach in *Grin2d*-cKO mice. This
380 epistasis analysis showed no additive phenotype (Fig. 4l-q), suggesting that
381 caldesmon likely functions downstream of GluN2D within a hierarchical
382 vascular signaling cascade. Together, these results identify caldesmon as a
383 critical effector linking GluN2D to SMC contractility and demonstrate that
384 localized NVC deficits in the BLA–despite intact NVC in other brain regions–are
385 sufficient to impair emotional responses to mild stress.

386

387 **BLA arteriolar SMCs' optogenetic suppression of NVC precipitates**
388 **negative emotional states under conditions of mild and negligible stress**

389 To achieve acute suppression of NVC within a millisecond timescale–
390 unattainable through genetic or pharmacological manipulations–we employed
391 an SMC-optogenetic approach to reversibly "clamp" vascular diameter.[57]

392 We generated SMC-specific ChR2-expressing mice (*SMA-creER:Ai32;* Fig.
393 5a) and optimized a fiber-optic setup to locally activate BLA SMCs while
394 simultaneously monitoring regional CBV (Fig. 5b). In the home cage under
395 minimal external stress, we optimized a protocol that reliably induced a
396 consistent ~3% CBV decrease (Fig. 5c red line). This hemodynamic
397 manipulation was rapid and reversible (Fig. 5d).

398 Consistent with earlier data obtained from *Grin2d*$^{f/f}$ mice (blue line in Fig.
399 2i, blue line), the stress during the 40 cm OFT elicited functional hyperemia in
400 an independent cohort of *SMA-creER:Ai47* (EYFP) mice (Fig. 5e-g, green line).
401 Optogenetic clamping of BLA arterioles partially blocked this hemodynamic
402 response (Fig. 5e–g, red line). Furthermore, power spectral density analysis of
403 the hemodynamic traces revealed a significant reduction in blood flow power
404 across low-frequency bands—typically associated with vascular vasomotion—
405 during optogenetic stimulation (Supplementary information, Fig. S15). This
406 suppression of spectral energy confirms that optogenetic clamping effectively
407 stabilized vascular diameter.

408 This acute NVC suppression precipitated an emotional shift: ChR2-EYFP
409 mice exhibited an exacerbation of negative emotional responses, characterized
410 by markedly increased BLA neural activation (Fig. 5h, i), reduced unsupported
411 rearing (Fig. 5j), and elevated serum corticosterone concentrations (Fig. 5k),
412 and shifted defecation metrics (Fig. 5l, m) in the 40 cm OFT. These alterations
413 were consistent with the *Grin2d*-cKO phenotype (Fig. 3a-d) in the 40 cm OFT.
414 Locomotor activity and center preference remained unaffected, ruling out motor
415 confounds (Supplementary information, Fig. S16a, b) in the 40 cm OFT. This
416 optogenetically driven, temporally controlled suppression of NVC reveals that
417 preventing the stress-induced vascular surge removes a critical physiological
418 component, thereby amplifying negative emotion.

419 Next, we investigated whether BLA-targeted vascular clamp, in the
420 absence of actual external stress, is sufficient to drive stress-like behaviors. We
421 applied the same optogenetic stimulation protocol (~3% CBV decrease) to mice
422 in the safe home cage environment for 15 min (Fig. 5n, o). Strikingly, this
423 hemodynamic mismatch alone was sufficient to induce a stress-like state: While
424 basal defecation was negligible in the home cage (0.23 pellets/15 min),
425 optogenetic stimulation induced a ~6.4-fold cumulative CBV change (Fig. 5o)
426 coupled with a ~10-fold surge in defecation bouts (Fig. 5p). These changes
427 were associated with increased BLA neural activation and elevated serum
428 corticosterone levels (Fig. 5q, r).

429 Crucially, we verified that this optogenetic manipulation did not induce

430 hypoxic injury. Unlike the Stroke Induced by Magnetic ParticLEs (SIMPLE)
431 stroke model[58-60] which triggers robust HIF-1α upregulation, our optogenetic
432 protocol elicited no obvious HIF-1α response after optogenetic stimulation in
433 the home cage (Supplementary information, Fig. S16c, d). This confirms that
434 the observed behavioral shifts stem from functional neurovascular modulation,
435 not ischemic stroke or tissue hypoxia.

436

437 **NVC dysfunction conversely exhibited hyporeactivity under high-**
438 **intensity stress**

439 Our findings from the standard 40 cm OFT established that NVC dysfunction
440 precipitates a hyper-reactive, anxiety-like state under mild stress (Fig. 3). We
441 next characterized how the NVC-deficient BLA responds to imminent, life-
442 threatening high-intensity stress.[61] To this end, we employed two paradigms: a
443 looming assay[62] and a virtual reality (VR_{eagle}) simulation of a diving eagle[63], both
444 of which mimic an approaching aerial predator.

445 Prior to looming stimulation, basal locomotor activity was comparable
446 between groups (Fig. 6a, blue region; Supplementary information, Fig. S17a).
447 Upon stimulus, both groups exhibited immediate and robust freezing (Fig. 6a,
448 yellow region), confirming that NVC dysfunction did not impair sensory
449 detection, threat evaluation, or the initiation of defensive strategies.[64]

450 However, a striking divergence emerged during the maintenance phase:

451 while control mice sustained a prolonged freezing state, *Grin2d*-cKO mice
452 exhibited a “premature exit” phenotype (Fig. 6b). Velocity heatmaps confirmed
453 that *Grin2d*-cKO mice resumed locomotor activity significantly earlier than
454 controls (Fig. 6b, c). This behavioral collapse was mirrored by an inappropriate
455 increase in unsupported rearing bouts—a high-risk behavior exposing the
456 animal to recurring predation—immediately following stimulus termination (Fig.
457 6d). This dissociation (intact initiation but shortened maintenance) in free-
458 moving mice underscores the critical role of NVC in sustaining defensive states.

459 The second life-threatening paradigm, virtual reality (VR_{eagle}) eagle,
460 allowed for head-fixed monitoring of pupil diameter in awake mice—a robust
461 index of autonomic arousal[65]—alongside locomotor activity on a float ball (Fig.
462 6e). Baseline metrics (pupil diameter and locomotor activity) were
463 comparable between genotypes (Supplementary information, Fig. S17b, c).
464 Upon exposure to the eagle call (0–1.5 s, Figure 6f blue region) and visual
465 dive (1.5–3 s, Figure 6f yellow region), both groups exhibited robust defensive
466 engagement, characterized by immediate freezing and sharp pupil dilation
467 sustained throughout the stimulus (0–3 s, Fig. 6f; Supplementary information,
468 Fig. S17d and Video S2). This confirms that sensory processing and fear
469 initiation remain preserved in *Grin2d*-cKO mice, consistent with observations
470 made in the looming assay.

471 However, a striking divergence emerged during the “defensive offset
472 phase”, defined as the interval from stimulus termination to the intersection

473 of pupil diameter and locomotion speed in tracing plots for the recovery period
474 (Fig. 6f, double-arrows lines). While littermate control mice maintained high
475 arousal, *Grin2d*-cKO mice exhibited a rapid collapse of the defensive state
476 (Fig. 6g). Moreover, the recovery time for pupil diameter back to baseline was
477 reduced by ~59% in *Grin2d*-cKO mice, consistent with the accelerated
478 recovery time of locomotion speed observed in the looming assay (Fig. 6h).
479 Collectively, these two independent paradigms demonstrate that NVC-
480 deficient mice cannot physiologically sustain high-load fear states.

481 To establish an intermediate stress condition between the OFTs and a
482 life-threatening predator scenario (looming and VR_{eagle}), we modified the
483 standard OFT to create a complex OFT (c-OFT). This modification involved
484 the addition of a metal fence barrier that separated an aversive start zone
485 (white floor) from a safe zone (black floor) (Fig. 6i).[29] c-Fos mapping of
486 littermate controls revealed that c-OFT paradigm indeed represented an
487 intermediate level of BLA activation, which fell between the mild stress elicited
488 by the OFTs and the intense stress induced by predator simulation (Fig. 6j,
489 blue line). In contrast, c-Fos mapping in *Grin2d*-cKO mice demonstrated
490 exaggerated neural activation under mild stress yet blunted activation under
491 intense stress, matching their corresponding behavioral phenotypes (Fig. 6j,
492 magenta line).

493 Notably, under the intermediate c-OFT condition, one-dimensional
494 analysis of c-Fos density failed to correlate with the observed heighted

495 defecation bouts in *Grin2d*-cKO mice (Fig. 6k). This discrepancy prompted us
496 to extend beyond simple intensity quantification and conduct further analyses
497 of the topological distribution patterns of c-Fos positive neurons within the
498 BLA (Fig. 6l-m; supplementary information, S18).

499 We therefore decoded c-Fos topology using the structural similarity index
500 measure (SSIM) and unbiased clustering to dissect BLA ensemble
501 configurations (Fig. 6l, m). In littermate controls, BLA topology exhibited
502 dynamic "stress scaling": activation patterns evolved distinctly from minimal
503 (Level 0) to high-threat states (Level 3), forming a precise structural hierarchy
504 (Fig. 6l). In contrast, *Grin2d*-cKO ensembles displayed topological
505 disorganization and a lack of hierarchy (Fig. 6m).

506 Mapping *Grin2d*-cKO neural SSIM signatures against the structural
507 hierarchy of littermate control mice revealed a striking inversion of emotional
508 scaling (Supplementary information, Fig. S18b-g): Under mild stress (OFTs),
509 *Grin2d*-cKO patterns aberrantly clustered with high-threat control templates
510 (Levels 2 and 3), providing a topological explanation for their hyper-reactivity
511 (Supplementary information, Fig. S18d, e). Conversely, under high load
512 (looming, VR_{eagle}), these patterns failed to scale appropriately and instead
513 regressed to low-stress templates (Level 1), underpinning their functional
514 collapse (Supplementary information, Fig. S18f, g). Specifically, hierarchical
515 clustering revealed that the *Grin2d*-cKO topological signature under c-OFT
516 aberrantly converged with that of control mice under ARS, rather than their

517 stage-matched controls. This pathological shift was absent in the home cage,
518 where topologies of both genotypes remained tightly clustered
519 (Supplementary information, Fig. S18b, c). These findings reveal that BLA
520 NVC deficiency decouples behavior from c-Fos intensity by inducing a
521 nuanced reconfiguration of BLA neural topology.

522 Collectively, these data reveal a stress load-dependent biphasic pattern
523 (Supplementary information, Fig. S18h): NVC dysfunction precipitates
524 topological hyper-reactivity under low stress load (OFTs) but leads to hypo-
525 sustainability under high stress load (looming and VR_{eagle}), demonstrating
526 that functional NVC is indispensable for the topological scaling of neural
527 networks during state transitions.

528

529 **Genetic NVC-enhancement model of *Glrb*-cKO mice**

530 Our preceding findings established that the cation-permeable NMDA receptor
531 (GluN2D) acts as the essential "accelerator" for NVC. Its deficiency disrupts
532 NVC, locking the brain into a state of behavioral rigidity—manifested as hyper-
533 reactivity under mild stress yet functional collapse under high load contexts.
534 Guided by the fundamental principle of electrochemical balance, we
535 hypothesized that if cation influx drives NVC, a converse mechanism mediated
536 by anion channels might functionally restrict hemodynamic gain. Consequently,
537 inhibiting such anionic "brakes" could theoretically potentiate NVC and confer

538 emotional resilience.

539 To identify these regulators, we screened transcriptomic databases for
540 anion channels enriched in mural cells.[56] This unbiased screen identified *Glrb*
541 (encoding the chloride-permeable glycine receptor subunit beta, GlyRβ) as the
542 top candidate (Supplementary information, Fig. S19)[56]. RNAscope and
543 immunofluorescence mapping revealed a distinct spatial segregation: *Glrb*
544 (GlyRβ) was predominantly expressed in venous SMCs (vSMCs) (Fig. 7a–d).
545 We validated this expression pattern using *Pdgfrβ-CreER:Glrb*$^{f/f}$ (*Glrb*-cKO)
546 mice, which exhibited a significant reduction in mural *Glrb* (GlyRβ) levels (Fig.
547 7c, e, f). To determine whether these venous receptors are functionally
548 innervated, we examined their molecular and ultrastructural organization:
549 Molecularly, GlyRβ puncta closely colocalized with gephyrin (Fig. 7g), a
550 scaffolding protein essential for clustering inhibitory receptors,[66] suggesting the
551 presence of postsynaptic-like machinery; Structurally, confocal imaging and
552 serial electron microscopy (EM) revealed frequent direct physical contacts
553 between neuronal axons and venular SMCs (Fig. 7h, i). Collectively, these
554 molecular and ultrastructural features provide the morphological substrate for
555 potential neuro-venular communication sites. Unlike the NVC deficit caused by
556 *Grin2d* ablation, *Glrb* deletion resulted in a “super-coupled” state: *Glrb*-cKO
557 mice exhibited significantly enhanced functional hyperemia upon whisker
558 stimulation (Fig. 7j-m). To pinpoint the cellular origin of this enhancement, we
559 performed a genetic dissection. First, deletion restricted to arteriolar SMCs

560 (driven by *SMA-creER*) failed to recapitulate the phenotype (Supplementary
561 information, Fig. S20), ruling out an arteriolar origin. Second, given that GlyRβ
562 is selectively enriched in venular SMCs—and considering the established view
563 that capillaries nearly lack the contractile machinery for active dilation[50]—the
564 enhanced NVC in *Pdgfrβ* mutants is primarily attributable to venular
565 disinhibition. Consequently, the enhanced NVC in *Glrb* mutants suggests that
566 venular GlyRβ may physiologically constrain the magnitude of hemodynamic
567 responses.

568 Given that pharmacological vasodilation (HET0016) successfully rescued
569 the *Grin2d*-cKO phenotype, we hypothesized that genetic removal of *Glrb* could
570 serve as a genetic rescue strategy to counterbalance the *Grin2d* deficit. To test
571 this genetic disinhibition hypothesis, we generated double-knockout mice
572 (*Pdgfrβ-CreER:Grin2d*$^{f/f}$*:Glrb*$^{f/f}$; Fig. 7k). Remarkably, the concomitant deletion
573 of *Glrb* effectively reversed the NVC deficiency triggered by *Grin2d* loss.
574 Whisker stimulation in *Pdgfrβ-CreER:Grin2d*$^{f/f}$*:Glrb*$^{f/f}$ mice elicited functional
575 hyperemia responses comparable to littermate controls (Fig. 7l, m). This result
576 implied that *Glrb*-cKO mimics the effect of HET0016. This finding establishes a
577 genetic paradigm of hemodynamic rescue, demonstrating that venular
578 disinhibition can effectively counterbalance the loss of the arteriolar accelerator.
579 We next asked the fundamental translational question: Does this enhancement
580 of neurovascular coupling confer behavioral resilience against stress?

581

582 **NVC enhancement confers resilience against both acute and chronic**
583 **stress**

584 Given that *Glrb* deletion unlocks a “super-coupled” hemodynamic state (Fig. 7),
585 we first asked whether this vascular enhancement translates into immediate
586 behavioral resilience against acute stress. We subjected mice to ARS. While
587 littermate controls exhibited characteristic stress-induced physiological and
588 behavioral shifts, *Glrb*-cKO mice appeared remarkably stress-buffered. They
589 displayed significantly attenuated BLA neuronal activation (Fig. 8a, b) and
590 blunted serum corticosterone concentrations (Fig. 8c) in ARS. Behaviorally, this
591 physiological resilience was mirrored by stabilized defecation dynamics, with
592 *Glrb*-cKO mice exhibiting significantly fewer defecation bouts in ARS (Fig. 8d).

593 The observation that *Glrb* removal in mural cells confers stress resilience
594 prompted us to investigate whether this NVC-enhancement model could
595 counteract the deficits caused by *Grin2d*-cKO. We found that *Pdgfrβ-*
596 *CreER:Grin2d*$^{f/f}$*:Glrb*$^{f/f}$ mice effectively neutralized the core hyper-anxious
597 phenotype observed in *Grin2d-cKO* mutants (Fig. 8d–j). Specifically, *Pdgfrβ-*
598 *CreER:Grin2d*$^{f/f}$*:Glrb*$^{f/f}$ mice exhibited defecation metrics comparable to NVC-
599 intact littermate controls in ARS and 40 cm OFT (Fig. 8d-f), accompanied by
600 attenuated BLA neural activation (Fig. 8g, h) and a significant increase in
601 unsupported rearing bouts (Fig. 8i) in the 40 cm OFT. Collectively, the
602 observation that *Pdgfrβ-CreER:Grin2d*$^{f/f}$*:Glrb*$^{f/f}$ mice closely resemble NVC-
603 intact mice indicates that emotional reactivity is dynamically calibrated by the

604 precise homeostatic balance between opposing vasoconstrictive and
605 vasodilatory signaling pathways within the BLA.

606 To determine whether the stress resilience observed in systemic mural cell-
607 specific *Glrb*-cKO mice is driven by localized NVC within the BLA, we targeted
608 the disruption of BLA NVC via local delivery of *Cald1* siRNA. In intense ARS,
609 local BLA NVC disruption abolished the resilience-conferring effects typically
610 seen in the *Glrb*-cKO mice, effectively reverting neural, behavioral, and
611 hormonal stress responses to littermate control levels (Supplementary
612 information, Fig. S21a-d). Furthermore, laser speckle contrast imaging (LSCI)
613 revealed that whole-brain knockdown of *Cald1* via cisterna magna delivery did
614 not alter basal CBF at the cortical surface (Supplementary information, Fig.
615 S21e). This indicates that *Cald1* deficiency did not compromise basal vascular
616 integrity, but specifically impairs the vascular response to neuronal activation.

617 While *Glrb* deletion effectively buffers the immediate impact of acute stress,
618 a more rigorous test of neurovascular integrity is whether this protection can
619 sustain itself against chronic adversity. We thus escalated our paradigm to
620 chronic restraint stress (CRS, 3 hours/day for 28 days) (Fig. 8k).[19, 67] We first
621 validated the efficacy of the CRS model in littermate controls, which exhibited
622 a comprehensive state of emotional and physiological exhaustion. Specifically,
623 CRS-treated littermate control mice exhibited significantly attenuated functional
624 hyperemia in S1BF during whisker stimulation (Fig. 7l, m).[19] Concurrently, these
625 mice developed a distinct constipation-like phenotype, characterized by

626 progressive reductions in both defecation frequency and Bristol scores over the
627 28-day stress period (Fig. 8l, m). This was accompanied by classical anxiety-
628 and depression-like behaviors, including significantly reduced time in the open
629 arms of the elevated plus maze (EPM; Supplementary information, Fig. S22a),
630 heightened neural activation in the lateral habenula (LHb; Supplementary
631 information, Fig. S22b, c)—a critical node in depression-related circuitry[68]—and
632 prolonged immobility in the forced swim test after the CRS modelling (FST; Fig.
633 8n). Furthermore, we verified that CRS exposure did not compromise BBB
634 integrity (Supplementary information, Fig. S23). This confirms that the observed
635 impairments in NVC and subsequent emotional and behavioral dysregulation
636 after CRS were not confounded by non-specific vascular leakage or barrier
637 disruption.[42, 69]

638 Under this sustained adversity, *Glrb*-cKO mice displayed profound
639 resilience. Specifically, they preserved intact whisker-evoked functional
640 hyperemia and remained resistant to the stress-induced constipation-like
641 phenotype, maintaining normal defecation dynamics throughout the 28-day
642 CRS modelling (Fig. 7l, m and Fig. 8l, m). Furthermore, *Glrb*-cKO mice
643 displayed high mobility in the FST, independent of CRS exposure (Fig. 8n). At
644 the cellular and endocrine levels, *Glrb*-cKO mice were protected from the
645 maladaptive sensitization of stress circuits, showing no significant increase in
646 baseline BLA neural activity and serum corticosterone concentrations
647 compared with CRS-treated littermate controls at the end of CRS (Fig. 8o, p).

Importantly, *Glrb*-cKO mice exhibited normal locomotion and spatial preference in the 40 cm OFT (Supplementary information, Fig. S22d, e), ruling out hyperactivity or altered exploratory drive as confounding factors for the observed behavioral improvements. Finally, it is important to note that *Glrb*-cKO mediated protection may brain-region specific. While emotional and neurovascular homeostasis was preserved, *Glrb*-cKO mice still experienced stress-induced weight loss comparable to CRS-treated littermate controls (Fig. 8q). This suggested that while enhanced NVC effectively shields the brain's emotional circuits, it did not negate the systemic physiological costs of chronic stress.

DISCUSSION

In this study, we demonstrate that bidirectional control of NVC enables bidirectional modulations of the negative emotion states. Far from being a passive metabolic read-out of neuronal activity, NVC within the BLA–but not in the primary somatosensory cortex–operates as an indispensable active regulator of the affective negative emotion network. By combining genetic, pharmacological, and optogenetic approaches, our findings reveal that the vascular interface acts as a gatekeeper, tuning stress signals to either be amplified into anxiety-like under mild stress or dampened into resilience to strong stress. These findings redefine the BLA NVC as a proactive component

669 of affective circuitry.

670 More than a century after the first measurements of regional CBF laid the
671 foundation for modern NVC research, the field has come to a new door–what
672 next?[70] We knock on this door by beginning with addressing the role of BLA
673 NVC in emotion modulation, offering a conceptual framework for exploring the
674 regulatory capacity of NVC across functionally distinct brain regions and their
675 respective outputs.

676 During optogenetic manipulations, the ~3% hemodynamic changes we
677 detected (Fig. 5n) is highly consistent with recent work by Hauglund et al.[57]
678 showing that analogous ~3% CBV changes sufficiently drive cerebrospinal fluid
679 flow. This concordance across two separate research groups verifies that subtle,
680 persistent shifts in basal blood volume can be sufficient to elicit notable
681 functional effects, for instance, elevated neural activity in the BLA (Fig. 5h, i, q,
682 r left).

683 Our arteriolar optogenetic data provide genuine *in vivo* validation that the
684 neurovascular unit (NVU) acts as a critical regulator of proximal neural activity
685 (Fig. 5e-m). Even under the minimal-stress home cage context with negligible
686 external stress, arteriole contraction potently activated neighboring neurons
687 (Fig.5q, r left), defining an *in vivo* form of vasculo-neuronal coupling (VNC) that
688 mirrors earlier *ex vivo* observations.[24] These findings imply an implication that
689 NVC and VNC operate as two arms of a fast, closed loop, enabling real-time,

690 bidirectional crosstalk between vascular and neuronal compartments.

691 NVC is a widely recognized, evolutionarily conserved biological process.[71]
692 The “premature exit” observed in NVC-deficient mice under predator-like stress
693 (Fig. 6) suggests that NVC is innately encoded to optimize the kinetics
694 underlying the predatory fear response cycle. As a survival-critical program, this
695 regulatory property may explain the evolutionary conservation of NVC across
696 species.

697 The specific mechanism by which *Glrb* deficiency enhances NVC warrants
698 further investigation. In mural cells, the intracellular chloride concentration (Cl^-
699 $_i$) is typically higher than the extracellular concentration (Cl^-_e), creating an
700 electrochemical gradient where the opening of chloride-permeable glycine
701 receptors leads to Cl^- outflow—a sharp contrast to the Cl^- influx observed in
702 mature neurons.[72-75] This efflux is predicted to depolarize mural cells and
703 promote contraction; thus, the ablation of *Glrb* likely diminishes the baseline
704 contractile ability of mural cells. Given that *Glrb* (GlyRβ) is selectively enriched
705 in venular SMCs (vSMCs) (Fig. 7a–d) and that its deletion in arteriolar SMCs
706 (aSMCs) fails to recapitulate the “super-coupled” phenotype (Supplementary
707 information, Fig. S20a, b), we propose that *Glrb* (GlyRβ) functions as a
708 physiological constraint on venular conductance. Upon its removal, neural
709 inputs—such as those during whisker stimulation—elicit a significantly
710 amplified NVC response (Fig. 7l, m).

711 While *Grin2d* and *Glrb* appear to exert their primary effects on distinct
712 vascular segments—the arteriolar and venular compartments, respectively—
713 their mutual counteraction suggests a complex hemodynamic synergy (Fig. 7l,
714 m). One plausible interpretation is that vSMCs also possess a regulatory weight
715 within the arteriole-capillary-venule network that is functionally comparable to
716 that of aSMCs. These findings suggest that NVC operates as an integrated
717 network property in the vasculature system, where enhanced venular
718 hemodynamics functionally offsets arteriolar deficits to maintain an apparent
719 partial equilibrium (Figures 7 and 8).

720 At the molecular level, we propose that GluN2D activates a signaling
721 cascade in arteriolar SMCs—specifically, a GluN2D–Ca^{2+}-bound calmodulin–
722 caldesmon–α-SMA axis. Caldesmon typically binds to α-SMA filaments and
723 sterically blocks their interaction with myosin, thereby suppressing cross-bridge
724 formation.[55] Ca^{2+}-bound calmodulin, generated following Ca^{2+} entry through
725 GluN2D-containing NMDARs, is known to relieve this inhibition.[55] Consequently,
726 GluN2D activation is predicted to release the caldesmon "brake", modulating α-
727 SMA–myosin cross-bridge cycling to increase CBF. Although this pathway
728 warrants further direct validation, our prediction is supported by genetic
729 epistasis analysis: *Cald1* knockdown effectively phenocopies the *Grin2d*-cKO
730 phenotypes (Fig. 4l-q), and the lack of an additive effect when combining these
731 two perturbations (*Grin2d*-cKO+local BLA *Cald1* KD) suggests that they
732 potentially operate within the same axis (Fig. 4l-q).

733 This study has two primary limitations. First, the current lack of a venular
734 SMCs-specific *CreER* line necessitated the use of the pan-mural *Pdgfrb-CreER*
735 driver to perturb *Glrb* in arteriolar SMCs, pericytes, and venular SMCs. Second,
736 we utilized male cohorts to minimize hormonal variability; future investigations
737 involving female mice are warranted to establish the sex-dependent
738 generalizability of these neurovascular mechanisms.

739 In conclusion, we identified that NVC functions as an active physiological
740 gatekeeper rather than a passive support system. This study establishes NVC
741 as a key target for basic research into neural circuits and mood disorders.

742

743 **MATERIALS AND METHODS**

744 **Animal care and subject selection**

745 All animal procedures complied with the Institutional Animal Care and Use
746 Committee (IACUC) guidelines of the School of Life Sciences, Westlake
747 University (Protocol 24013JJM). Mice were housed in the Westlake University
748 Laboratory Animal Resource Centre under strictly controlled conditions: a 12-h
749 light/dark cycle at 25 °C, with maximum six mice per individually ventilated cage,
750 and *ad libitum* access to standard chow and water. To exclude potential
751 confounding effects from the estrous cycle on emotional behavior, we
752 exclusively used age-matched male C57BL/6J mice (60–80 days old at the
753 onset of experiments).[30]

754

755 **Rigor and bias control for behavior-related assay**

756 We implemented rigorous protocols to minimize behavioral variability arising
757 from habituation or handling. To ensure stable baseline conditions, animals
758 were first acclimated to the facility for at least two weeks and then habituated
759 to the testing room environment for at least 90 min prior to each specific assay.
760 All handling and behavioral assays were performed by a single trained
761 experimenter who was strictly blinded to genotype and group assignments;
762 blinding was maintained by a separate researcher who managed genotyping
763 results. Furthermore, testing was confined to a fixed daily time window (13:00–
764 19:00). To prevent exposure to uncontrolled olfactory or auditory cues, testing
765 areas were strictly controlled for light, noise, and odor: apparatuses were
766 thoroughly cleaned with 70% ethanol and ventilated between trials, and animals
767 were transported in standardized containers. Finally, animals were randomly
768 distributed across experimental groups from different cages to control for
769 potential cage effects.[30, 76, 77]

770

771 **Home cage non-invasive physiological monitoring**

772 To assess physiological parameters with minimal disturbance, mice were
773 monitored in their home cages. Blood pressure was measured using a non-
774 invasive tail-cuff system (Kent/Biopa), and the occupation of fat was measured

using EchoMRI™-100H (EchoMRI) during the fixed experimental time window (13:00–19:00); crucially, mice were habituated to the restrainer for three consecutive days prior to recording to minimize stress artifacts.

For baseline metabolic and excretory profiling, mice were housed in groups of four. Over three consecutive 3-day cycles, animals were provided with standardized quantities of food (60 g), water (340 g), and bedding (100 g). At the end of each cycle, body weight, ingestive behaviors (food and water intake), fecal output, and urination volume (derived from bedding weight gain) were recorded. For home-cage baseline assessments where individual excreta could not be definitively assigned in group-housed conditions, data were averaged per mouse within each cage. To ensure statistical rigor and avoid pseudoreplication, the cage mean was utilized as the independent experimental unit (N = 4 cages). To facilitate cross-group comparisons, weight data were normalized to the littermate control baseline. Specifically, the value of each sample was divided by the mean value of the control group (defined as 100%). To record defecation bouts, mice were individually housed in new home cages for 3 days of habituation. Existing fecal pellets were cleared 15 min prior to the assay, and the number of defecation bouts was recorded during the subsequent 15-min interval. Following monitoring, mice were randomly assigned to terminal procedures, including gastrointestinal inspection, retro-orbital blood collection for ELISA, blood-brain barrier (BBB) integrity assessment, and brain extraction for c-Fos immunofluorescence mapping. All

assessors remained blinded to group identity throughout data collection and analysis.

Behavioral assays

We performed all behavioral assays using a rigorous double-blind protocol. One trained experimenter conducted the assays, while a second, independent experimenter performed the video scoring and data analysis. To eliminate olfactory cues and ensure consistency, we cleaned all apparatus with 70% ethanol and fully aerated them between subjects.

Open field tests (OFTs)

To assess emotional responses under graded stress intensities, the OFT was conducted in square arenas of three specific dimensions: standard (40 × 40 cm), intermediate (35 × 35 cm), and constricted (10 × 10 cm). Mice were placed in the center of the arena, and behavior was recorded for 15 min using an overhead camera. Unsupported rearing—defined as standing on hindlegs without contacting the arena walls—was quantified during the first 5 min. Defecation metrics (bouts, rate, and latency), running distance, and area preference were measured across the entire 15-min session. For zonal analysis, the arena floor was digitally divided into 25 equal squares (5 × 5 grid); the center zone was defined as the inner 9 squares, excluding the 16 peripheral squares

818 adjacent to the walls.

819 After testing, mice were transferred to clean, individual cages. Retro-orbital
820 blood samples for ELISA analysis were collected 5 min post-assay. Mice
821 designated for immunofluorescence were perfused 90 min after the assay to
822 capture peak c-Fos expression. For linear correlation analyses, behavioral and
823 physiological data were paired from the same individual subjects.

824 To adhere to the 3Rs principles (Replacement, Reduction, and Refinement)
825 and minimize animal usage, 40 cm OFT data (including whisker stimulation
826 data) for *SMA-creER:Grin1*$^{f/f}$ mice were obtained through the retrospective re-
827 analysis of unpublished datasets independently generated in our laboratory.
828 This approach enhances the reproducibility of our findings, as these data were
829 collected by a different experimenter at a distinct time point using identical
830 experimental parameters. Due to the nature of the original experimental
831 recordings, which were restricted to behavioral videos and whisker-evoked
832 hemodynamic measurements, c-Fos and serum corticosterone data were not
833 available for the *SMA-creER:Grin1*$^{f/f}$ line.

834 For fiber photometry and optogenetic-based OFT, only 40 cm OFT used.
835 Tamoxifen induction 21 days prior to formal testing. For real-time NVC
836 monitoring, *AAV2/9-hSyn-GCaMP8f* was stereotaxically injected into the BLA
837 (AP: −1.6 mm; ML: ±3.45 mm; DV: −4.00 mm), and optic fibers were implanted
838 immediately above the injection site (DV: −3.95 mm). Following a two-week

839 recovery and three days of fiber-connection habituation, mice received a retro-
840 orbital injection of Rhodamine B (Sigma, R9379; 100 μl, 5 mg/ml for formal
841 assay) 15 min prior to the 40 cm OFT. The experimental timeline comprised
842 three sequential recording phases: pre-test (home cage), test (40 cm OFT), and
843 post-test (home cage).

844 To rigorously isolate genuine functional signals from hemodynamic and
845 motion-related artifacts, we employed a multi-wavelength fiber photometry
846 system (Thinkertech) for all fiber photometry assays referred published
847 methods.[78, 79] Fluorescence signals were acquired via 473 nm excitation for
848 GCaMP8f (Ca^{2+}-dependent) and 580 nm for Rhodamine (blood volume). A 405
849 nm channel was utilized as an isosbestic reference; at this wavelength,
850 GCaMP8f fluorescence remains Ca^{2+}-insensitive, serving as a precise proxy for
851 non-specific absorption and motion artifacts that affect both the green and red
852 emission spectra. To decontaminate the functional data, the 405 nm reference
853 trace was independently fitted to the 473 nm and 580 nm raw signals using
854 least-squares linear regression. These fitted components were then subtracted
855 from their respective raw traces. This dual-correction strategy effectively
856 neutralized common-mode noise and ensured that the reported $\triangle F/F$ for both
857 GCaMP8f and Rhodamine reflects true physiological dynamics—neuronal
858 activity and functional blood volume changes, respectively—undistorted by
859 physical movement or non-functional optical fluctuations. These data
860 processing and normalization protocols were applied consistently to

861 optogenetic experiments to ensure cross-experimental comparability (details
862 and formula shown below).

863 For optogenetic manipulation of vascular contractility,[43, 44, 57] optic fibers
864 were implanted in *SMA-creER:Ai32* (ChR2-EYFP) and control *SMA-*
865 *creER:Ai47* (EYFP) mice using the coordinates described above (without
866 *AAV2/9-hSyn-GCaMP8f* injection). Mice received tamoxifen induction 21 days
867 prior to testing. Following habituation and Rhodamine injection, blue light pulses
868 (473 nm) were delivered to induce optogenetic stimulation while simultaneously
869 monitoring cerebral blood volume (CBV) via Rhodamine fluorescence (580 nm).
870 To capture the full hemodynamic response profile, recordings were segmented
871 into three phases: pre-stimulation baseline, optical stimulation, and post-
872 stimulation recovery. Optogenetic stimulation cycle consisted of an 85 ms
873 stimulation pulse followed by a 5 ms interval and a 5 ms recording window (10
874 Hz, 0.939 mW laser power).

875 As for isosbestic correction for hemodynamic artifacts, similar to BLA
876 photometry recording, signal fluctuations at the 405 nm isosbestic point are
877 calcium-independent and primarily reflect changes in light scattering and
878 absorption by dynamic hemoglobin concentration changes (functional
879 hyperemia). We applied a linear regression correction algorithm. As mentioned
880 above, the 405 nm signal was fitted to the 473 nm signal, and the predicted
881 hemodynamic/motion component was subtracted. This correction confirms that
882 the CBV recording during the optogenetic stimulation represents a genuine

883 hemodynamics.

884 Two distinct normalization strategies were applied to quantify CBV
885 dynamics:

886 1. Static Baseline Comparison (Cross-group): To allow for cross-
887 group comparisons of basal vascular hemodynamics, data were normalized
888 to the mean raw value of the control group. Specifically, the raw value of
889 each individual sample was divided by the mean raw value of the littermate
890 control group (defined as 100%). This approach standardizes the readout,
891 ensuring that reported values reflect specific genotypic differences in
892 perfusion capacity relative to a physiological baseline.

893 2. Dynamic Response Quantification (Time-series): For time-series
894 recordings of CBV (as well as Ca^{2+} signal recording and Laser Speckle
895 Contrast Imaging recording), a temporal normalization strategy was applied.
896 The baseline signal ($F_{baseline}$) was defined as the mean value recorded
897 during the defined pre-stimulation period (e.g., the 30-second baseline
898 window). The relative change at each time point (F_t) was calculated as a
899 percentage of its own baseline using the formula:

900 $$\triangle CBV\ (\%)\ \text{or}\ \triangle Ca^{2+}\ (\%) = (F_t - F_{baseline}) / F_{baseline} \times 100\%$$

901 This self-normalization approach isolates the evoked hemodynamic
902 response from background variations. This peak-aligned averaging strategy

903 ensures that the quantification of the metabolic plateau is temporally
904 synchronized to the individual hemodynamic kinetics of each animal.

905 Fourier transform plots were generated in MATLAB, with frequency and
906 power spectral density represented on the *X* and *Y* axes, respectively. The
907 analysis was conducted using the acquisition parameters specified in the 40
908 cm OFT optogenetic stimulation section. To resolve the spectral characteristics
909 of the BLA hemodynamic response, Fast Fourier Transform (FFT)[80-82] was
910 applied to the CBV time series. For visualization, the low-frequency range (0–
911 1 Hz) is presented in the representative spectral panel. For statistical
912 quantification, the Area Under the Curve (AUC) was calculated specifically for
913 the ultra-low frequency band (0–0.3 Hz) to represent oscillatory power across
914 experimental groups.[83, 84] The relevant codes can be found at the GitHub
915 website:
916 https://github.com/JialabEleven/Functional_hyperemia_regulates_emotion-
917 master/tree/master/Part7_Frequency_analysis.
918

919 Home cage optogenetic stimulation and recording

920 To determine if BLA vasoconstriction is sufficient to induce negative emotion in
921 a non-aversive environment, simultaneous optogenetics and photometry were
922 performed in the home cage. *SMA-creER:Ai32* (ChR2-EYFP) and control *SMA-*
923 *creER:Ai47* (EYFP) mice received tamoxifen induction 21 days prior to testing.
924 Optic fibers were implanted above the BLA (AP: −1.6 mm; ML: ±3.45 mm; DV:

925 −3.95 mm) two weeks before the assay, and mice were habituated to the
926 recording tether for three days. The experimental procedures for optogenetic
927 stimulation in the home cage were identical to those conducted in the 40 cm
928 OFT, with the exception of the testing environment.

929 On the test day, Rhodamine B (100 μL, 5 mg/mL) was administered via
930 retro-orbital injection 15 min prior to recording. The session comprised three
931 15-min epochs: baseline, stimulation, and recovery. To ensure signal fidelity
932 and prevent spectral crosstalk, an optimized interleaved illumination sequence
933 was employed: (1) 405 nm for isosbestic control; (2) 580 nm for continuous
934 CBV recording; and (3) 473 nm for optogenetic stimulation (delivered
935 exclusively during the second epoch). The duty cycle consisted of an 85 ms
936 stimulation pulse followed by a 5 ms interval and a 5 ms recording window (10
937 Hz, 0.939 mW laser power). To standardize baseline conditions, all existing
938 fecal pellets were removed immediately before recording, and fresh fecal output
939 was quantified at the end of the session. Data analysis and processing for
940 optogenetics in the home cage is similar to that in the 40 cm OFT.

941

942 Tube stress assay

943 Restraint stress was induced using modified 50 mL conical tubes (Corning,
944 Cat# 430290).[85, 86] To prevent hypoxia and hyperthermia, tubes were equipped
945 with multiple ventilation apertures drilled into the cap and body, ensuring

946 adequate airflow while strictly restricting physical movement.

947 For the acute restraint stress (ARS) paradigm, mice were restrained for a
948 single 15-min session, and fecal pellet output was quantified immediately upon
949 release. To interrogate the causal role of BLA activity in stress responses, we
950 utilized a chemogenetic BLA neural silencing strategy. *AAV2/5-mCaMKIIa-*
951 *hM4D(Gi)-EGFP-ER2-WPRE-pA* (inhibitory DREADD) or the control virus
952 *AAV2/5-mCaMKIIa-EGFP-ER2-WPRE-pA* was bilaterally injected into the BLA
953 (AP: −1.6 mm; ML: ±3.45 mm; DV: −4.0 mm). Following a two-week recovery
954 period, mice were subjected to behavioral testing (including the 40 cm OFT
955 described above). To ensure peak DREADD activation during the stressor, the
956 agonist Compound 21 (C21; MCE, Cat# HY-100234; 0.1 mg/kg, i.p.) was
957 administered 45 min prior to initiating restraint. Following ARS, mice were
958 individually housed in clean cages. Retro-orbital blood samples for ELISA
959 analysis were collected 5 min post-assay. To capture stress-induced neuronal
960 activation, mice were perfused 90 min post-assay for c-Fos
961 immunofluorescence mapping.

962 For the chronic restraint stress (CRS) paradigm, mice were subjected to daily
963 restraint sessions for 28 consecutive days. To prevent habituation to the
964 stressor, both the duration (randomized between 120 and 180 min) and the
965 daily onset time (within the light phase) were varied. The physiological impact
966 of chronic stress was assessed weekly (at the end of each 7-day block) by
967 recording fecal output and stool consistency (Bristol Score)[87] during a 60-min

968 monitoring period in a clean home cage. Bristol scores analysis was conducted
969 by an independent researcher blinded to the mouse genotypes and treatment
970 groups. Mice designated for Elevated Plus-Maze (EPM) Test, Forced Swim Test
971 (FST), Blood-brain-barrier (BBB) integrity assessment, ELISA inspection, and
972 immunofluorescence analysis were sacrificed 24 hours after the final CRS
973 session.

974

975 Complex-open field test

976 To simulate an environment of high visual contrast and frustrated escape, the
977 complex OFT (c-OFT) was conducted in a specialized chamber divided into two
978 compartments: a high-illumination white zone (aversive) and a low-illumination
979 black zone.[29, 88] Crucially, these zones were separated by a barred metal
980 partition that permitted visual contact with the safe environment but precluded
981 physical entry. Mice were placed in the center of the white compartment at trial
982 onset, and behavioral responses to this context of unattainable safety were
983 continuously recorded for 20 min. Defecation bouts inspection after the assay.
984 To capture stress-induced neuronal activation, mice were perfused 90 min post-
985 assay for c-Fos immunofluorescence mapping.

986

987 Looming assay

988 Innate defensive behaviors against aerial predators were assessed by adapting

989 established protocols,[62] with specific optimizations implemented to standardize
990 threat perception. Mice were first acclimated to the arena for 10 min to stabilize
991 baseline anxiety levels. To ensure that defensive responses (freezing or flight)
992 were distinct from baseline immobility or thigmotaxis, a state-dependent
993 triggering protocol was employed. Unlike continuous stimulation paradigms, the
994 looming stimulus—a rapidly expanding overhead black disk—was manually
995 triggered only when the mouse met specific behavioral criteria: spontaneous
996 locomotion (speed 13–15 cm/s) and positioning within the arena center (away
997 from the walls). Behavioral responses were recorded using a high-resolution
998 overhead camera. Each mouse underwent a single stimulation trial to prevent
999 habituation. Immediately following the assay, mice were housed individually in
1000 clean cages for 90 min prior to perfusion for c-Fos analysis.

1001

1002 Virtual reality eagle (VR_{eagle}) assay

1003 To simulate an aerial predator attack within a highly controlled, multimodal
1004 environment, we employed a custom-built virtual reality (VR) flight simulation
1005 system. Assay design modified from previous work.[62, 63] The apparatus
1006 consisted of an air-supported spherical treadmill (float ball) allowing
1007 unrestricted locomotion, surrounded by a panoramic display system to create
1008 an immersive visual field. Two weeks prior to testing, mice were implanted with
1009 titanium headplates. To strictly decouple restraint stress from predator-induced

1010 responses, animals underwent a rigorous daily habituation protocol (one week)
1011 to the head-fixation apparatus and the floating ball mechanism until they
1012 demonstrated stable voluntary locomotion. On the testing day, mice were head-
1013 fixed and allowed a 5-min adaptation period within a neutral visual landscape.
1014 To ensure the capture of active defensive responses, a state-dependent
1015 triggering protocol was enforced: the predator stimulus was triggered only after
1016 the mouse initiated spontaneous locomotion following the adaptation phase.
1017 The stimulus consisted of a high-fidelity eagle avatar diving rapidly from the
1018 dorsal to the proximal visual field (3 s duration), temporally synchronized with
1019 an eagle call (audiovisual integration, ~75 dB at first 1.5 s). Pupil diameter was
1020 tracked via an infrared camera, and locomotion speed was recorded via rotary
1021 encoders sampling the spherical treadmill rotation. Data acquisition continued
1022 for 2 min post-stimulation to assess recovery kinetics. Each mouse underwent
1023 a single stimulation trial to prevent habituation. Immediately following the assay,
1024 mice were housed individually in clean cages for 90 min prior to perfusion for
1025 c-Fos analysis.

1026

1027 Elevated Plus-Maze (EPM) Test

1028 To assess anxiety-like behavior, the EPM was conducted using an apparatus
1029 elevated 50 cm above the floor, consisting of two open arms (65 × 5 cm) and
1030 two closed arms (65 × 5 cm) intersecting at a central platform.[89, 90] At the trial

1031 onset, mice were placed in the center zone facing an open arm and allowed to
1032 explore freely for 5 min. The duration of time spent in the open arms was
1033 recorded.

1034

1035 Forced Swim Test (FST)

1036 To evaluate behavioral despair, the FST was performed in a transparent glass
1037 cylinder filled with water (25 °C) to a depth sufficient to preclude caudal
1038 support.[91] Behavior was recorded for a 5-min session. The duration of
1039 immobility—defined as floating with the absence of active struggling, exhibiting
1040 only minimal movements necessary to maintain the head above water—was
1041 quantified. Immediately post-assay, mice were dried and returned to warmed
1042 home cages.

1043

1044 **Enzyme-linked immunosorbent assay (ELISA)**

1045 To assess physiological stress levels, blood samples were allowed to clot at
1046 controlled room temperature (22–25 °C) for 2 hours. Serum was isolated by
1047 centrifugation at 3,000 rpm for 20 min at 4 °C, followed by a secondary
1048 clarification spin at 8,000 rpm for 3 min to remove residual debris.
1049 Corticosterone concentrations were quantified using a commercial ELISA kit
1050 (Absin, Cat# abs554164-96T) strictly following the manufacturer's protocol.
1051 Optical density (OD) was measured using a Cytation 5 microplate reader

1052 (Agilent, Model MS-SP104).

1053

1054 **Stereotaxic viral transduction**

1055 Mice were anesthetized with isoflurane and secured in a stereotaxic frame. To
1056 minimize bias, surgical procedures were performed by investigators who were
1057 blinded to the group allocations. For manipulations targeting the BLA, viral
1058 vectors were microinjected at the following coordinates relative to Bregma: AP:
1059 −1.6 mm; ML: ±3.45 mm; DV: −4.0 mm. For chemogenetic inhibition, mice
1060 received bilateral injections (150 nL per side) of the neural inhibitory DREADD
1061 virus *AAV2/5-mCaMKIIa-hM4D(Gi)-EGFP-ER2-WPRE-pA* (2.3 × 10^{12} VG/mL)
1062 or the control virus *AAV2/5-mCaMKIIa-EGFP-ER2-WPRE-pA* (2.3 × 10^{12}
1063 VG/mL).[37] For neuronal calcium recording: The calcium indicator *AAV2/9-hSyn-*
1064 *jGCaMP8f-WPRE-pA* (2.0 × 10^{12} VG/mL) was injected bilaterally (150 nL per
1065 side) using the same coordinates. To label glycinergic neurons in the medullary
1066 reticular formation, *rAAV2/4-Glyt2-EGFP-WPRE-hGHpolyA* (5 × 10^{12} VG/mL)
1067 was injected bilaterally (500 nL per side) at coordinates: AP: −3.5 mm; ML:
1068 ±0.84 mm; DV: −2.8 mm.[92]

1069 Following surgery, mice were allowed to recover for at least two weeks to
1070 ensure optimal viral expression and physiological recovery prior to behavioral
1071 testing or brain collection.

1072

1073 **Immunofluorescence staining and microscopy**

1074 To preserve tissue integrity and antigenicity, mice were deeply anesthetized
1075 with 1% pentobarbital sodium (80 mg/kg, i.p.) and transcardially perfused with
1076 ice-cold PBS (5 min) followed by 4% paraformaldehyde (PFA) in PBS (5 min).
1077 Brains and peripheral organs were harvested, post-fixed in 4% PFA for 6 hours
1078 at 4 °C, and sectioned at 50 μm using a vibratome (Leica Histo-VT1200S).
1079 Cultured cells were washed with PBS and subsequently fixed in 4% PFA for 10
1080 min at room temperature.

1081 For immunolabeling, free-floating sections were permeabilized and
1082 blocked in PBS containing 1% Triton X-100 and 0.25% normal donkey serum
1083 (NDS) for 60 min at room temperature. Following three washes in PBS, sections
1084 were incubated overnight at 4 °C with primary antibodies in a buffer containing
1085 0.1% Triton X-100. After extensive washing, sections were incubated with
1086 species-specific fluorescence-conjugated secondary antibodies (in 0.1% Triton
1087 X-100) for 2 hours at room temperature. Nuclei were counterstained with DAPI
1088 (1:1000; Beyotime, Cat# C1002). Sections were mounted using anti-fade
1089 medium (SouthernBiotech, Cat# 0100-01) and imaged using a Zeiss LSM800
1090 confocal microscope.

1091 To explicitly quantify the spatial distribution of proteins relative to the
1092 vasculature (e.g., GlyRβ distribution), orthogonal linescan profiling was
1093 performed. Regions of interests (ROIs) were selected where vessels appeared

in longitudinal cross-section (brain slice) or appropriate places in the boundary of cultured Human Umbilical Vein Smooth Muscle Cells. Line profiles (width: 5 pixels) were drawn to capture the fluorescence intensity gradient. Besides, to validate the robustness of these spatial associations and control for selection bias, Pearson's Correlation Coefficient (PCC) was calculated across the entire ROI using the ImageJ Coloc 2 plugin.[93] This global metric confirmed the degree of pixel-by-pixel co-localization between the target protein and the vascular marker, independent of specific linescan trajectories.

As for cellular quantification and normalization, distinct quantification and normalization strategies were applied based on the specific biological metrics:

1. Cellular Intensity (e.g., c-Fos): The total number of NeuN-positive nuclei was identified within the defined ROI. Preliminary analysis confirmed that the density of NeuN-positive neurons was consistent across groups, validating the use of area-based normalization. Activation intensity was calculated by dividing the positive neural count by the total area of the ROI, expressed as c-Fos positive neurons per mm^2. Additionally, to facilitate comparison with alternative quantification methodologies, the proportion of c-Fos-positive neurons relative to the total neuronal population within the BLA and LHb was also calculated. These supplementary data are provided in the supplementary information (Supplementary information, Fig. S24).
2. Relative Protein Expression (e.g., GluN2D, HIF-1α, and IgG): Mean Fluorescence Intensity (MFI) was measured specifically within the somatic

1116 ROIs of NeuN-positive neurons. To facilitate cross-group comparisons, data
1117 were normalized to the littermate control baseline. Specifically, the MFI of
1118 each sample was divided by the mean MFI of the littermate control group
1119 (defined as 100%).

1120 3. Signal colocalization (e.g., COX-2): Background fluorescence in
1121 the COX-2 channel (546 nm) was first subtracted across the field of view.
1122 The colocalization between the COX-2 signal and the NeuN signal (488 nm)
1123 within NeuN-positive regions was then quantified using the Pearson
1124 correlation coefficient (PCC, Coloc 2 plugin in ImageJ software).

1125

1126 **Pharmacological interventions**

1127 To induce Cre-mediated recombination, Tamoxifen (MCE, Cat# HY-13757A)
1128 was dissolved in corn oil (Aladdin, Cat# C116023) at a concentration of 10
1129 mg/mL. The solution was administered via oral gavage (200 μL daily). Dosing
1130 schedules were tailored to specific genotypes: *Acta2*-cKO mice were treated
1131 from postnatal day 21 (P21) to P24, whereas all other transgenic lines received
1132 treatment from P60 to P63, unless otherwise specified.

1133 For acute pharmacological manipulations, two distinct delivery routes were
1134 employed:

1135 1. Systemic Administration: Drugs were delivered via intraperitoneal
1136 (i.p.) injection at a standardized volume of 200 μL per mouse. Behavioral

1137 assays commenced 15 min post-infusion to target the peak efficacy window.

1138 2. Local BLA injection: To target the BLA specifically, a stainless-steel
1139 guide cannula (RWD, Cat# 800-00245-00) was stereotaxically implanted at
1140 coordinates AP: −1.6 mm, ML: ±3.45 mm, DV: −4.0 mm. Drugs were
1141 microinfused (1 μL total volume) at a controlled rate of 250 nL/min using an
1142 automated syringe pump. HET0016 (10 μM) was microinfused locally into
1143 the BLA. Behavioral assays commenced 5 min post-infusion to target the
1144 peak efficacy window.

1145

1146 **Cell isolation and culture**

1147 To characterize SMC-specific molecular mechanisms, primary cultures were
1148 established by the SMCs sorted from P0 brain parenchymal tissue of *SMA-*
1149 *creER:Ai47* mice. Cortical parenchymal tissue was dissected following
1150 hypothermia-induced anesthesia and digested in 0.25% trypsin (Thermo
1151 Scientific, Cat# 25200072) for 15 min at 37 °C. Digestion was terminated with
1152 fetal bovine serum (FBS; Gibco, Cat# 10099). The suspension was passed
1153 through a 40 μm cell strainer (Falcon, Cat# 352340) and centrifuged at 1,600 ×
1154 g for 5 min at 4 °C. Pelleted cells were resuspended in Smooth Muscle Cell
1155 Medium (SMCM; ScienCell, Cat# 1101) and plated in T25 flasks (Corning, Cat#
1156 430639).

1157 To purify SMC lineages, primary cultures (~80%) were treated with

1158 Tamoxifen (5 μM in DMSO; Solarbio, Cat# D8371) to induce EGFP expression
1159 specifically in α-SMA-positive cells. Four days post-induction, EGFP-positive
1160 cells were purified using an MA-900 cell sorter (Sony, FCCF-MBR). Sorted cells
1161 were maintained in SMCM for downstream assays. The purity of SMCs isolated
1162 via this protocol has been previously validated.[94]

1163 To capture the *in vivo* transcriptional profile of mural cells (e.g., validation
1164 of *Glrb* expression), freshly isolated cells were used rather than cultured
1165 populations. Pdgfrβ-positve cells were sorted directly from dissociated whole-
1166 brain single-cell suspensions for P60 mice using an anti-Pdgfrβ antibody and
1167 immediately lysed in TRIzol reagent to minimize transcriptional alterations. For
1168 the assay in Fig. 7g, Human Umbilical Vein Smooth Muscle Cells (HU-vSMC;
1169 ScienCell, Cat# 8020) were cultured under standard conditions recommended
1170 by the manufacturer.

1171

1172 **Semi-quantitative reverse transcription PCR (RT-PCR)**

1173 Total RNA was extracted from two distinct sources using TRIzol reagent
1174 (Sangon Biotec, Cat# B511311-0100): (1) Cultured Cells: Sorted EGFP-positive
1175 SMCs harvested at ~90% confluence; and (2) Brain Tissue: Cortices or
1176 cerebella dissected from P60/P0 mice under 1% pentobarbital sodium (80
1177 mg/kg, i.p.)-induced (P60) or hypothermia-induced (P0) anesthesia.

1178 First-strand cDNA was synthesized (50 ng/μL) using the HiScript III 1st

1179 Strand cDNA Synthesis Kit (Vazyme, Cat# R312-02). For transcript abundance
1180 analysis, semi-quantitative PCR amplification was performed using Green Taq
1181 Mix (Vazyme, Cat# P131-AA). The reaction mixture contained 10 μL Taq Mix, 2
1182 μL cDNA, 2 μL primer pairs (10 μM), and 6 μL RNase-free water. PCR
1183 amplicons were resolved on 2% agarose gels (BIOWEST, Cat# 111860) via
1184 electrophoresis (220 V for 30 min) and imaged using a Tanon 1600 system.

1185 To quantify relative mRNA abundance, the mean grey value of
1186 electrophoretogram bands was quantified using ImageJ software: Band
1187 intensities were first normalized to the corresponding internal loading control
1188 (e.g., *18s*) to correct for variations in lane-to-lane loading. Then, to determine
1189 relative expression levels across groups, these normalized values were
1190 subsequently divided by the mean value of the littermate control group (defined
1191 as 100%).

1192

1193 **RNAscope *in situ* hybridization**

1194 To validate cell-type-specific gene expression, 15 μm horizontal brain sections
1195 were prepared using a Leica CM1950 cryostat. Genetically modified lines were
1196 utilized to map specific targets: *SMA-creER:Ai14* mice for *Grin2d* expression in
1197 arteriolar SMCs, and *Pdgfrβ-creER:Ai14* mice for *Glrb* in mural cells; *WT* mice
1198 were used for probe specificity validation (*Grin1* and *Grin2d*). Multiplex
1199 fluorescent *in situ* hybridization was performed using the RNAscope Multiplex

1200 Fluorescent Reagent Kit v2 (ACDbio, Cat# 323100) strictly adhering to the
1201 published works and manufacturer's guidelines.[38, 89] Specific probes included
1202 *Grin2d* (Cat# 425951-C3), *Grin1* (Cat# 431611), and *Glrb* (Cat# 1225261-C1).
1203 Spatial quantification, including orthogonal linescan profiling and co-localization
1204 assessment, was performed identically to the immunofluorescence protocol
1205 described above. Briefly, regions of interests (ROIs) were selected where
1206 vessels appeared in longitudinal cross-section. Line profiles (width: 5 pixels)
1207 were drawn to capture the fluorescence intensity gradient. Besides, to validate
1208 the robustness of these spatial associations and control for selection bias,
1209 Pearson's Correlation Coefficient (PCC) was calculated across the entire ROI
1210 using the ImageJ Coloc 2 plugin.

1211

1212 **Western blot**

1213 Protein extraction was performed on two distinct sample types: (1) Brain Tissue:
1214 Dissected regions were homogenized in ice-cold RIPA buffer (Thermo Scientific,
1215 Cat# 89901) supplemented with a protease inhibitor cocktail (CWBIO, Cat#
1216 CW22008); and (2) Cultured Cells: Cells were lysed in the same buffer at ~90%
1217 confluence. Lysates were centrifuged at 12,000 × g for 5 min at 4 °C to remove
1218 insoluble debris. Protein concentrations were determined using a Micro BCA
1219 Protein Assay Kit (CWBIO, Cat# CW2011S). Samples were denatured by
1220 heating at 100 °C for 10 min in SDS-PAGE loading buffer. Proteins were

1221 resolved on 8% SDS-polyacrylamide gels and transferred onto 0.45 μm PVDF
1222 membranes (Millipore, Cat# IPVH00010). Following blocking with 5% non-fat
1223 milk in TBST, membranes were incubated overnight at 4 °C with primary
1224 antibodies, washed, and subsequently incubated with HRP-conjugated
1225 secondary antibodies for 45 min at room temperature. Immunoreactive bands
1226 were visualized using ECL reagents (Abbkine, Cat# BMU102-CN) and captured
1227 on a GE AI680RGB imaging system.

1228 To quantify relative protein abundance, the mean grey value of
1229 immunoreactive bands was quantified using ImageJ software. A rigorous dual-
1230 normalization strategy was applied identically to the RT-PCR protocol: Band
1231 intensities were first normalized to the corresponding internal loading control
1232 (e.g., GAPDH) to correct for variations in lane-to-lane loading. Then, to
1233 determine relative expression levels across groups, these normalized values
1234 were subsequently divided by the mean value of the littermate control group
1235 (defined as 100%).

1236

1237 **siRNA administration**

1238 To achieve broad cerebrovascular knockdown; siRNA was delivered via
1239 injection into the cisterna magna following established protocols.[38] A mixture
1240 containing 0.8 nmol siRNA and FITC-dextran (10 mg/mL; Sigma) was prepared
1241 to allow for visual tracking of the distribution (20 μL total volume, infused 1

1242 ul/min). 10 min post-injection, successful delivery was rigorously verified by
1243 visualizing perivascular FITC fluorescence through the open scalp using a
1244 Zeiss Axio Zoom V16 microscope. Crucially, only mice exhibiting confirmed
1245 widespread perivascular perfusion were included in downstream analyses.
1246 Functional outcomes (Whisker Stimulation and 40 cm OFT) were assessed 48
1247 hours post-injection to align with the window of peak knockdown efficiency.

1248 For local BLA and S1BF knockdown, siRNA solution (1 nM, 150 nL) was
1249 microinjected bilaterally directly into the BLA at coordinates: AP: −1.55 mm; ML:
1250 ±3.40 mm; DV: −4.0 mm (BLA)/ DV: −0.5 mm (S1BF). The 40 cm OFT and ARS
1251 was conducted 48 hours post-injection.

1252

1253 **Whisker stimulation and Laser Speckle Contrast Imaging (LSCI)**

1254 To assess functional hyperemia, mice were anaesthetized with 1% sodium
1255 pentobarbital (80 mg/kg, i.p.). Assay design referred published paper.[38, 48, 60]
1256 Following anesthesia, the head was secured in a stereotaxic frame, and the
1257 scalp was retracted to expose the skull. We stimulated whiskers longitudinally
1258 using a motor-driven brush (12 Hz, 1 min) and recorded CBF dynamics in the
1259 contralateral barrel cortex using a laser speckle contrast imaging system
1260 (RFLSI ZW/RFSLI III, RWD Life Science).[95] Images were acquired at a
1261 resolution of 512 x 512 pixels with an exposure time 5 ms, optimized for 10
1262 frames per second (fps) sampling.

The LSCI system provides data in “Perfusion Units (PU)”, which represent a relative blood flow index derived from the spatial blurring of laser speckle patterns. This index is related to the product of average speed and concentration of moving red blood cells in the tissue sample volume. While these raw PU values were used to compare basal perfusion levels between groups, functional hyperemia data were normalized to correct for inter-individual variations in cranial optical properties. Specifically, the CBF response was calculated as the percentage change relative to baseline:

$$\triangle CBF\ (\%) = (CBF_t - CBF_{baseline}) / CBF_{baseline} \times 100\%$$

Where CBF_t is defined as the perfusion value of each frame; $CBF_{baseline}$ is defined as the mean perfusion value during the 30-second pre-stimulation period.

To characterize the temporal dynamics of functional hyperemia, the peak response time was identified using a custom MATLAB algorithm (Signal Processing Toolbox). Specifically, local maxima in the △CBF time-series were detected using the findpeaks function, with empirical constraints applied to reject signal noise (minimum peak height threshold > 2.2%; minimum peak separation **>** 50 frames). The global maximum detected within the stimulation window was defined as the peak functional hyperemia. To quantify the magnitude of the sustained vascular response, we calculated the mean △CBF over a period from the identified peak latency to 90 seconds (which marks the conclusion of the whisker stimulation).

1285

1286 **Tissue clearing and 3D vascular reconstruction**

1287 To visualize the 3D vascular architecture, mouse brains were washed in PBS
1288 (3 × 2 hours) on a shaker (40 rpm) at room temperature. Tissue clearing was
1289 performed using a commercial kit (Nuohai, NH-CR-210701), adhering strictly to
1290 the manufacturer's protocol. Cleared whole-brain samples were imaged using
1291 light-sheet fluorescence microscopy (LSFM; Nuohai, LS18) with a 561 nm
1292 excitation laser. For structural analysis, raw datasets were stitched using LS18,
1293 software and downsampled (0.25 ×) in ImageJ.

1294 The datasets, comprising 1,500 sagittal slices were registered to the Allen
1295 Mouse Brain Common Coordinate Framework (CCFv3) using the BIRDS plugin.
1296 Specifically, nine reference slices were selected, and their corresponding atlas
1297 indices were manually defined to guide the registration algorithm. The
1298 automated registration for the entire dataset was then executed based on these
1299 reference points. To ensure spatial accuracy, each slice was monitored during
1300 the process, followed by randomized spot-checks post-registration. Any
1301 misalignments were resolved through manual adjustment or by re-running the
1302 registration pipeline. Based on this refined registration, Imaris Surface modules
1303 were generated for specific brain regions (eg., BLA). Vascular structures were
1304 segmented based on fluorescence signal intensity, and vascular volume was
1305 quantified using Imaris software.

1306

1307 **High-Fat Diet (HFD) challenge**

1308 To evaluate NVC integrity under clinically relevant metabolic stress, a diet-
1309 induced obesity model was employed. Mice were randomized into HFD (SYSE,
1310 Cat# PD6001; 60% kcal from fat) or normal fat diet (NFD) control groups for
1311 four weeks. Body weight and food intake were monitored weekly. Physiological
1312 impact was assessed by quantifying home-cage fecal output as described
1313 above. Following the 4-week modelling, mice were subjected to the 40 cm OFT,
1314 and whisker stimulation assays to assess emotional and hemodynamic function,
1315 respectively. For ELISA analysis, serum was collected 5 min after the 40 cm
1316 OFT. For c-Fos immunofluorescence (IF) staining, brain tissues were harvested
1317 90 min post- 40 cm OFT.

1318

1319 **Immunoprecipitation (IP) assay**

1320 To map the GluN2D interactome, cultured SMCs sorted from P0 *SMA-*
1321 *creER:Ai14* mice brain parenchymal tissue (via tdTomato-based sorting) were
1322 collected and subsequently expanded in SMCM. At ~90% confluence, cells
1323 were transduced with lentivirus encoding Grin2d-3XFlag (*Lenti-EF1-EGFP-*
1324 *CMV-Grin2d-3XFlag-WPRE*, 5 × 10^{12} VG/mL). One-week post-transduction,
1325 infected cells (EGFP-tdTomato double positive) were purified using an MA-900
1326 sorter and expanded in 10 cm dishes. Upon reaching 90% confluence, cells

1327 were lysed in RIPA buffer. Lysates were incubated with Anti-GluN2D or IgG
1328 control antibodies conjugated to Protein G Magnetic Beads (Epizyme, Cat#
1329 YJ002) to pull down the protein complex. Eluates were analyzed via Western
1330 blot and mass spectrometry.

1331

1332 **Blood-Brain Barrier (BBB) permeability assay**

1333 To evaluate BBB integrity, the Evans Blue dye extravasation assay was
1334 performed.[96] Mice were injected retro-orbitally with 2% Evans Blue (Merck,
1335 Cat# E2129; dissolved in saline; 4 μL/g). 45 min post-injection, mice were
1336 anesthetized, and whole brains were harvested. Macroscopic dye leakage was
1337 first assessed qualitatively using a Zeiss Axio Zoom V16 microscope. For
1338 quantitative assessment, brains were weighed and homogenized in 1 mL of 50%
1339 trichloroacetic acid (Merck, Cat# 190780). Following centrifugation at 10,000 ×
1340 g for 20 min at 4 °C, the supernatant was collected, and Evans Blue
1341 concentration was quantified by measuring absorbance at 620 nm. To detect
1342 microscopic leakage, immunofluorescence staining for Immunoglobulin G (IgG)
1343 was performed as described in the Immunofluorescence Staining section. We
1344 utilized brain sections from mice subjected to non-perfusion as positive
1345 controls—defining their mean fluorescence intensity as the 100% benchmark—
1346 to quantify the IgG intensity.

1347

1348 **Colorectal endoscopy**

1349 To assess stress-induced gastrointestinal pathology, representative images of
1350 the distal colon were captured using the ENDOQ colonoscopy system. To
1351 ensure unbiased evaluation, a gastroenterologist blinded to the experimental
1352 groups scored mucosal morphology and signs of inflammation based on the
1353 endoscopic images.

1354

1355 **Hematoxylin and Eosin (H&E) staining**

1356 For histological analysis, mice were anesthetized and perfused as described
1357 above. Harvested tissues were post-fixed in 4% PFA for 6 hours at 4 °C.
1358 Following standard paraffin embedding, 8 μm sections were cut (Histo.
1359 Microtome, Leica FC-LRM), and H&E staining was performed to visualize gross
1360 morphological structures.

1361

1362 **Topological characterization of BLA activation patterns**

1363 To objectively classify emotional states based on the spatial configuration of
1364 neuronal ensembles, a topology-based estimation framework was developed,
1365 integrating the Structural Similarity Index (SSIM) with unsupervised hierarchical
1366 clustering.

1367 To transition from discrete cellular signals to a continuous representation

of regional activation, raw c-Fos immunofluorescence staining images were preprocessed in MATLAB. Images were converted to greyscale, inverted, and normalized to a [0, 1] intensity scale. A multi-scale Gaussian smoothing protocol ($\sigma 1$ = 6 pixels, $\sigma 2$ = 12 pixels) was applied to generate a continuous spatial intensity map representing the macro-scale topography of neuronal activation within the BLA. This step effectively minimizes high-frequency noise from individual cell variations while preserving the global spatial structure.

To quantify the topological similarity between experimental conditions, pairwise SSIM values were computed between the activation intensity maps. Unlike traditional metrics that rely on absolute cell counts or pixel-by-pixel subtraction, SSIM assesses the preservation of structural information by integrating comparisons of luminance (l), contrast (c), and structure (s). The similarity index between image x and y is calculated as:

$$\mathrm{SSIM}(x, y) = [l(x, y)]^{\alpha} \cdot [c(x, y)]^{\beta} \cdot [s(x, y)]^{\gamma}$$

This metric provides a robust measure of spatial fidelity, converting image-based topographical correlations into a numerical similarity matrix.

The resulting SSIM similarity matrix was utilized for cluster analysis in R. We defined the topological distance (D) between any two conditions as $D = 1 - \mathrm{SSIM}$. Based on this distance matrix, unsupervised hierarchical clustering was performed using Ward's minimum variance method (method = "ward.D2"). This algorithm minimizes total within-cluster variance to construct a dendrogram,

effectively grouping behavioral contexts into distinct clusters based purely on topological proximity. These naturally emerging clusters were then mapped to discrete stress Levels (Levels 0–3), defining the subject's state based on the intrinsic topology of their neuronal response rather than arbitrary thresholds.

To ensure rigor, a double-blind workflow was implemented: image processing and algorithmic analysis were conducted by two independent analysts, distinct from the personnel performing wet-lab experiments. Statistical analyses were performed using GraphPad Prism (v9.4.1) and custom MATLAB scripts. All source code is available at website in the Github shown below: https://github.com/JialabEleven/Functional_hyperemia_regulates_emotion-master.

Serial Block-Face Scanning Electron Microscopy (SBF-SEM)

To visualize the ultrastructure of the neurovascular interface, we prepared specimens consistent with our previous protocols.[38] Briefly, we identified ascending venules using X-ray microscopy (Zeiss Xradia 520 Versa) at 4 × magnification (80 kV). We mounted the specimen on an aluminum pin using conductive epoxy (Chemtronics, CW2400) and trimmed it into a 600 × 600 × 700 μm^3 block using a glass knife and a diamond trimming knife (DiATOME, Trim 90). Prior to imaging, we sputter-coated the sample with gold–palladium (Leica EM ACE200). We acquired images using a Carl Zeiss Gemini 300

1410 scanning electron microscope equipped with a Gatan 3View ultramicrotome
1411 and a BSE detector. Imaging parameters were set to 2 kV acceleration voltage
1412 under high vacuum (~1.8 × 10^{-3} mBar) with focal charge compensation. We
1413 performed serial sectioning at a thickness of 50–75 nm with a cutting speed of
1414 0.1 mm/s.

1415

1416 **Stroke modelling**

1417 To validate the absence of hypoxic injury in our optogenetic model, we
1418 generated a positive control for hypoxia using the Stroke Induced by Magnetic
1419 ParticLEs (SIMPLE) method.[58-60] Briefly, we injected magnetic microparticles
1420 into the bloodstream and positioned a magnet over the middle cerebral artery
1421 (MCA) to induce targeted occlusion. This permanent ischemia triggers robust
1422 upregulation of Hypoxia-inducible factor 1-alpha (HIF-1α) within 24 hours. We
1423 utilized brain sections from mice subjected to the SIMPLE stroke model as
1424 positive controls—defining their mean fluorescence intensity in the stroke
1425 infarct area as the 100% benchmark—to quantify HIF-1α expression.

1426

1427 **Software, code, and data availability**

1428 Fluorescence images were processed using Zeiss Zen Lite (v3.4) and ImageJ
1429 (v1.53u). For fiber photometry, signal demodulation and linear regression
1430 correction were performed using the system's built-in proprietary software

(Thinkertech). Whisker stimulation data were acquired and analyzed using the RWD LSCI software (v5.0). Trajectory tracking for the OFTs, complex OFT, and EPM was performed using the Noldus EthoVision XT system (v18), which was also utilized to generate locomotion heatmaps. For the Looming and VR_{eagle} assays, tracking was conducted using custom scripts (Bayonne). Physiological and Topology Analysis: Custom MATLAB scripts were developed to analyze CBF peak kinetics, map aggregate defecation coordinates, and generate neural activation heatmaps for the topology-based estimation framework. KEGG pathway enrichment analysis and SSIM-based hierarchical clustering were executed using custom R algorithms. Statistical analyses were conducted using GraphPad Prism (v9.4.1) and MATLAB. Figures were assembled using Adobe Illustrator 2024 (v28.3). Outliers were identified and excluded using the Interquartile Range (IQR) method (values falling outside the range of Q1 − 1.5 × IQR to Q3 + 1.5 × IQR).[97] Data are expressed as mean ± standard error of the mean (SEM). The normality of data distribution was assessed using the Shapiro-Wilk test. Specific statistical tests employed for each experiment are detailed in the corresponding figure legends. Exact *P* values are reported to four decimal places. A *P* value < 0.05 was considered statistically significant. Statistical analyses were performed using GraphPad Prism (v9.4.1). A comprehensive data resource checklist, detailing figure attributions and sample sources, is provided in Supplementary Table S2 for reference. Furthermore, to ensure maximum transparency and statistical robustness, the percentage of c-

Fos positive neurons in the BLA across all experimental cohorts is quantified and presented in Supplementary Figure S24. All custom MATLAB and R code generated for the topology-based estimation framework and hemodynamic analysis is available at the GitHub website for free searching and use: https://github.com/JialabEleven/Functional_hyperemia_regulates_emotion-master.

REFERENCES

1 Roelofs K, Bramson B, Toni I. A neurocognitive theory of flexible emotion control: The role of the lateral frontal pole in emotion regulation. *Ann N Y Acad Sci* 2023; **1525**:28-40.

2 Bortolon C, Chen S, Bonanno GA. Components of emotion regulation flexibility and psychosis: The association between psychosis-proneness and context sensitivity. *Br J Clin Psychol* 2023; **62**:82-95.

3 D'Agostino A, Covanti S, Rossi Monti M, Starcevic V. Reconsidering Emotion Dysregulation. *Psychiatr Q* 2017; **88**:807-825.

4 Easdale-Cheele T, Parlatini V, Cortese S, Bellato A. A Narrative Review of the Efficacy of Interventions for Emotional Dysregulation, and Underlying Bio-Psycho-Social Factors. *Brain Sci* 2024; **14**.

5 De Prisco M, Oliva V, Fico G *et al.* Emotion dysregulation in bipolar disorder compared to other mental illnesses: a systematic review and meta-analysis.

Psychol Med 2023; **53**:7484-7503.

6 Geng H, Xu P, Aleman A, Qin S, Luo YJ. Dynamic Organization of Large-scale Functional Brain Networks Supports Interactions Between Emotion and Executive Control. *Neurosci Bull* 2024; **40**:981-991.

7 Szaflarski JP, Allendorfer JB, Heyse H, Mendoza L, Szaflarski BA, Cohen N. Functional MRI of facial emotion processing in left temporal lobe epilepsy. *Epilepsy Behav* 2014; **32**:92-99.

8 Etkin A, Wager TD. Functional neuroimaging of anxiety: a meta-analysis of emotional processing in PTSD, social anxiety disorder, and specific phobia. *Am J Psychiatry* 2007; **164**:1476-1488.

9 Mathias EJ, Kenny A, Plank MJ, David T. Integrated models of neurovascular coupling and BOLD signals: Responses for varying neural activations. *Neuroimage* 2018; **174**:69-86.

10 Iadecola C. The Neurovascular Unit Coming of Age: A Journey through Neurovascular Coupling in Health and Disease. *Neuron* 2017; **96**:17-42.

11 Garfinkel SN, Abelson JL, King AP *et al.* Impaired contextual modulation of memories in PTSD: an fMRI and psychophysiological study of extinction retention and fear renewal. *J Neurosci* 2014; **34**:13435-13443.

12 Delvecchio G, Fossati P, Boyer P *et al.* Common and distinct neural correlates of emotional processing in Bipolar Disorder and Major Depressive Disorder: a voxel-based meta-analysis of functional magnetic resonance imaging studies. *Eur Neuropsychopharmacol* 2012; **22**:100-113.

1496 13 Fan Y, Herrera-Melendez AL, Pestke K *et al.* Early life stress modulates
1497 amygdala-prefrontal functional connectivity: implications for oxytocin effects.
1498 *Hum Brain Mapp* 2014; **35**:5328-5339.
1499 14 Yang S, Webb AJS. Reduced neurovascular coupling is associated with
1500 increased cardiovascular risk without established cerebrovascular disease: A
1501 cross-sectional analysis in UK biobank. *J Cereb Blood Flow Metab*
1502 2024:271678x241302172.
1503 15 Kunimatsu A, Yasaka K, Akai H, Kunimatsu N, Abe O. MRI findings in
1504 posttraumatic stress disorder. *J Magn Reson Imaging* 2020; **52**:380-396.
1505 16 Terburg D, Morgan BE, Montoya ER *et al.* Hypervigilance for fear after
1506 basolateral amygdala damage in humans. *Transl Psychiatry* 2012; **2**:e115.
1507 17 Feinstein JS, Adolphs R, Damasio A, Tranel D. The human amygdala and
1508 the induction and experience of fear. *Curr Biol* 2011; **21**:34-38.
1509 18 Han K, Lee M, Lim HK *et al.* Excitation-Inhibition Imbalance Leads to
1510 Alteration of Neuronal Coherence and Neurovascular Coupling under Acute
1511 Stress. *J Neurosci* 2020; **40**:9148-9162.
1512 19 Lee S, Kang BM, Shin MK *et al.* Chronic Stress Decreases Cerebrovascular
1513 Responses During Rat Hindlimb Electrical Stimulation. *Front Neurosci* 2015;
1514 **9**:462.
1515 20 Johnson AC, Uhlig F, Einwag Z, Cataldo N, Erdos B. The neuroendocrine
1516 stress response impairs hippocampal vascular function and memory in male
1517 and female rats. *Neurobiol Dis* 2022; **168**:105717.

1518 21 Shen J, Wang D, Wang X *et al.* Neurovascular Coupling in the Dentate Gyrus
1519 Regulates Adult Hippocampal Neurogenesis. *Neuron* 2019; **103**:878-890 e873.
1520 22 Garthwaite G, Bartus K, Malcolm D *et al.* Signaling from blood vessels to
1521 CNS axons through nitric oxide. *J Neurosci* 2006; **26**:7730-7740.
1522 23 Roy RK, Althammer F, Seymour AJ *et al.* Inverse neurovascular coupling
1523 contributes to positive feedback excitation of vasopressin neurons during a
1524 systemic homeostatic challenge. *Cell Rep* 2021; **37**:109925.
1525 24 Kim KJ, Ramiro Diaz J, Iddings JA, Filosa JA. Vasculo-Neuronal Coupling:
1526 Retrograde Vascular Communication to Brain Neurons. *J Neurosci* 2016;
1527 **36**:12624-12639.
1528 25 Drew PJ. Neurovascular coupling: motive unknown. *Trends Neurosci* 2022;
1529 **45**:809-819.
1530 26 Phillips ML, Drevets WC, Rauch SL, Lane R. Neurobiology of emotion
1531 perception II: Implications for major psychiatric disorders. *Biol Psychiatry* 2003;
1532 **54**:515-528.
1533 27 Hale MW, Hay-Schmidt A, Mikkelsen JD, Poulsen B, Shekhar A, Lowry CA.
1534 Exposure to an open-field arena increases c-Fos expression in a distributed
1535 anxiety-related system projecting to the basolateral amygdaloid complex.
1536 *Neuroscience* 2008; **155**:659-672.
1537 28 Kovacs LA, Schiessl JA, Nafz AE, Csernus V, Gaszner B. Both Basal and
1538 Acute Restraint Stress-Induced c-Fos Expression Is Influenced by Age in the
1539 Extended Amygdala and Brainstem Stress Centers in Male Rats. *Front Aging*

1540 *Neurosci* 2018; **10**:248.

1541 29 Shoji H, Miyakawa T. Effects of test experience, closed-arm wall color, and
1542 illumination level on behavior and plasma corticosterone response in an
1543 elevated plus maze in male C57BL/6J mice: a challenge against conventional
1544 interpretation of the test. *Mol Brain* 2021; **14**:34.

1545 30 Sturman O, Germain PL, Bohacek J. Exploratory rearing: a context- and
1546 stress-sensitive behavior recorded in the open-field test. *Stress* 2018; **21**:443-
1547 452.

1548 31 Kakol-Palm D, Brusberg M, Sand E *et al.* Role of tachykinin NK(1) and NK(2)
1549 receptors in colonic sensitivity and stress-induced defecation in gerbils. *Eur J*
1550 *Pharmacol* 2008; **582**:123-131.

1551 32 Taguchi R, Shikata K, Furuya Y *et al.* Selective corticotropin-releasing factor
1552 1 receptor antagonist E2508 reduces restraint stress-induced defecation and
1553 visceral pain in rat models. *Psychoneuroendocrinology* 2017; **75**:110-115.

1554 33 Monarca RI, Silva RFB, Gabriel SI, Cerveira AM, von Merten S. The
1555 Presence of a Shelter in an Open Field Test Has Differential Effects on the
1556 Behavior and Stress Response of Two Mouse Species. *J Exp Zool A Ecol Integr*
1557 *Physiol* 2025; **343**:480-492.

1558 34 An W, Zhang Y, Zhou A, Hu Y. Detrimental Effects of Restricted Cage Size
1559 on Reproductive Performance, Exploration Ability, and Anxiety but Not Working
1560 Memory of Kunming Mice. *Front Behav Neurosci* 2021; **15**:651782.

1561 35 Powell WH, Annett LE, Depoortere R, Newman-Tancredi A, Iravani MM. The

1562 selective 5-HT(1A) receptor agonist NLX-112 displays anxiolytic-like activity in
1563 mice. *Naunyn Schmiedebergs Arch Pharmacol* 2022; **395**:149-157.
1564 36 Chen K, Gupta R, Martin-Avila A, Cui M, Xie Z, Yang G. Anesthesia-induced
1565 hippocampal-cortical hyperactivity and tau hyperphosphorylation impair remote
1566 memory retrieval in Alzheimer's disease. *Alzheimers Dement* 2024; **20**:494-510.
1567 37 Khalil V, Faress I, Mermet-Joret N, Kerwin P, Yonehara K, Nabavi S.
1568 Subcortico-amygdala pathway processes innate and learned threats. *Elife* 2023;
1569 **12**.
1570 38 Zhang D, Ruan J, Peng S *et al.* Synaptic-like transmission between neural
1571 axons and arteriolar smooth muscle cells drives cerebral neurovascular
1572 coupling. *Nat Neurosci* 2024; **27**:232-248.
1573 39 Monyer H, Burnashev N, Laurie DJ, Sakmann B, Seeburg PH.
1574 Developmental and regional expression in the rat brain and functional
1575 properties of four NMDA receptors. *Neuron* 1994; **12**:529-540.
1576 40 Laurie DJ, Bartke I, Schoepfer R, Naujoks K, Seeburg PH. Regional,
1577 developmental and interspecies expression of the four NMDAR2 subunits,
1578 examined using monoclonal antibodies. *Brain Res Mol Brain Res* 1997; **51**:23-
1579 32.
1580 41 Qiu YM, Zhang CL, Chen AQ *et al.* Immune Cells in the BBB Disruption After
1581 Acute Ischemic Stroke: Targets for Immune Therapy? *Front Immunol* 2021;
1582 **12**:678744.
1583 42 Dion-Albert L, Dudek KA, Russo SJ, Campbell M, Menard C. Neurovascular

1584 adaptations modulating cognition, mood, and stress responses. *Trends*
1585 *Neurosci* 2023; **46**:276-292.
1586 43 Oyarzabal EA, Hsu LM, Das M *et al.* Chemogenetic stimulation of tonic locus
1587 coeruleus activity strengthens the default mode network. *Sci Adv* 2022;
1588 **8**:eabm9898.
1589 44 Chao TH, Zhang WT, Hsu LM, Cerri DH, Wang TW, Shih YI. Computing
1590 hemodynamic response functions from concurrent spectral fiber-photometry
1591 and fMRI data. *Neurophotonics* 2022; **9**:032205.
1592 45 Liu X, Li C, Falck JR, Roman RJ, Harder DR, Koehler RC. Interaction of
1593 nitric oxide, 20-HETE, and EETs during functional hyperemia in whisker barrel
1594 cortex. *Am J Physiol Heart Circ Physiol* 2008; **295**:H619-631.
1595 46 Renic M, Klaus JA, Omura T *et al.* Effect of 20-HETE inhibition on infarct
1596 volume and cerebral blood flow after transient middle cerebral artery occlusion.
1597 *J Cereb Blood Flow Metab* 2009; **29**:629-639.
1598 47 Lacroix A, Toussay X, Anenberg E *et al.* COX-2-Derived Prostaglandin E2
1599 Produced by Pyramidal Neurons Contributes to Neurovascular Coupling in the
1600 Rodent Cerebral Cortex. *J Neurosci* 2015; **35**:11791-11810.
1601 48 Lecrux C, Toussay X, Kocharyan A *et al.* Pyramidal neurons are "neurogenic
1602 hubs" in the neurovascular coupling response to whisker stimulation. *J*
1603 *Neurosci* 2011; **31**:9836-9847.
1604 49 Niwa K, Araki E, Morham SG, Ross ME, Iadecola C. Cyclooxygenase-2
1605 contributes to functional hyperemia in whisker-barrel cortex. *J Neurosci* 2000;

1606 **20**:763-770.

1607 50 Hill RA, Tong L, Yuan P, Murikinati S, Gupta S, Grutzendler J. Regional Blood
1608 Flow in the Normal and Ischemic Brain Is Controlled by Arteriolar Smooth
1609 Muscle Cell Contractility and Not by Capillary Pericytes. *Neuron* 2015; **87**:95-
1610 110.

1611 51 Heissler SM, Chinthalapudi K. Structural and functional mechanisms of actin
1612 isoforms. *FEBS J* 2025; **292**:468-482.

1613 52 Li W, Prakash R, Chawla D *et al.* Early effects of high-fat diet on
1614 neurovascular function and focal ischemic brain injury. *Am J Physiol Regul*
1615 *Integr Comp Physiol* 2013; **304**:R1001-1008.

1616 53 Chang HC, Tai YT, Cherng YG *et al.* Resveratrol attenuates high-fat diet-
1617 induced disruption of the blood-brain barrier and protects brain neurons from
1618 apoptotic insults. *J Agric Food Chem* 2014; **62**:3466-3475.

1619 54 Foster DB, Shen LH, Kelly J, Thibault P, Van Eyk JE, Mak AS.
1620 Phosphorylation of caldesmon by p21-activated kinase. Implications for the
1621 Ca(2+) sensitivity of smooth muscle contraction. *J Biol Chem* 2000; **275**:1959-
1622 1965.

1623 55 Yao YB, Xiao CF, Lu JG, Wang C. Caldesmon: Biochemical and Clinical
1624 Implications in Cancer. *Front Cell Dev Biol* 2021; **9**:634759.

1625 56 Vanlandewijck M, He L, Mae MA *et al.* A molecular atlas of cell types and
1626 zonation in the brain vasculature. *Nature* 2018; **554**:475-480.

1627 57 Hauglund NL, Andersen M, Tokarska K *et al.* Norepinephrine-mediated slow

1628 vasomotion drives glymphatic clearance during sleep. *Cell* 2025; **188**:606-622
1629 e617.
1630 58 Lan Y, Zhang X, Liu S *et al.* Fate mapping of Spp1 expression reveals age-
1631 dependent plasticity of disease-associated microglia-like cells after brain injury.
1632 *Immunity* 2024; **57**:349-363 e349.
1633 59 Jia JM, Chowdary PD, Gao X *et al.* Control of cerebral ischemia with
1634 magnetic nanoparticles. *Nat Methods* 2017; **14**:160-166.
1635 60 Jin Y, Shi P, Wang Y *et al.* Precise control of embolic stroke with magnetized
1636 red blood cells in mice. *Commun Biol* 2022; **5**:136.
1637 61 Hu Y, Chen Z, Huang L *et al.* A translational study on looming-evoked
1638 defensive response and the underlying subcortical pathway in autism. *Sci Rep*
1639 2017; **7**:14755.
1640 62 Shang C, Chen Z, Liu A *et al.* Divergent midbrain circuits orchestrate escape
1641 and freezing responses to looming stimuli in mice. *Nat Commun* 2018; **9**:1232.
1642 63 Wang L, Chen IZ, Lin D. Collateral pathways from the ventromedial
1643 hypothalamus mediate defensive behaviors. *Neuron* 2015; **85**:1344-1358.
1644 64 Silva BA, Gross CT, Graff J. The neural circuits of innate fear: detection,
1645 integration, action, and memorization. *Learn Mem* 2016; **23**:544-555.
1646 65 Clewett D, Gasser C, Davachi L. Pupil-linked arousal signals track the
1647 temporal organization of events in memory. *Nat Commun* 2020; **11**:4007.
1648 66 Grunewald N, Jan A, Salvatico C *et al.* Sequences Flanking the Gephyrin-
1649 Binding Site of GlyRbeta Tune Receptor Stabilization at Synapses. *eNeuro*

1650 2018; **5**.

1651 67 Chiba S, Numakawa T, Ninomiya M, Richards MC, Wakabayashi C, Kunugi
1652 H. Chronic restraint stress causes anxiety- and depression-like behaviors,
1653 downregulates glucocorticoid receptor expression, and attenuates glutamate
1654 release induced by brain-derived neurotrophic factor in the prefrontal cortex.
1655 *Prog Neuropsychopharmacol Biol Psychiatry* 2012; **39**:112-119.

1656 68 Cui Y, Yang Y, Ni Z *et al.* Astroglial Kir4.1 in the lateral habenula drives
1657 neuronal bursts in depression. *Nature* 2018; **554**:323-327.

1658 69 Lee S, Kang BM, Kim JH *et al.* Real-time in vivo two-photon imaging study
1659 reveals decreased cerebro-vascular volume and increased blood-brain barrier
1660 permeability in chronically stressed mice. *Sci Rep* 2018; **8**:13064.

1661 70 Masamoto K, Hirase H, Yamada K, Kanno I. Neurovascular coupling-What
1662 next? *Prog Brain Res* 2016; **225**:269-272.

1663 71 Malezieux M, Klein AS, Gogolla N. Neural Circuits for Emotion. *Annu Rev*
1664 *Neurosci* 2023; **46**:211-231.

1665 72 Yamasaki E, Thakore P, Ali S *et al.* Impaired intracellular Ca(2+) signaling
1666 contributes to age-related cerebral small vessel disease in Col4a1 mutant mice.
1667 *Sci Signal* 2023; **16**:eadi3966.

1668 73 Liu Z, Le Q, Lv Y *et al.* A distinct D1-MSN subpopulation down-regulates
1669 dopamine to promote negative emotional state. *Cell Res* 2022; **32**:139-156.

1670 74 Chipperfield AR, Harper AA. Chloride in smooth muscle. *Prog Biophys Mol*
1671 *Biol* 2000; **74**:175-221.

1672 75 Ben-Ari Y. Excitatory actions of gaba during development: the nature of the
1673 nurture. *Nat Rev Neurosci* 2002; **3**:728-739.
1674 76 Runegaard AH, Sorensen AT, Fitzpatrick CM *et al.* Locomotor- and Reward-
1675 Enhancing Effects of Cocaine Are Differentially Regulated by Chemogenetic
1676 Stimulation of Gi-Signaling in Dopaminergic Neurons. *eNeuro* 2018; **5**.
1677 77 Seibenhener ML, Wooten MC. Use of the Open Field Maze to measure
1678 locomotor and anxiety-like behavior in mice. *J Vis Exp* 2015:e52434.
1679 78 Ma Y, Shaik MA, Kim SH *et al.* Correction to 'Wide-field optical mapping of
1680 neural activity and brain haemodynamics: considerations and novel
1681 approaches'. *Philos Trans R Soc Lond B Biol Sci* 2017; **372**.
1682 79 Lerner TN, Shilyansky C, Davidson TJ *et al.* Intact-Brain Analyses Reveal
1683 Distinct Information Carried by SNc Dopamine Subcircuits. *Cell* 2015; **162**:635-
1684 647.
1685 80 Li J, Zhang Y, Zhang D *et al.* Ca(2+) oscillation in vascular smooth muscle
1686 cells control myogenic spontaneous vasomotion and counteract post-ischemic
1687 no-reflow. *Commun Biol* 2024; **7**:332.
1688 81 Zhang YY, Li JZ, Wang WT, Xie HQ, Ruan JY, Jia JM. Vasomotion delineates
1689 cerebral vascular dynamic features and participates in the homeostatic cerebral
1690 blood flow regulation. *Sci Rep* 2025; **15**:36210.
1691 82 Zhang YY, Li JZ, Xie HQ *et al.* High-resolution vasomotion analysis reveals
1692 novel arteriole physiological features and progressive modulation of cerebral
1693 vascular networks by stroke. *J Cereb Blood Flow Metab* 2024; **44**:1330-1348.

1694 83 Stefanovska A, Bracic M, Kvernmo HD. Wavelet analysis of oscillations in
1695 the peripheral blood circulation measured by laser Doppler technique. *IEEE*
1696 *Trans Biomed Eng* 1999; **46**:1230-1239.
1697 84 Kleinfeld D, Mitra PP. Spectral methods for functional brain imaging. *Cold*
1698 *Spring Harb Protoc* 2014; **2014**:248-262.
1699 85 Seo JS, Park JY, Choi J *et al.* NADPH oxidase mediates depressive behavior
1700 induced by chronic stress in mice. *J Neurosci* 2012; **32**:9690-9699.
1701 86 Chen M, Ma S, Liu H *et al.* Brain region-specific action of ketamine as a
1702 rapid antidepressant. *Science* 2024; **385**:eado7010.
1703 87 Longstreth GF, Thompson WG, Chey WD, Houghton LA, Mearin F, Spiller
1704 RC. Functional bowel disorders. *Gastroenterology* 2006; **130**:1480-1491.
1705 88 Arakawa H, Arakawa K, Blanchard DC, Blanchard RJ. Scent marking
1706 behavior in male C57BL/6J mice: sexual and developmental determination.
1707 *Behav Brain Res* 2007; **182**:73-79.
1708 89 Yu XD, Zhu Y, Sun QX *et al.* Distinct serotonergic pathways to the amygdala
1709 underlie separate behavioral features of anxiety. *Nat Neurosci* 2022; **25**:1651-
1710 1663.
1711 90 Liu J, Li D, Huang J *et al.* Glutamatergic Neurons in the Amygdala Are
1712 Involved in Paclitaxel-Induced Pain and Anxiety. *Front Psychiatry* 2022;
1713 **13**:869544.
1714 91 Warden MR, Selimbeyoglu A, Mirzabekov JJ *et al.* A prefrontal cortex-
1715 brainstem neuronal projection that controls response to behavioural challenge.

1716 *Nature* 2012; **492**:428-432.

1717 92 Rampon C, Luppi PH, Fort P, Peyron C, Jouvet M. Distribution of glycine-
1718 immunoreactive cell bodies and fibers in the rat brain. *Neuroscience* 1996;
1719 **75**:737-755.

1720 93 Dunn KW, Kamocka MM, McDonald JH. A practical guide to evaluating
1721 colocalization in biological microscopy. *Am J Physiol Cell Physiol* 2011;
1722 **300**:C723-742.

1723 94 Li X, Zhou L, Zhang X *et al.* Proteins secreted by brain arteriolar smooth
1724 muscle cells are instructive for neural development. *Mol Brain* 2022; **15**:97.

1725 95 Ferris HR, Stine NC, Hill-Eubanks DC, Nelson MT, Wellman GC, Koide M.
1726 Epidermal Growth Factor Receptors in Vascular Endothelial Cells Contribute to
1727 Functional Hyperemia in the Brain. *Int J Mol Sci* 2023; **24**.

1728 96 Hou W, Yao J, Liu J *et al.* USP14 inhibition promotes recovery by protecting
1729 BBB integrity and attenuating neuroinflammation in MCAO mice. *CNS Neurosci*
1730 *Ther* 2023; **29**:3612-3623.

1731 97 Villani AP, Rozieres A, Bensaid B *et al.* Massive clonal expansion of
1732 polycytotoxic skin and blood CD8(+) T cells in patients with toxic epidermal
1733 necrolysis. *Sci Adv* 2021; **7**.

1734

1735 **ACKNOWLEDGMENTS**

1736 We sincerely thank Prof. Bo Li for his invaluable advice and for editing the
1737 manuscript. We are grateful to Prof. Hailan Hu for providing the *Ai32* mice, and

to Prof. Yanmei Tao and Dr. Xu Hu for sharing the *Nestin-Cre* and *Emx1-Cre* lines. We also thank Xiaoxuan Zhang for providing stroke-modeling mice; Xuan Li from Prof. Bo Li's lab for guidance on fiber photometry in the amygdala; and Wuyang Zhang for assisting with data assessment during the revision. We thank Dr. Zhu Zhu for providing critical discussion during the revision. We thank rotation/visiting students Jiaxing Tang, Zeyu Meng, Jiaqi Tu, and Yiran Ge for double-bind analysis of behavioral data. furthermore, we thank the following staff at Westlake University for their technical support: Yi Zhu for sharing psychological insights that facilitated our data interpretation; Yajie Liu at the Laboratory Animal Resource Center (LARC) for guidance on behavioral assays; Dr. Jiongfang Xie at the Microscopy Core Facility for imaging assistance; Dr. Mingzhu Fan at the Mass Spectrometry & Metabolomics Core Facility (MSMCF) for mass spectrometry data collection; and Yanan Tang at the Flow Cytometry Core Facility (FCCF) for assistance with cell sorting.

This work was supported by Westlake Laboratory of Life Sciences and Biomedicine (Project No. 202309002), the National Natural Science Foundation of China (project No. 32571142 and 32170961), State Key Laboratory of Gene Expression (Grant No. 2025ZY01117), Hangzhou Leading Innovation Team (TD2024001), the Joint Fund of the Zhejiang Provincial Natural Science Foundation of China (LHZQN25H160001), the "Pioneer" and "Leading Goose" R&D Program of Zhejiang (grant 2024SSYS0031), and the partially supported from the Construction Fund of Key Medical Disciplines of Hangzhou

(2025HZZD04) from H.W.

AUTHOR CONTRIBUTIONS

J.-M.J. conceived the project, designed the experiments, and supervised this study. J.Y.R. designed and performed key experiments, obtained and organized the majority of original data, and wrote the manuscript draft. X.H.Q. designed the complex OFT, Bristol score assessments, gut health inspection, and S1BF NVC control assays; performed the cluster analysis of topological SSIM data and conducted *Cald1* cisterna magna injections; participated in the 40 cm OFT, looming and VR_{eagle} assays, BBB integrity inspections, and blood sample collection; and provided critical suggestions during the revision. H.Q.X. spearheaded the 3D reconstruction of BLA arterioles by registering tissue-cleared images to the mouse brain atlas; developed a fiber photometry prototype for BLA CBV recording; participated in the Looming and VR_{eagle} assays and blood pressure measurements; and contributed to the assessment of stress-hormone levels. Y.Y.Z. developed the MATLAB-based computational pipeline for functional hyperemia peak detection, mass spectrometry data preprocessing, BLA neural topological analysis, and Fast Fourier Transform (FFT) processing. D.D.Z. provided the raw dataset of the cleared brain of the *SMA-creER:Ai14* mouse, primer pairs of *Grin1*, raw data of the serial electron microscopy, and *SMA-creER:Grin1*$^{f/f}$ 40 cm OFT video raw data. W.T.W. contributed to the writing of MATLAB code with Y.Y.Z.. B.R.Z. participated in the

1782 double-blind genotyping management of mice and cell sorting. D.P.L. helped

1783 the mouse brain section after 35 cm OFT. Y.X.N illustrated the KEGG maps.

1784

1785 **CONFLICT OF INTERESTS**

1786 The authors declare no competing interests.

1787

1788 **FIGURE LEGENDS**

1789 **Fig.1 Validation of defecation bouts as a robust quantitative index of**
1790 **negative emotional states. a** Experimental design for home cage (HC), open
1791 field tests (OFTs), and acute restraint stress (ARS) assays. **b, c** Representative
1792 images (**b**) and quantification (**c**) of BLA neuronal activation across different
1793 stress paradigms shown in (**a**). One-way ANOVA followed by Tukey's multiple
1794 comparisons test ($P < 0.0001$). **d** Quantification of defecation bouts under the
1795 paradigms shown in (**a**). Kruskal-Wallis test followed by Dunn's multiple
1796 comparisons test ($P < 0.0001$). **e** Linear correlation between BLA c-Fos-positive
1797 neuron counts and defecation bouts. Data were pooled from (**c**) and (**d**). Dotted
1798 lines are SEM. **f, g** Serum corticosterone concentrations (**f**) under the
1799 paradigms shown in (**a**) and their linear correlation with defecation bouts (**g**).
1800 Data were pooled in (**g**) from (**d**) and (**f**). One-way ANOVA followed by Tukey's
1801 multiple comparisons test ($P < 0.0001$). Dotted lines are SEM in (**g**). **h–j** Total
1802 running distance (**h**), time spent in the center zone (**i**), and unsupported rearing
1803 bouts (**j**) in 40 cm and 35 cm OFT. Student's *t*-test (**h**, **i**) and Mann-Whitney test
1804 (**j**). **k** Representative heatmap of zone preference for a single mouse and the
1805 spatial distribution of defecation locations from 15 mice in the 40 cm OFT. Each
1806 dot indicates one defecation location. **l** Statistical quantification of the spatial
1807 distribution data in (**k**). **m** Experimental schematic of chemogenetic inhibition of
1808 BLA neurons using *AAV2/5-hSyn-hM4Di-EGFP*. **n, o** Representative images (**n**)
1809 and quantification (**o**) of BLA neuronal activation under chemogenetic inhibition

in ARS. Student's *t*-test. **p** Quantification of defecation bouts in 40 cm OFT and ARS following BLA chemogenetic inhibition. Mann-Whitney test. **q** Defecation rate and defecation latency in the 40 cm OFT. Sample sizes (*N*) are indicated in the panels. Gehan-Breslow-Wilcoxon test. **r, s** Time spent in the center zone (**r**) and total running distance (**s**) following chemogenetic inhibition in the 40 cm OFT. Student's *t*-test. **t** Defecation bouts in the 40 cm OFT and ARS following BLA injection of the control virus (EGFP). Mann-Whitney test. Except (**k**), each dot represents one mouse. **** indicates $P < 0.0001$. Data are presented as mean ± SEM.

Fig.2 GluN2D in arteriolar SMCs is essential for NVC in S1BF and BLA. a Schematic representation of the neuro-smooth muscle junction (NsMJ) within the neurovascular unit (NVU). **b** Electrophoretogram (top) and quantification (bottom) of mRNA levels for NMDA receptor subunits via RT-PCR in cultured SMCs sorted from P0 brain parenchymal tissue. P0 cerebellum lysates used as benchmark. Arrows indicate bands' locations. **c** Validation of *Grin2d* expression via RNAscope. Top: representative image from the cortex of brain slice (yellow dotted line indicates the arteriolar SMC boundary). Middle: representative fluorescence intensity linescan of the region indicated by white arrows. Bottom: Pearson's correlation coefficient analysis. Each dot represents one linescan region from one mouse. **d, e** Representative images (**d**) and quantification (**e**) of GluN2D immunofluorescence (IF) staining in the middle cerebral artery

1832 (MCA). Each dot represents one analysis region of MCA from a single mouse.
1833 Student's *t*-test. **f-g** Experimental schematic (**f**) and whisker-evoked functional
1834 hyperemia in the S1BF (**g**). Panel (**g**) left: time-series traces of functional
1835 hyperemia; shaded areas represent SEM across mice. Panel (**g**) right:
1836 quantification of the functional hyperemia plateau phase. One-way ANOVA
1837 followed by Tukey's multiple comparisons test ($P < 0.0001$). Floxed control mice
1838 group including comparable 8 *Grin2d*$^{f/f}$ mice and 7 *Grin1*$^{f/f}$ mice. **h** Schematic
1839 for concurrent recording of CBV (Through Rhodamine) and neuronal Ca^{2+}
1840 (Through *AAV2/9-hSyn-GCaMP8f*) signals in the BLA. **i, j** Time-series
1841 recordings of BLA CBV (**i**) and Ca^{2+} signals (**j**) during the 15-min (900 s) 40 cm
1842 OFT session. Shaded areas represent SEM across mice. **k** Area under curve
1843 (AUC) quantification of the first 5 minutes of CBV and Ca^{2+} responses from data
1844 in (**i**) and (**j**). Student's *t*-test. **l, m** Representative images (**l**) and quantification
1845 (**m**) of BLA neuronal activation following the 40 cm OFT. Student's *t*-test. Except
1846 (**c** and **e**), each dot represents one mouse. **** indicates $P < 0.0001$. Data are
1847 presented as mean ± SEM. See also Supplementary information, Figs. S1–S8.

1848

1849 **Fig.3 Systemic SMC-specific GluN2D deficiency-driven negative**
1850 **emotionality is pharmacologically rescued via BLA local intervention. a**
1851 Defecation bout in the 40 cm OFT shown in 5-minute intervals. Mann-Whitney
1852 test. **b** Comparison of defecation bouts across HC (Home cage), OFTs, and
1853 ARS paradigms. Kruskal-Wallis test followed by Dunn's multiple comparisons

1854 test (P = 0.0365). **c** Defecation rate and defecation latency in the OFTs. Sample
1855 sizes (N) are indicated in the panels. Gehan-Breslow-Wilcoxon test. **d**
1856 Unsupported rearing bouts (left) and serum corticosterone concentrations (right)
1857 in the 40 cm OFT. Mann-Whitney test (left) and Student's *t*-test (right). **e**
1858 Experimental schematic of systemic HET0016 administration. **f, g**
1859 Representative images (**f**) and quantification (**g**) of BLA neuronal activation
1860 following systemic HET0016 treatment in the 40 cm OFT. Two-way ANOVA
1861 followed by Tukey's multiple comparisons test (P = 0.0104). **h–j** Quantification
1862 of defecation bouts (**h**), defecation rate and latency (**i**), and unsupported rearing
1863 bouts and serum corticosterone concentrations (**j**) in the 40 cm OFT following
1864 systemic HET0016 administration. Two-way ANOVA on rank-transformed data
1865 followed by Sidak's multiple comparisons test (**h**, P < 0.0001; **j left**, P = 0.00003),
1866 Gehan-Breslow-Wilcoxon test (**i**), and Two-way ANOVA followed by Tukey's
1867 multiple comparisons test (**j right**, P = 0.0212). Sample sizes (N) are indicated
1868 in the panel (**i**). **k** Experimental schematic of local BLA microinjection of
1869 HET0016. **l, m** Representative images (**l**) and quantification (**m**) of BLA
1870 neuronal activation following local BLA HET0016 treatment in the 40 cm OFT.
1871 Two-way ANOVA followed by Tukey's multiple comparisons test (P < 0.0001).
1872 **n–p** Quantification of defecation bouts (**n**), defecation rate and latency (**o**), and
1873 unsupported rearing bouts and serum corticosterone concentrations (**p**) in the
1874 40 cm OFT following local BLA HET0016 administration. Two-way ANOVA on
1875 rank-transformed data followed by Sidak's multiple comparisons test (**n**, P <

1876 0.0001, **p left**, P = 0.0020), Gehan-Breslow-Wilcoxon test (**o**), and Two-way
1877 ANOVA followed by Tukey's multiple comparisons test (**p right,** P = 0.0190).
1878 Sample sizes (N) are indicated in the panel (**o**). Each dot represents one mouse.
1879 **** indicates P < 0.0001. Data are presented as mean ± SEM. Detailed
1880 statistical data for panel (**c**, **i**, and **o**) are shown in the supplementary table S1,
1881 sub-table 1-3. See also Supplementary information, Figs. S9–S12.

1882

1883 **Fig.4 Caldesmon interacts with GluN2D in the SMCs to regulate**
1884 **neurovascular coupling and further modulate emotional states. a** KEGG
1885 pathway analysis of GluN2D-interacting proteins identified via proteomic
1886 analysis from cultured SMCs sorted from P0 brain parenchymal tissue. **b**
1887 Immunoprecipitation validation of the interaction between GluN2D and
1888 caldesmon from cultured SMCs sorted from P0 brain parenchymal tissue. **c**
1889 Experimental schematic for whole-brain (left) and local BLA (right) *Cald1*
1890 knockdown (KD) using siRNA. **d, e** Representative images (**d**) and
1891 quantification (**e**) of caldesmon immunofluorescence (IF) staining. Student's *t*-
1892 test. **f** Electrophoretogram (top) and quantification (bottom) of *Cald1* mRNA
1893 expression in the cortex lysates following whole-brain *Cald1* siRNA injection.
1894 Student's *t*-test. **g, h** Representative immunofluorescence (IF) images of
1895 caldesmon in the BLA (**g**) and ventromedial hypothalamus (VMH, **h**) of mice
1896 received local BLA *Cald1* siRNA injection. **i** Quantification of caldesmon
1897 expression levels from the experiments shown in (**g, h)**. Student's *t*-test. **j, k**

1898 Functional hyperemia in the S1BF during whisker stimulation (**j**) and
1899 quantification of the plateau phase (**k**). Shaded areas represent SEM across
1900 mice. One-way ANOVA followed by Tukey's multiple comparisons test (P =
1901 0.0041). Floxed control mice group including comparable 3 mice with cisterna
1902 magna scramble siRNA injection and 3 mice with local BLA scramble siRNA
1903 injection. **l, m** Representative images (**l**) and quantification (**m**) of BLA neuronal
1904 activation in the 40 cm OFT. One-way ANOVA followed by Tukey's multiple
1905 comparisons test (P < 0.0001). **n** Unsupported rearing bouts in the 40 cm OFT.
1906 Kruskal-Wallis test followed by Dunn's multiple comparisons test (P = 0.0001).
1907 **o** Serum corticosterone concentrations in the 40 cm OFT. One-way ANOVA
1908 followed by Tukey's multiple comparisons test (P = 0.0013). **p, q** Defecation
1909 bouts (**p**), defecation rate, and latency (**q**) in the 40 cm OFT. Kruskal-Wallis test
1910 followed by Dunn's multiple comparisons test (**p**, P < 0.0001) and Gehan-
1911 Breslow-Wilcoxon test (**q**). Sample sizes (N) are indicated between panels (**p**
1912 and **q**). Each dot represents one mouse. **** indicates P < 0.0001. Data are
1913 presented as mean ± SEM. Detailed statistical data for panel (**q**) are shown in
1914 the supplementary table S1, sub-table 4. See also Supplementary information,
1915 Figs. S13–S14.

1916

1917 **Fig.5 Optogenetic vascular clamping in the BLA is sufficient to drive**
1918 **negative emotionality. a, b** Experimental schematic showing the fiber optic
1919 implantation site (**a**) and the setup for optogenetic stimulation in a freely moving

1920 mouse within the home cage (**b**). **c, d** Representative CBV traces showing
1921 optogenetically induced CBV changes under various stimulation protocols (**c**)
1922 and the corresponding quantification (**d**). Each dot represents the area under
1923 curve (AUC) change from one mouse during the stimulation period. Shaded
1924 areas represent SEM across mice. One-way ANOVA followed by Tukey's
1925 multiple comparisons test (P < 0.0001). **e–g** Experimental schematic (**e**),
1926 representative CBV traces (**f**), and quantification (**g**) in the 40 cm OFT under
1927 optogenetic vascular clamping. Each dot represents the AUC change during
1928 the optogenetic stimulation from one mouse in (**g**). Shaded areas represent
1929 SEM across mice in (**f**). Dotted lines in (**f**) indicate X = 0 and Y = 0. Student's *t*-
1930 test. **h, i** Representative images (**h**) and quantification (**i**) of BLA neuronal
1931 activation following optogenetic stimulation in the 40 cm OFT. Student's *t*-test.
1932 **j–m,** Quantification of unsupported rearing bouts (**j**), serum corticosterone
1933 concentrations (**k**), defecation bouts (**l**), and defecation rate and latency (**m**) in
1934 the 40 cm OFT during optogenetic stimulation. Coloured dotted lines in (**m**)
1935 indicate the median defecation latency for each group. Mann-Whitney test (**j**, **l**),
1936 Student's t-test (**k**), and Gehan-Breslow-Wilcoxon test (**m**). Sample sizes (N)
1937 are indicated in the panel (**m**). **n, o** Experimental schematic of 15-min home
1938 cage optogenetic stimulation (**n**, **top**), corresponding BLA CBV response (**n**,
1939 **bottom**), and quantification (**o**). Each dot represents the area under curve
1940 (AUC) change during the optogenetic stimulation from one mouse in the home
1941 cage. Shaded areas represent SEM across mice. Student's *t*-test. **p**

1942 Quantification of defecation bouts during home cage optogenetic stimulation.
1943 Colored numbers indicate the mean defecation bouts for each group. Kruskal-
1944 Wallis test followed by Dunn's multiple comparisons test (P < 0.0001). **q, r**
1945 Representative images (**q**) and quantification (**r**) of BLA neuronal activation (**r**
1946 **left**) and serum corticosterone concentrations (**r right**) in the home cage
1947 optogenetic stimulation. Student's *t*-test. Each dot represents one mouse. ****
1948 indicates P < 0.0001. Data are presented as mean ± SEM. See also
1949 Supplementary information, Figs. S15–S16.

1950

1951 **Fig.6 Compromised NVC impairs defensive sustainability and alters BLA**
1952 **neural topological scaling. a, b** Time-series plots (**a**) and heatmaps (**b**)
1953 profiling locomotion speed dynamics before (**a, blue region**) and during (**a,**
1954 **yellow region**) looming stimulation. shaded areas represent SEM across mice
1955 in (**a**). The yellow dotted box in (**b**) indicates the 3-second looming duration. **c,**
1956 **d** Quantification of the accumulated recovery latency from freezing (**c**) and
1957 unsupported rearing bouts 5 min before and after looming stimulation (**d**). N =
1958 15 mice per group. Kolmogorov-smirnov test (**c**) and Two-way ANOVA on rank-
1959 transformed data followed by Sidak's multiple comparisons test (**d**, P < 0.0001).
1960 **e** Experimental schematic of the virtual reality facility for visual threat stimulation.
1961 **f** Time-series traces showing normalized pupil diameter and locomotion speed
1962 during (0–3 s) and after (3–6 s) VR_{eagle} stimulation. The blue region (first 1.5 s)
1963 indicates the eagle call, and the yellow region (1.5–3.0 s) indicates the eagle

1964 diving phase. Representative images of the VR_{eagle} stimulus and the mouse eye
1965 with a clearly visualized pupil are shown on the bottom. Shaded areas represent
1966 SEM across mice. **g, h** Quantification of defensive offset phase (**g**) dynamics
1967 and recovery latencies for pupil diameter and locomotion (**h**) from the data in
1968 (**b** and **f**). *N* = 7 mice per group in VR_{eagle} assay, and *N* = 15 mice per group in
1969 looming assay. Student's *t*-test. **i** Experimental schematic of the complex open
1970 field test (c-OFT) arena. **j** Quantification of BLA neuronal activation in contexts
1971 of home cage, 40 cm OFT, 35 cm OFT, c-OFT, Looming, and VR_{eagle} assays.
1972 Data of 40 cm OFT groups are shared with **Fig. 2m**. Student's *t*-test. **k**
1973 Defecation bouts of mice in the c-OFT. Mann-Whitney test. **l, m** Structural
1974 Similarity Index (SSIM)-based unbiased classification of BLA c-Fos topological
1975 patterns across seven standard stress contexts in littermate control mice (**l**) and
1976 *Grin2d*-cKO mice (**m**). Heatmaps indicate the modified c-Fos intensity in the
1977 BLA (processing details can be seen in the supplementary information, **Figure**
1978 **S18a**). **** indicates $P < 0.0001$. Data are presented as mean ± SEM. See also
1979 Supplementary information, Figs. S17–S18.

1980

1981 **Fig.7 Mural cell-specific GlyRβ deficiency establishes an enhancement**
1982 **model for NVC. a, b** Representative RNAscope images (**a**) and quantification
1983 (**b**) of *Glrb* mRNA expression via RNAscope in arteriolar SMCs (aSMCs) and
1984 venous SMCs (vSMCs) from brain slices. Each dot represents one dot per
1985 mural cell; *N* = 4 mice per group. Mann-Whitney test. **c–e** Representative

1986 images of GlyRβ immunofluorescence from brain slices (**c**) and quantification
1987 comparing arterioles vs. venules in littermate control mice (**d**) and venules
1988 between littermate control and *Glrb*-cKO mice (**e**). In panel (**d**), each dot
1989 represents the number of clusters per 10 μm vessel; N = 4 mice per group. In
1990 panel (**e**), each dot represents one analysis region of vascular mural cells from
1991 a single mouse. Mann-Whitney test (**d**) and Student's *t*-test (**e**). **f**
1992 Electrophoretogram (top) and quantification (bottom) of *Glrb* mRNA expression
1993 in acute sorted Pdgfrβ-positive parenchymal mural cells compared with P60
1994 medullary reticular formation lysates (as positive control). Each dot represents
1995 one mouse. One-way ANOVA followed by Tukey's multiple comparisons test (P
1996 < 0.0001). **g** Co-localization of GlyRβ with gephyrin in cultured human umbilical
1997 venous SMCs (HU-vSMCs). The panel on the right shows the Pearson's
1998 correlation coefficient analysis. Each dot represents the mean correlation
1999 coefficient of ten cells from an independent biological replicate. **h** Co-
2000 localization of GlyRβ with glycinergic axon terminals in the cortex of brain slice.
2001 The orange dotted box indicates the magnified area. Top right: Pearson's
2002 correlation coefficient analysis. Bottom right: Fluorescence intensity linescan
2003 across the region indicated by the white arrow. Each dot represents one
2004 linescan region from one mouse. **i** Sequential electron microscopy (EM)
2005 sections of an ascending venule in the mouse cerebral cortex. White arrows
2006 indicate axonal terminals structural contacts with venous SMCs. EC:
2007 endothelial cell; SMC: smooth muscle cell. **j, k** Experimental schematics of the

2008 whisker stimulation paradigm (**j**) and the transgenic mouse mating strategy (**k**).
2009 **l, m** Functional hyperemia in the S1BF during whisker stimulation (**l**) and
2010 quantification of the corresponding plateau phase (**m**). Shaded areas represent
2011 SEM across mice in (**l**). Each dot represents one mouse. One-way ANOVA
2012 followed by Tukey's multiple comparisons test (P < 0.0001). Control data
2013 (*Grin2d*$^{f/f}$ and *Pdgfrβ-creER:Grin2d*$^{f/f}$) are shared with **Fig. S11j**. Floxed control
2014 mice group including comparable 3 *Grin2d*$^{f/f}$ mice, 3 *Glrb*$^{f/f}$ mice, and 3
2015 *Grin2d*$^{f/f}$:*Glrb*$^{f/f}$ mice. **** indicates P < 0.0001. Data are presented as mean ±
2016 SEM. See also Supplementary information, Figs. S19–S20.

2017

2018 **Fig.8 An enhancement model of NVC promotes resilience against acute**
2019 **and chronic emotional distress. a, b** Representative images (**a**) and
2020 quantification (**b**) of BLA neuronal activation in ARS. Student's *t*-test. **c** Serum
2021 corticosterone concentrations in ARS. Student's *t*-test. **d-f** Defecation bouts in
2022 ARS (**d**) and 40 cm OFT (**e**), and defecation rate and latency in the 40 cm OFT
2023 (**f**). Kruskal-Wallis test followed by Dunn's multiple comparisons test (P <
2024 0.0001 for **d** and P = 0.0014 for **e**). Sample sizes (N) are indicated in the panel
2025 (**f**). Gehan-Breslow-Wilcoxon test for (**f**). Floxed control data in (**e** and **f**) (14
2026 *Grin2d*$^{f/f}$ mice and 17 *Pdgfrβ-creER:Grin2d*$^{f/f}$ mice) are shared with **Fig. 3b, c**
2027 and **S12o**, **p**. Floxed control group in (**e**, **f**) contains comparable 14 *Grin2d*$^{f/f}$
2028 mice, 5 *Glrb*$^{f/f}$ mice, and 5 *Grin2d*$^{f/f}$:*Glrb*$^{f/f}$ mice. **g, h** Representative images (**g**)
2029 and quantification (**h**) of BLA neuronal activation in the 40 cm OFT. Student's *t*-

test. **i, j** Unsupported rearing bouts (**i**) and serum corticosterone concentrations (**j**) in the 40 cm OFT. Mann-Whitney test (**i**) and Student's *t*-test (**j**). **k** Experimental schematic of the chronic restraint stress (CRS) paradigm. **l, m** Representative fecal appearance (**l**) and statistical analysis of Bristol scores and defecation bouts during the CRS session (**m**). All fecal scoring was performed by an independent observer blinded to the experimental groups. *N* = 15 mice per group. Two-way ANOVA on rank-transformed data followed by Sidak's multiple comparisons test ($P < 0.0001$). Bristol s.: Bristol score. **n** Immobility time in the forced swim test (FST) after CRS modelling. One-way ANOVA followed by Tukey's multiple comparisons test ($P < 0.0001$). **o, p** Representative images (**o**) and quantification (**p**) of BLA neuronal activation (**p left**) and serum corticosterone concentrations (**p right**) after CRS. Quantification was performed by an independent observer blinded to the experimental groups. One-way ANOVA followed by Tukey's multiple comparisons test ($P < 0.0001$ for **p left**; $P = 0.0400$ for **p right**). **q** Body weight changes during the CRS paradigm. *N* = 15 mice per group. Student's *t*-test. Each dot represents one mouse. **** indicates $P < 0.0001$. Data are presented as mean ± SEM. Detailed statistical data for panel (**f**) are shown in the supplementary table S1, sub-table 5. Naïve indicates mice without CRS modelling as controls. See also Supplementary information, Figs. S21–S23.

Supplementary information

2052 *Supplementary figure legends*

2053 **Fig.S1 Validation of successful GluN2D conditional Knock-out. a, b**
2054 Representative images (**a**) and quantification (**b**) of *Grin1* and *Grin2d* mRNA
2055 expression via RNAscope in the cerebellum. Each dot represents one region of
2056 interest (ROI) from a single brain slice per mouse. Student's *t*-test. **c–e**
2057 Representative immunoblot (top) and quantification (bottom) of GluN2D protein
2058 levels in P0/P60 cerebellum lysates (**c**), cultured SMCs sorted from P0
2059 parenchymal tissue (**d**), and P60 cortex lysates(**e**). Each dot represents one
2060 mouse. One-way ANOVA followed by Tukey's multiple comparisons test for (**c,**
2061 $P < 0.0001$), and Student's *t*-test for (**d**, **e**). **** indicates $P < 0.0001$. Data are
2062 presented as mean ± SEM.

2063

2064 **Fig.S2 Validation of GluN2D expression in peripheral organs' SMCs. a**
2065 Representative low-magnification images of tissue sections from the heart, liver,
2066 spleen, lung, kidney, small intestine, and bladder of *SMA-creER:Ai14* mice (top).
2067 Yellow dotted boxes indicate the magnified areas shown below. White arrows
2068 indicate ROIs for fluorescence intensity linescan analysis. **b** Fluorescence
2069 intensity distribution (linescan) across the ROIs indicated by white arrows in (**a**).
2070 **c** Quantification of GluN2D immunofluorescence (IF) staining intensity of
2071 GluN2D in SMCs across tissues. Each dot represents one mouse. One-way
2072 ANOVA followed by Tukey's multiple comparisons test ($P < 0.0001$). ****

2073 indicates $P < 0.0001$. Data are presented as mean ± SEM.

2074

2075 **Fig.S3 Verification of mouse metabolic status, gut health, and blood-brain**
2076 **barrier integrity. a–h** Quantification of food consumption (**a**), water intake (**b**),
2077 number of fecal pellets (**c**), daily fecal weight (**d**), weight per pellet (**e**), urine
2078 output (**f**), relative body weight changes (**g**), and blood pressure (**h**) measured
2079 in the home cage. For (**a–f**), each dot represents the average value per cage
2080 (4 mice per cage). For (**g, h**), each dot represents an individual mouse. Mann-
2081 Whitney test (**c**) and Student's *t*-test (except **c**). **i** Representative images of
2082 intestinal morphology (appearance and length) and H&E staining of intestinal
2083 sections. **j–n** Quantification of data from (**i**), including mice body weight (**j**),
2084 intestinal length (**k**), intestinal length-to-body weight ratio (**l**), villus length (**m**),
2085 and total 24-hour defecation count (**n**) for mice in the home cage. Each dot
2086 represents one mouse. Student's *t*-test. **o, p** Representative images of the brain
2087 following retro-orbital Evans Blue injection (**o**) and the corresponding
2088 quantification (**p**). Each dot represents one mouse. One-way ANOVA followed
2089 by Tukey's multiple comparisons test ($P = 0.7654$). Data are presented as mean
2090 ± SEM.

2091

2092 **Fig.S4 Validation of SMC marker proteins in *Grin2d*-cKO mice. a**
2093 Representative immunoblot (top) and quantification (bottom) of α-SMA

2094 expression. Each dot represents one mouse. Student's *t*-test. **b** Quantification
2095 of Smoothelin immunofluorescence (IF) staining in the middle cerebral artery
2096 (MCA), corresponding to the representative images in **Fig. 2d**. Each dot
2097 represents one analysis region of MCA from a single mouse. *N* = 4 mice per
2098 group. Student's *t*-test. Data are presented as mean ± SEM.

2099

2100 **Fig.S5 The effect of tamoxifen on NVC. a** Whisker-evoked functional
2101 hyperemia in the S1BF of littermate control mice treated with tamoxifen.
2102 Shaded areas represent SEM across mice. **b** Quantification of the functional
2103 hyperemia plateau phase from the data in (**a**). Each dot represents one mouse.
2104 Student's *t*-test. Data are presented as mean ± SEM.

2105

2106 **Fig.S6 3D-Reconstruction of BLA arteriolar topology through correlative**
2107 **integration of the Allen Brain Atlas with tissue-cleared brains from *SMA-***
2108 ***creER:Ai14* mouse. a** Ventral view of the mouse BLA. Schematic diagram (left)
2109 was adapted from *The Mouse Nervous System* (p. 460, Fig. 14.1), and 3D-
2110 reconstruciton (right) was generated in Imaris using the Allen Mouse Brain
2111 Common Coordinate Framework plugin. BLA is denoted translucent grey. Blue
2112 denotes arteriolar SMCs. Colored lines represent distinct arteriolar segments.
2113 **b** Coronal view of the mouse BLA along with arterioles inside. Colored lines
2114 indicate arterioles in basal amygdala anterior part (BAa), basal amygdala

2115 ventral part (BAv), and lateral amygdala (LA).

2116

2117 **Fig.S7 Calibration and validation of plasma Rhodamine fluorescence**
2118 **intensity. a** Real-time fluorescence intensity measurement following retro-
2119 orbital injection of various Rhodamine concentrations. **b** Linear correlation
2120 between Rhodamine concentration and fluorescence intensity in (**a**). Each dot
2121 represents the average intensity from 120–150 s post-injection for a specific
2122 concentration. **c** Real-time fluorescence intensity measurements following
2123 retro-orbital injection of 5 mg/mL Rhodamine, showing signal stability from 900–
2124 3600 s post-injection.

2125

2126 **Fig.S8 Baseline CBV and OFT performance in *Grin2d*-cKO mice. a** Baseline
2127 CBV in the BLA during the home cage stage. Each dot represents one mouse.
2128 Student's *t*-test. **b, c** Running distance (**b**) and time spent in the center zone (**c**)
2129 in the 40 cm OFT. Each dot represents one mouse. Student's *t*-test. Data are
2130 presented as mean ± SEM.

2131

2132 **Fig.S9 Serum corticosterone concentrations under baseline conditions.**
2133 **a–c** Serum corticosterone concentrations in mice at the home cage condition
2134 (**a**), following i.p. injection of HET0016 (**b**), and following local BLA
2135 microinjection of HET0016 (**c**). Each dot represents one mouse. Student's *t*-

2136 test. Data are presented as mean ± SEM.

2137

2138 **Fig.S10 Dose-dependent and functional validation of HET0016. a** Effects of
2139 different HET0016 concentrations on defecation bouts in ARS. Each dot
2140 represents one mouse. Kruskal-Wallis test followed by Dunn's multiple
2141 comparisons test (P = 0.0005). **b, c** Functional hyperemia in the S1BF during
2142 whisker stimulation (**b**) and quantification of the corresponding plateau phase
2143 (**c**). Shaded areas represent SEM across mice. Each dot represents one mouse.
2144 Paired Student's *t*-test. Data are presented as mean ± SEM.

2145

2146 **Fig.S11 NVC dysfunction across multiple models drives negative**
2147 **emotionality. a–h** Validation of the *Emx1-cre:Ptgs2* model. Experimental
2148 schematic of mating strategy (**a**). Representative images (**b**) and quantification
2149 of neuronal COX-2 (encoded by *Ptgs2*) expression (**c**). Functional hyperemia
2150 in the S1BF (**d, e**), BLA neuronal activation (**f, g**), unsupported rearing bouts (**h,**
2151 **left**), and serum corticosterone (**h, right**) in the 40 cm OFT. **i–r** Validation of the
2152 mural cell-based NMDA conditional knock out models. Mating strategy (**i**),
2153 functional hyperemia (**j**), BLA neuronal activation (**k, l**, and **o, p**). Unsupported
2154 rearing (**m, q**) and serum corticosterone (**n, r**) in the 40 cm OFT. **s–v** Validation
2155 of the *Acta2*-cKO model. Mating strategy (**s**), α-SMA immunoblot quantification
2156 (**t**), and functional hyperemia in the S1BF (**u, v**). **w–aii** Effects of local BLA

2157 HET0016 injection in *Acta2*-cKO mice. Experimental design (**w**), BLA neuronal
2158 activation (**x, y**), serum corticosterone concentrations (**z**), unsupported rearing
2159 bouts (**ai, left**), and defecation bouts (**ai, right**), and defecation rate and latency
2160 in the 40 cm OFT (**aii**) with local BLA HET0016 injection. Each dot represents
2161 one mouse. Shaded areas represent SEM across mice in panel (**d**, **j**, and **u**).
2162 Floxed control mice group in (**j**) including comparable 8 *Grin2d*$^{f/f}$ mice, 7 *Grin1*$^{f/f}$
2163 mice, and 3 *Grin2d*$^{ff/}$*: Grin1*$^{f/f}$ mice. Control data (*Grin2d*$^{f/f}$, *Grin1*$^{f/f}$, *SMA-*
2164 *creER:Grin2d*$^{f/f}$, and *SMA-creER:Grin1*$^{f/f}$) are shared with **Fig. 2g**. Student's *t-*
2165 test (**c**, **e**, **g**, **h right**, **l**, **n**, **p**, **r**, **t**, and **v**). Mann-Whitney test (**h left**, **m**, and **q**).
2166 Two-way ANOVA followed by Tukey's multiple comparisons test for (**y,** P =
2167 0.6564; **z**, P = 0.7144). Two-way ANOVA on rank-transformed data followed by
2168 Sidak's multiple comparisons test (**ai left**, P = 0.4442; **ai right**, P = 0.7932).
2169 One-way ANOVA followed by Tukey's multiple comparisons test (**j**, $P < 0.0001$).
2170 Gehan-Breslow-Wilcoxon test (**aii**). Sample sizes (N) are indicated in the panel
2171 (**aii**). **** indicates $P < 0.0001$. Data are presented as mean ± SEM.

2172

2173 **Fig.S12 HFD-induced NVC dysfunction and its impact on emotional**
2174 **distress. a–d** High-fat diet (HFD) model validation. Schematic (**a**), body weight
2175 changes (**b**), body composition (fat and lean mass) changes (**c**), and food
2176 consumption (**d**) of mice with HFD or normal-fat diet (NFD). Student's *t*-test. N
2177 = 16 mice per group for **b** and **d**, two-way ANOVA followed by Tukey's multiple
2178 comparisons test ($P < 0.0001$). **e-f** Assessment of BBB integrity via Evans Blue

2179 injection (**e**) and quantification (**f**). student's *t*-test. **g, h** Functional hyperemia in
2180 the S1BF (**g**) and quantification of the plateau phase (**h**). shaded areas
2181 represent SEM across mice in (**g**). Student's *t*-test. **i–n** Effects of local BLA
2182 HET0016 injection in HFD mice. Experimental design (**i**), BLA neural activation
2183 (**j, k**), defecation bouts (**l**), defecation rate and latency (**m**), and unsupported
2184 rearing (**n**) of HFD mice in the 40 cm OFT with local BLA HET0016 injection.
2185 Two-way ANOVA followed by Tukey's multiple comparisons test for (**k**), P =
2186 0.0001. Two-way ANOVA on rank-transformed data followed by Sidak's multiple
2187 comparisons test (**l** and **n**), $P < 0.0001$ for (**l**), and $P = 0.0009$ for (**n**). Gehan-
2188 Breslow-Wilcoxon test (**m**). Sample sizes (*N*) are indicated in the panel (**m**). **o,**
2189 **p** Defecation bouts (**o**), and defecation rate and latency (**p**) in the 40 cm OFT
2190 and ARS (panel **o** only). Kruskal-Wallis test followed by Dunn's multiple
2191 comparisons test for (**o**) (P < 0.0001). Gehan-Breslow-Wilcoxon test for (**p**).
2192 Sample sizes (*N*) are indicated in the panels (**o** and **p**). Control data
2193 (*Grin2d*$^{f/f}$and *SMA-creER:Grin2d*$^{f/ff}$) are shared with **Fig. 3a-c**. Detailed
2194 statistical data for panel (**p**) are shown in the supplementary table S1, sub-table
2195 6. Dotted line in (**p**) used to separate two cluster of distribution pattern between
2196 NVC-deficiency groups and their littermate controls. Each dot represents one
2197 mouse. **** indicates $P < 0.0001$. Data are presented as mean ± SEM.

2198

2199 **Fig.S13 Specificity of S1BF *Cald1* knockdown. a** Schematic showing the
2200 siRNA injection site in the S1BF and its spatial relationship with the BLA (orange

2201 dotted line). **b–d** Representative images of caldesmon IF stainningin the S1BF
2202 (**b**) and BLA (**c**) following local S1BF *Cald1* siRNA injection, with quantification
2203 in (**d**). Each dot represents one mouse. Two-way ANOVA followed by Tukey's
2204 multiple comparisons test ($P < 0.0001$). **** indicates $P < 0.0001$. Data are
2205 presented as mean ± SEM.

2206

2207 **Fig.S14 Impact of S1BF *Cald1* knockdown on emotional responses. a, b**
2208 Defecation bouts (**a**), and defecation rate and latency (**b**) in the 40 cm OFT
2209 following S1BF *Cald1* KD in the 40 cm OFT. Each dot represents one mouse.
2210 Mann-Whitney test in (**a**). Sample sizes (*N*) are indicated in the panel (**b**).
2211 Gehan-Breslow-Wilcoxon test in (**b**). **c, d** Representative images (**c**) and
2212 quantification (**d**) of BLA neuronal activation in the 40 cm OFT. Each dot
2213 represents one mouse. Student's *t*-test. **e, f** Unsupported rearing bouts (**e**) and
2214 serum corticosterone concentrations (**f**) in the 40 cm OFT. Each dot represents
2215 one mouse. Mann-Whitney test in (**e**), and student's *t*-test in (**f**). Data are
2216 presented as mean ± SEM.

2217

2218 **Fig.S15 Spectral energy analysis of BLA blood flow signals. a, b**
2219 Representative Fourier plot of BLA CBV signals from 0–1 Hz (**a**) and
2220 quantification of ultra-low-frequency oscillations (0–0.3 Hz) (**b**) in the 40 cm OFT.
2221 Each dot represents one mouse. One-way ANOVA followed by Tukey's multiple

2222 comparisons test ($P < 0.0001$). **** indicates $P < 0.0001$. Data are presented
2223 as mean ± SEM.

2224

2225 **Fig.S16 Supplementary data for BLA optogenetic stimulation. a, b** Running
2226 distance (**a**) and time spent in the center zone (**b**) during optogenetic stimulation
2227 in the 40 cm OFT. Each dot represents one mouse. Student's *t*-test. **c, d**
2228 Representative images (**c**) and quantification (**d**) of Hif-1α immunofluorescence
2229 in the BLA during the optogenetic stimulation in the home cage. Stroke model
2230 tissue serves as a positive control. Each dot represents one mouse. One-way
2231 ANOVA followed by Tukey's multiple comparisons test ($P < 0.0001$). ****
2232 indicates $P < 0.0001$. Data are presented as mean ± SEM.

2233

2234 **Fig.S17 Supplementary locomotion speed and pupil diameter in looming**
2235 **and VR_{eagle} assays. a–d** Quantification of pre-stimulation locomotion speed in
2236 looming (**a**) and VR_{eagle} (**b**) assays, and pupil diameter before (**c**) and at the
2237 conclusion (**d**) of VR_{eagle} stimulation. Each dot represents one mouse. Student's
2238 *t*-test. Data are presented as mean ± SEM.

2239

2240 **Fig.S18 Methodological framework for topological clustering and**
2241 **clustering coordinates of *Grin2d*-cKO mice. a** Schematic workflow for
2242 clustering data processing and generation. **b–g**, Clustering coordinates of

2243 *Grin2d*-cKO mice mapped against the unbiased classification library of
2244 littermate controls across individual contexts. **h** the summary of the load-
2245 dependent biphasic pattern. Quantification data shared with **Fig. 6j**, and
2246 heatmap shared with **Figure. 6l, m**. Each 50% transparent dot represents one
2247 mouse. The non-transparent dot represents the mean value. Student's *t*-test.
2248 Data are presented as mean ± SEM.

2249

2250 **Fig.S19 *Glrb* expression profile in the vascular transcriptome database.**
2251 Transcriptional levels of *Glrb* in venous SMCs (vSMCs), arteriolar SMCs
2252 (aaSMCs), and arterial SMCs (aSMCs). Data are presented as mean ± SEM.

2253

2254 **Fig.S20 Functional and behavioral validation of SMC-specific *Glrb*-cKO**
2255 **mice. a, b** Functional hyperemia in the S1BF (**a**) and quantification of the
2256 plateau phase (**b**). **c** Defecation bouts of mice during the ARS. Each dot
2257 represents one mouse. Shaded areas represent SEM across mice in (**a**).
2258 Student's *t*-test (**b**) and Mann-Whitney test (**c**). Data are presented as mean ±
2259 SEM.

2260

2261 **Fig.S21 Local BLA *Cald1* knockdown occludes the NVC enhancement in**
2262 ***Glrb*-cKO mice. a, b** Representative images (**a**) and quantification (**b**) of BLA
2263 neuronal activation of *Glrb*-cKO mice with local BLA *Cald1* KD in ARS.

Student's *t*-test. **c, d** Defecation bouts (**c**) and serum corticosterone (**d**) in *Glrb*-cKO mice with local BLA *Cald1* KD in ARS. Mann-Whitney test (**c**) and Student's *t*-test (**d**). **e** Baseline cerebral perfusion analysis before and after *Cald1* siRNA cisterna magna injection in the *Glrb*-cKO mice. Paired Student's *t*-test. Each dot represents one mouse. Data are presented as mean ± SEM.

Fig.S22 CRS modelling and *Glrb*-cKO mice naïve behaviours in the 40 cm OFT. a Time spent in the open arms of the elevated plus maze after CRS modelling (EPM, left) and fecal quality (Bristol score, right, data similar to that in **Fig. 8m**) at day-28 of CRS. Student's *t*-test (left) and Mann-Whitney test (right). **b, c** Representative images (**b**) and quantification (**c**) of neuronal activation in the lateral habenula (LHb) after CRS modelling. Student's *t*-test. **d, e** Total running distance (**d**) and time spent in the center zone (**e**) in the 40 cm OFT. Naïve indicates mice without CRS modelling as controls. Each dot represents one mouse. Student's *t*-test. **** indicates $P < 0.0001$. Data are presented as mean ± SEM.

Fig.S23 Assessment of BBB integrity following CRS. Representative images (including non-perfusion positive control) and quantification of IgG fluorescence in the S1BF and BLA after CRS modelling. Each dot represents the average IgG level per mouse, calculated from three ROIs in both the cortex

2285 and the BLA. One-way ANOVA followed by Tukey's multiple comparisons test

2286 ($P < 0.0001$). **** indicates $P < 0.0001$. Data are presented as mean ± SEM.

2287

2288 **Fig.S24 Statistical quantification of the percentage of c-Fos positive**

2289 **neurons in the BLA. (a–u)** Re-quantification of c-Fos positive neuron ratios

2290 (normalized to total NeuN positive neurons in the BLA) corresponding to the

2291 original intensity-based data presented in Figure 1c (**a**), Figure 1e (**b**), Figure

2292 1o (**c**), Figure 2m (**d**), Figure 3g (**e**), Figure 3m (**f**), Figure S11g (**g**), Figure S11l

2293 (**h**), Figure S11p (**i**), Figure S11y (**j**), Figure S12k (**k**), Figure 4m (**l**), Figure S14d

2294 (**m**), Figure 5i (**n**), Figure 5r left (**o**), Figure 6j (**p**), Figure 8b (**q**), Figure 8h (**r**),

2295 Figure 8p left (**s**), Figure S21b (**t**), and Figure S22c (**u**), respectively.

2296

2297 *Supplementary tables*

2298 **Supplementary Table S1. P_{value} of Defecation rate-latency curve**

2299 Sub table 1 for **Fig. 3c**

P	1	2	3	4	5	6
1	1	0.0031	0.0019	****	****	****
2		1	0.1934	0.3581	0.1384	0.1189
3			1	0.8685	0.3193	0.3458
4				1	0.1585	0.1083

5					1	0.9278
6						1

1. OFT_40 *Grin2d*$^{f/f}$
2. OFT_35 *Grin2d*$^{f/f}$
3. OFT_10 *Grin2d*$^{f/f}$
4. OFT_40 *Grin2d*-cKO
5. OFT_40 *Grin2d*-cKO
6. OFT_40 *Grin2d*-cKO

**** indicates $P < 0.0001$

Sub table 2 for **Fig. 3i**

P	1	2	3	4
1	1	0.1650	****	0.6470
2		1	****	0.2934
3			1	****
4				1

1. *Grin2d*$^{f/f}$+Saline
2. *Grin2d*$^{f/f}$+HET0016
3. *Grin2d*-cKO+Saline
4. *Grin2d*-cKO+HET0016

**** indicates $P < 0.0001$

2314

2315 Sub table 3 for **Fig. 3o**

P	1	2	3	4
1	1	0.0679	0.0003	0.2123
2		1	****	0.3173
3			1	****
4				1

2316 5. *Grin2d*$^{f/f}$+Saline

2317 6. *Grin2d*$^{f/f}$+HET0016

2318 7. *Grin2d*-cKO+Saline

2319 8. *Grin2d*-cKO+HET0016

2320 **** indicates $P < 0.0001$

2321

2322 Sub table 4 for **Fig. 4q**

P	1	2	3	4	5
1	1	****	****	0.0009	****
2		1	0.5745	0.8881	0.9999
3			1	0.99990	0.6926
4				1	0.6353
5					1

2323 1. Scramble (Whole-brain+BLA)

2. *Cald1* KD (Whole-brain)
3. *Cald1* KD (BLA)
4. Scramble (BLA)+*Grin2d*-cKO
5. *Cald1* KD (BLA)+*Grin2d*-cKO

**** indicates $P < 0.0001$

Sub table 5 for **Fig. 8f**

P	1	2	3	4
1	1	0.0012	0.6285	0.4703
2		1	0.0035	0.0244
3			1	0.2637
4				1

1. Floxed control mice
2. *Pdgfrβ-creER:Grin2d*$^{f/f}$
3. *Pdgfrβ-creER:Glrb*$^{f/f}$
4. *Pdgfrβ-creER:Grin2d*$^{f/f}$*:Glrb*$^{f/f}$

**** indicates $P < 0.0001$

2339 Sub table 6 for **Fig. S12p**

P	1	2	3	4	5	6	7	8	9	10	11	12
1	1	****	0.0002	0.0823	0.0005	0.8480	****	****	0.4906	****	0.5680	****
2		1	0.7333	0.0092	0.7209	0.0002	0.0786	0.2073	0.0043	0.4279	0.0010	0.2679
3			1	0.0047	0.7747	0.0001	0.2580	0.3542	0.0028	0.7549	0.0010	0.4218
4				1	0.0130	0.1038	****	0.0001	0.2961	0.0009	0.0548	0.0005
5					1	0.0004	0.2596	0.3170	0.0078	0.9480	0.0022	0.5377
6						1	****	****	0.5970	****	0.4793	****
7							1	0.4699	****	0.2935	0.0003	0.8118
8								1				
9								****	1	0.0008	0.2695	0.0005
10								0.3463		1	0.0003	0.5583
11								****			1	0.0005
12								0.9373				1

2340 1. *Grin2d*$^{f/f}$

2341 2. *SMA-creER:Grin2d*$^{f/f}$

2342 3. *Pdgfrβ-creER:Grin2d*$^{f/f}$

2343 4. *Grin1*$^{f/f}$

2344 5. *SMA-creER:Grin1*$^{f/f}$

2345 6. *Ptgs2*$^{f/f}$

2346 7. *Emx1-cre:Ptgs2*$^{f/f}$

2347 8. *SMA-creER:Grin1*$^{f/f}$*:Grin2d*$^{f/f}$

2348 9. *Acta2*$^{f/f}$

2349 10. *Pdgfrβ-creER:Acta2*$^{f/f}$

2350 11. NFD

2351 12. HFD

2352 **** indicates $P < 0.0001$

2353

2354 **Supplementary Table S2. Sample source checklist**

No.	Location	Sample type	Source
1	Fig. 1b	Immunofluorescence staining	Brain slice
2	Fig. 1n	Immunofluorescence staining	Brain slice
3	Fig. 2b	Semi-quantified PCR	Sorted cultured cell
4	Fig. 2c	RNAscope	Brain slice
5	Fig. 2d	Immunofluorescence staining	Isolated MCA
6	Fig. 2l	Immunofluorescence staining	Brain slice
7	Fig. S1a	RNAscope	Brain slice
8	Fig. S1c	Western blot	Cerebellum lysates
9	Fig. S1d	Western blot	Sorted cultured cell
10	Fig. S1e	Western blot	Cortex lysates
11	Fig. S2a	Immunofluorescence staining	Tissue slice
12	Fig. S3i	Hematoxylin and eosin staining	Intestine slice
13	Fig. S3o	Absorbance measurement	Brain lysates

14	Fig. S4a	Western blot	Sorted culture cell
15	Fig. S4b	Immunofluorescence staining	Isolated MCA
16	Fig. 3f	Immunofluorescence staining	Brain slice
17	Fig. 3l	Immunofluorescence staining	Brain slice
18	Fig. S11b	Immunofluorescence staining	Brain slice
19	Fig. S11f	Immunofluorescence staining	Brain slice
20	Fig. S11k	Immunofluorescence staining	Brain slice
21	Fig. S11o	Immunofluorescence staining	Brain slice
22	Fig. S11t	Western blot	Cortex lysates
23	Fig. S11x	Immunofluorescence staining	Brain slice
24	Fig. S12e	Absorbance measurement	Brain lysates
25	Fig. S12j	Immunofluorescence staining	Brain slice
26	Fig. 4b	Western blot	Sorted culture cell
27	Fig. 4d	Immunofluorescence staining	Brain slice
28	Fig. 4f	Semi-quantified PCR	Cortex lysate
29	Fig. 4g	Immunofluorescence staining	Brain slice
30	Fig. 4h	Immunofluorescence staining	Brain slice
31	Fig. 4l	Immunofluorescence staining	Brain slice
32	Fig. S13b	Immunofluorescence staining	Brain slice
33	Fig. S13c	Immunofluorescence staining	Brain slice
34	Fig. S14c	Immunofluorescence staining	Brain slice
35	Fig. 5a	Immunofluorescence staining	Brain slice

36	Fig. 5h	Immunofluorescence staining	Brain slice
37	Fig. 5q	Immunofluorescence staining	Brain slice
38	Fig. S16c	Immunofluorescence staining	Brain slice
39	Fig. 7a	RNAscope	Brain slice
40	Fig. 7c	Immunofluorescence staining	Brain slice
41	Fig. 7f	Semi-quantified PCR	Acute sorted cell
42	Fig. 7g	Immunofluorescence staining	Cultured cell line
43	Fig. 7h	Immunofluorescence staining	Brain slice
44	Fig. 7i	Electron microscopy image	Brain slice
45	Fig. 8a	Immunofluorescence staining	Brain slice
46	Fig. 8g	Immunofluorescence staining	Brain slice
47	Fig. 8o	Immunofluorescence staining	Brain slice
48	Fig. S21a	Immunofluorescence staining	Brain slice
49	Fig. S22b	Immunofluorescence staining	Brain slice
50	Fig. S23	Immunofluorescence staining	Brain slice

Supplementary Table S3. Mice information

Abbreviation	Full name	Source
Ai32	*B6;129S-Gt(ROSA)26Sortm32(CAG-COP4*H134R/EYFP)Hze/J*	*Hailan Hu, Zhejiang University*

Nestin-cre	*B6.Cg-Tg(Nes-cre)1Kln/J*	*Yanmei Tao and Xu Hu, Hangzhou Normal University/ Southeast University*
Emx1-cre	*B6.129S2-Emx1tm1(cre)Krj/J*	*Yanmei Tao and Xu Hu, Hangzhou Normal University/ Southeast University*
SMA-creER	*Tg(Acta2-cre/ERT2)12Pcn*	*Bo Zhou, ShanghaiInstitutes for Biological Sciences, Chinese Academy of Sciences*
Pdgfrβ-creER	*Tg(Pdgfrb-cre/ERT2)6096Rha*	*Xiang Yu, Peking University*
Ai47	*Gt(ROSA)26Sortm47(CAG-EGFP*)Hze*	*Zilong Qiu, Chinese Academy of Sciences Center for Excellence in Brain Science and Intelligence Technology, Chinese Academy of Sciences.*

Ai14	*B6.Cg-Gt(ROSA)26Sortm14(CAG-tdTomato)Hze/J*	*Woo-Ping Ge, Chinese Institute of Brain Research (CIBR)*
Grin2d	*B6/JGpt-Grin2dem1Cflox/Gpt*	*GemPharmatech*
Grin1	*Grin1tm2Stl*	*Yangang Sun, Chinese Academy of Sciences Center for Excellence in Brain Science and Intelligence Technology, Chinese Academy of Sciences*
Ptgs2	*C57BL/6JCya-Ptgs2em1flox/Cya*	*Cyagen*
Acta2	*C57BL/6JGpt-Acta2em1Cflox/Gpt*	*GemPharmatech*
Glrb	*C57BL/6JGpt-Glrbem1Cflox/Gpt*	*GemPharmatech*

2360 **Supplementary Table S4. Antibodies information**

Name	Host	Cat#	Dilution	Company
Anti-NMDAR2D Antibody	Mouse	MAB5578	1:400 (IF) 1:2,500 (WB) 1:1,000 (IP)	Merck
Anti-Smoothelin antibody	Rabbit	ab219652	1:400 (IF)	abcam
α-Smooth Muscle Actin (ACTA2) Rabbit mAb	Rabbit	A17910	1:2,500 (WB)	ABclonal
ACE2 Recombinant Rabbit Monoclonal Antibody (SN0754)	Rabbit	MA5-32307	1:400 (IF)	Invitrogen
Gephyrin Polyclonal Antibody	Rabbit	PA5-29036	1:400 (IF)	Invitrogen
BD Pharmingen™ Purified Rat Anti-Mouse CD31	Rat	557355	1:200 (IF)	BD
Anti-NeuN purified Antibody	Guinea Pig	ABN90P	1:800 (IF)	Merck
COX2/PTGS2 Rabbit pAb	Rabbit	A1253	1:400 (IF)	ABclonal
c-Fos antibody	Rabbit	226 003	1:1,000 (IF)	SYSY

Recombinant Alexa Fluor® 488 Anti-Caldesmon/CDM antibody	Rabbit	ab208116	1:400 (IF) 1:2,500 (WB)	abcam
iFluor™ 488 Conjugated Goat anti-mouse IgG polyclonal Antibody	Goat	HA1125	1:400 (IF)	HUABIO
Mouse Aminopeptidase N/CD13 Antibody	Goat	AF2335	1:200 (IF)	R&D
CD140b (PDGFRB) Monoclonal Antibody (APB5), APC, eBioscience™	Rat	17-1402-82	1:50 (FCM)	Invitrogen
Mice IgG	Mouse	A7028	1:1,000 (IP)	Beyotime
Donkey anti-Mouse IgG (H+L) ReadyProbes™ Secondary Antibody, Alexa Fluor™ 488	Donkey	R37114	1:1,000 (IF)	Invitrogen
Donkey anti-Rabbit IgG (H+L) ReadyProbes™ Secondary Antibody, Alexa Fluor™ 488	Donkey	R37118	1:1,000 (IF)	Invitrogen
Donkey anti-Rabbit IgG (H+L) Highly Cross-Adsorbed Secondary Antibody, Alexa Fluor™ 546	Donkey	A10040	1:1,000 (IF)	Invitrogen

Donkey anti-Rat IgG (H+L) Highly Cross-Adsorbed Secondary Antibody, Alexa Fluor™ 488	Donkey	A21208	1:1,000 (IF)	Invitrogen
Donkey anti-Rat IgG (H+L) Highly Cross-Adsorbed Secondary Antibody, Alexa Fluor™ 555	Donkey	A78945	1:1,000 (IF)	Invitrogen
Donkey anti-Rat IgG (H+L) Highly Cross-Adsorbed Secondary Antibody, Alexa Fluor™ Plus 647	Donkey	A48272	1:1,000 (IF)	Invitrogen
Alexa Fluor® 647 AffiniPure™ Donkey Anti-Guinea Pig IgG (H+L)	Donkey	706-605-148	1:1,000 (IF)	Jackson ImmunoResearch
β-Tubulin Mouse mAb	Mouse	AC021	1:5,000 (WB)	ABclonal
Goat Anti-Mouse IgG, HRP Conjugated	Goat	CW0102	1:10,000 (WB)	CWBIO
Goat Anti-Rabbit IgG, HRP Conjugated	Goat	CW0103	1:10,000 (WB)	CWBIO
DDDDK-Tag Rabbit mAb	Rabbit	AE063	1:400 (IF)	ABclonal

Hif-1α	Rabbit	ER1802-41	1:100 (IF)	HUABIO

2361

2362 **Supplementary Table S5. Primer pairs information**

Name		Sequence
Grin1	F	AAGAACCTGCAGCAGTACCA
	R	GCAGCAGGACTCATCAGTGT
Grin2a	F	TCAGGGACTTTGGAAAACGCT
	R	AAGTCATGCAGGGTTGGTTG
Grin2b	F	ACTAACTATCAATGAAGAACGGT
	R	CCAGACCCCAGAGTAACCA
Grin2c	F	TGTGGGCCTTCTTCGCTGTCATCT
	R	TGCCATTAGGTACCGTGCCAAAAC
Grin2d	F	TGGAGGAGTACGACTGGACAT
	R	CGCACTGACACTACGGAGC
Grin3a	F	CTGCACACCAGTCAGAGGTT
	R	TTCGTTGGTTGTCGTGACTC

Grin3b	F	TGGGGGTCTACCACTTGTCA
	R	TGGATCTTCTGGCTCGTGTG
Glrb	F	TTCAAAGGCATTCCTGTTGATGT
	R	TGAGCCTCTGAAGTCACTAGG
Cald1	F	GCCGTTCAAGTGCTTCACTC
	R	TGTCAATCTTGGAGACTACTGCT
18s	F	CGGACACGGACAGGATTGACA
	R	CCAGACAAATCGCTCCACCAACTA
Cald1 *(siRNA)*	F	GUUUGAUCCGACCAUAACAGA
	R	UGUUAUGGUCGGAUCAAACUC

Supplementary Video

Supplementary Video S1. Topological distribution of arterioles in the BLA.

Supplementary Video S2. Pupil diameter changes during the stimulation in the VR_{eagle} stimulation assay.

a

b

c

d

e

f

g

h

i

j

k

l

m

n

o

p

q

r

s

t

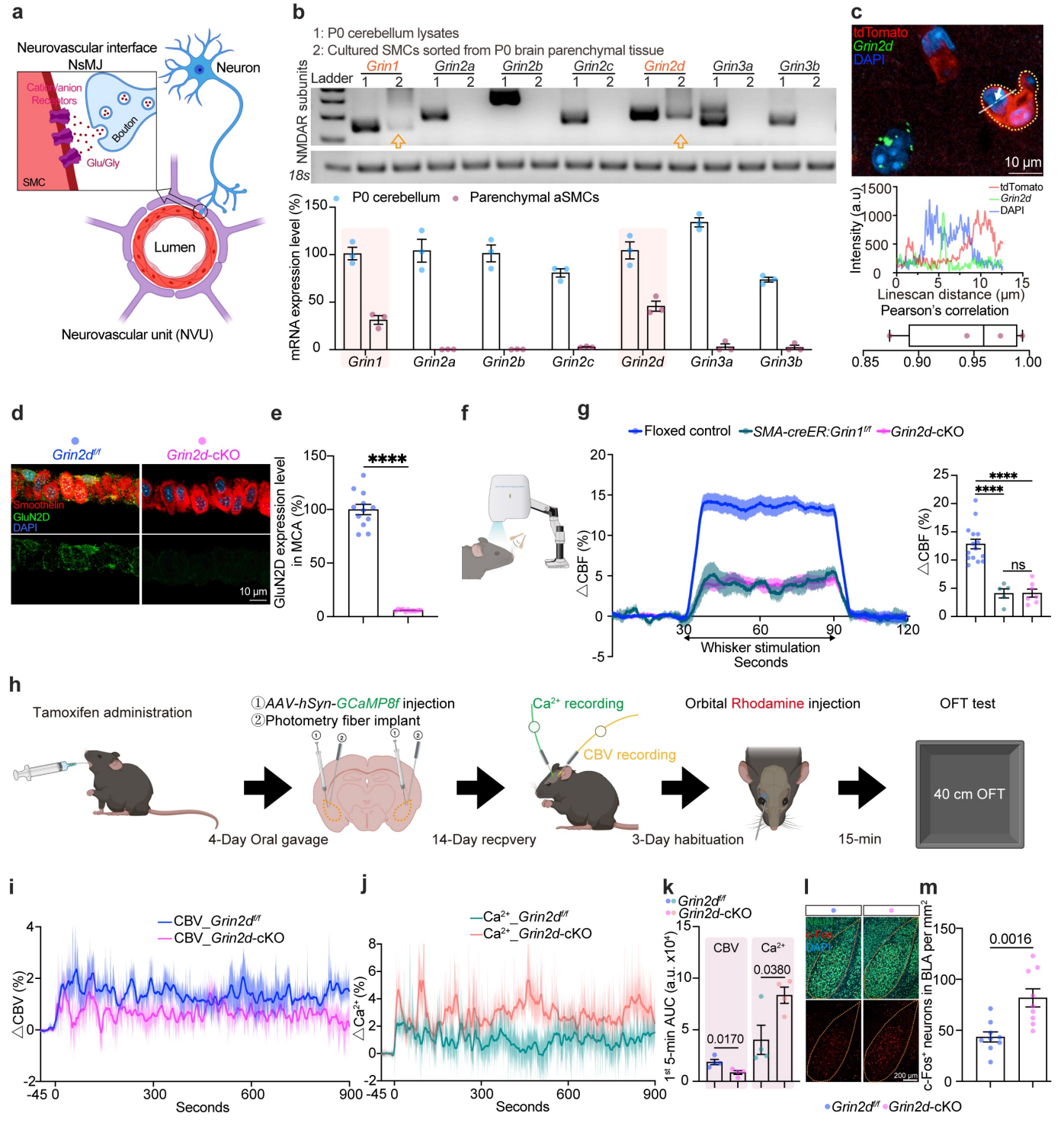
a
Neurovascular interface
NsMJ
Neuron
Cation/anion Receptors
Bouton
Glu/Gly
SMC
Lumen
Neurovascular unit (NVU)
b
1: P0 cerebellum lysates
2: Cultured SMCs sorted from P0 brain parenchymal tissue
Ladder
Grin1
Grin2a
Grin2b
Grin2c
Grin2d
Grin3a
Grin3b
NMDAR subunits
18s
P0 cerebellum
Parenchymal aSMCs
mRNA expression level (%)
c
tdTomato
Grin2d
DAPI
10 μm
Intensity (a.u.)
Linescan distance (μm)
Pearson's correlation
d
Grin2d f/f
Grin2d-cKO
Smoothelin
GluN2D
DAPI
10 μm
e
GluN2D expression level in MCA (%)
****
f
g
Floxed control
SMA-creER:Grin1 f/f
Grin2d-cKO
△CBF (%)
Whisker stimulation
Seconds
****
****
ns
h
Tamoxifen administration
4-Day Oral gavage
①AAV-hSyn-GCaMP8f injection
②Photometry fiber implant
14-Day recpvery
Ca2+ recording
CBV recording
Orbital Rhodamine injection
3-Day habituation
OFT test
15-min
40 cm OFT
i
CBV_Grin2d f/f
CBV_Grin2d-cKO
△CBV (%)
Seconds
j
Ca2+_Grin2d f/f
Ca2+_Grin2d-cKO
△Ca2+ (%)
Seconds
k
Grin2d f/f
Grin2d-cKO
CBV
Ca2+
0.0170
0.0380
1st 5-min AUC (a.u. x10⁴)
l
c-Fos
DAPI
200 μm
m
0.0016
c-Fos+ neurons in BLA per mm2
Grin2d f/f
Grin2d-cKO

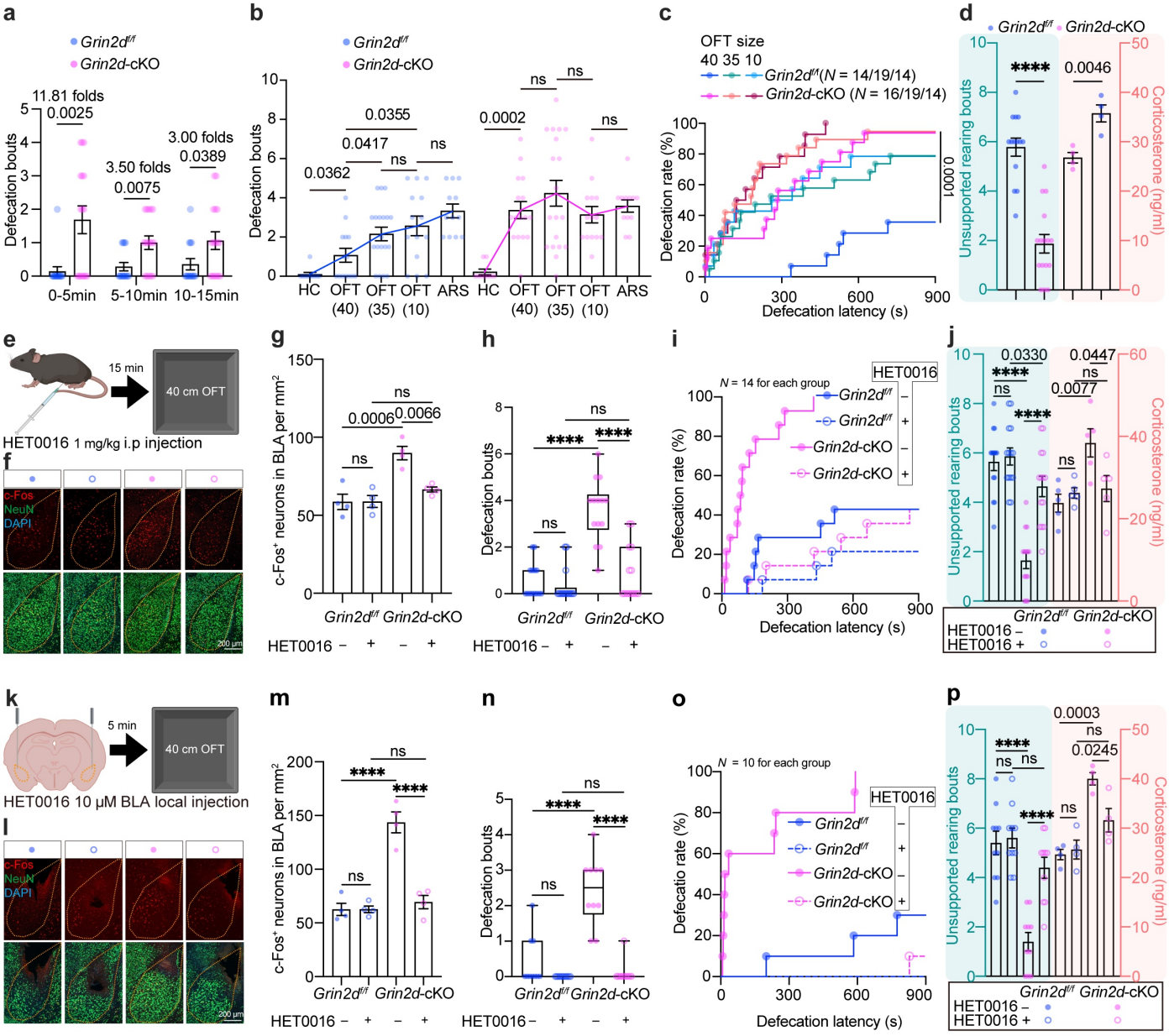
a
Grin2d f/f
Grin2d-cKO
11.81 folds
0.0025
3.50 folds
0.0075
3.00 folds
0.0389
Defecation bouts
0-5min
5-10min
10-15min
b
Grin2d f/f
Grin2d-cKO
0.0362
0.0417
0.0355
ns
0.0002
Defecation bouts
HC
OFT (40)
OFT (35)
OFT (10)
ARS
c
OFT size
40 35 10
Grin2d f/f (N = 14/19/14)
Grin2d-cKO (N = 16/19/14)
0.0001
Defecation rate (%)
Defecation latency (s)
d
Grin2d f/f
Grin2d-cKO
****
0.0046
Unsupported rearing bouts
Corticosterone (ng/ml)
e
15 min
40 cm OFT
HET0016 1 mg/kg i.p injection
f
c-Fos
NeuN
DAPI
200 μm
g
0.0006
0.0066
c-Fos+ neurons in BLA per mm2
Grin2d f/f
Grin2d-cKO
HET0016
h
Defecation bouts
i
N = 14 for each group
HET0016
Grin2d f/f
Grin2d-cKO
Defecation rate (%)
Defecation latency (s)
j
0.0330
0.0447
0.0077
Unsupported rearing bouts
Corticosterone (ng/ml)
HET0016 –
HET0016 +
k
5 min
40 cm OFT
HET0016 10 μM BLA local injection
l
c-Fos
NeuN
DAPI
200 μm
m
c-Fos+ neurons in BLA per mm2
n
Defecation bouts
o
N = 10 for each group
HET0016
Defecation rate (%)
Defecation latency (s)
p
0.0003
0.0245
Unsupported rearing bouts
Corticosterone (ng/ml)

Revised Figure 4

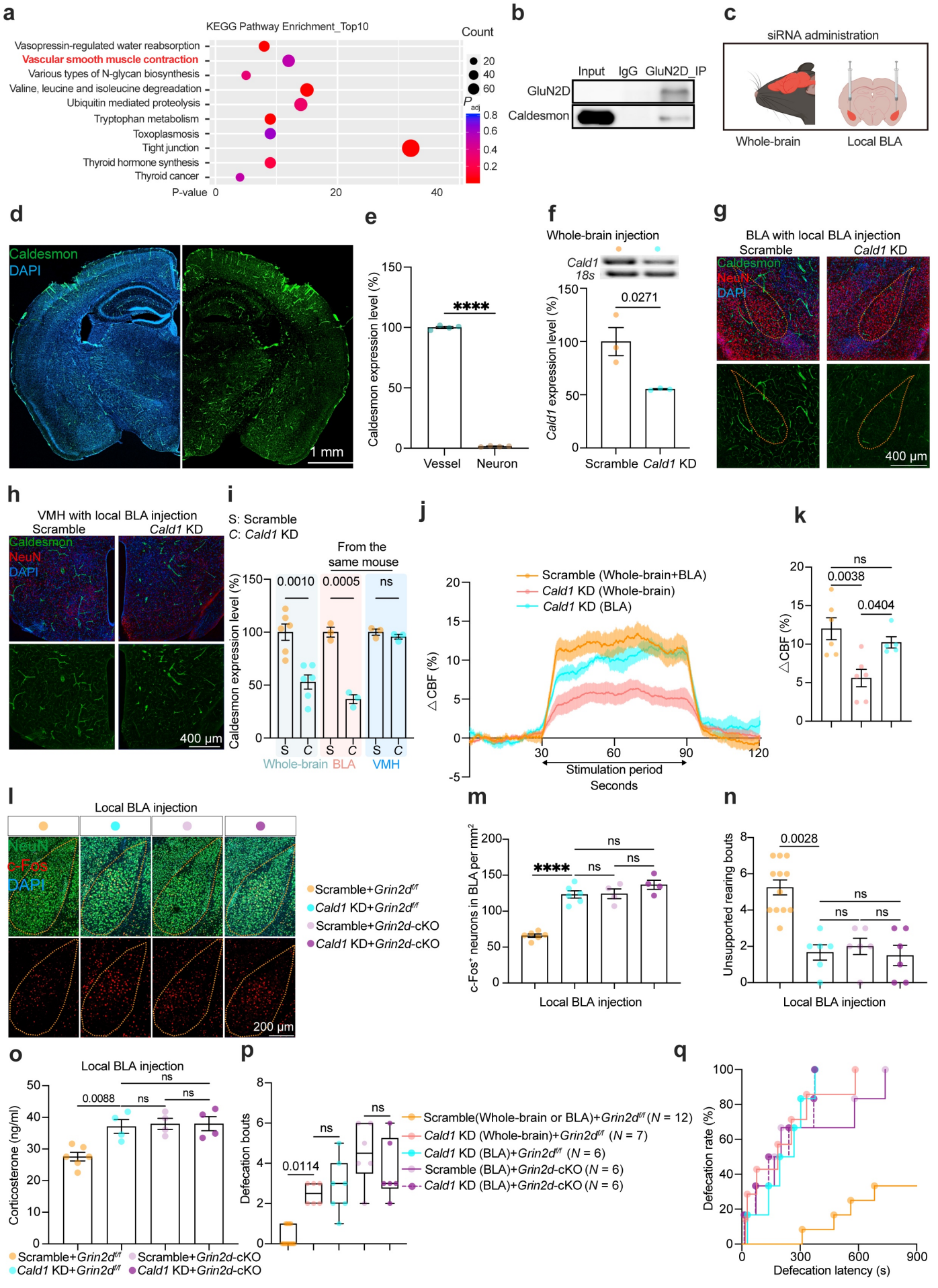

Revised Figure 5

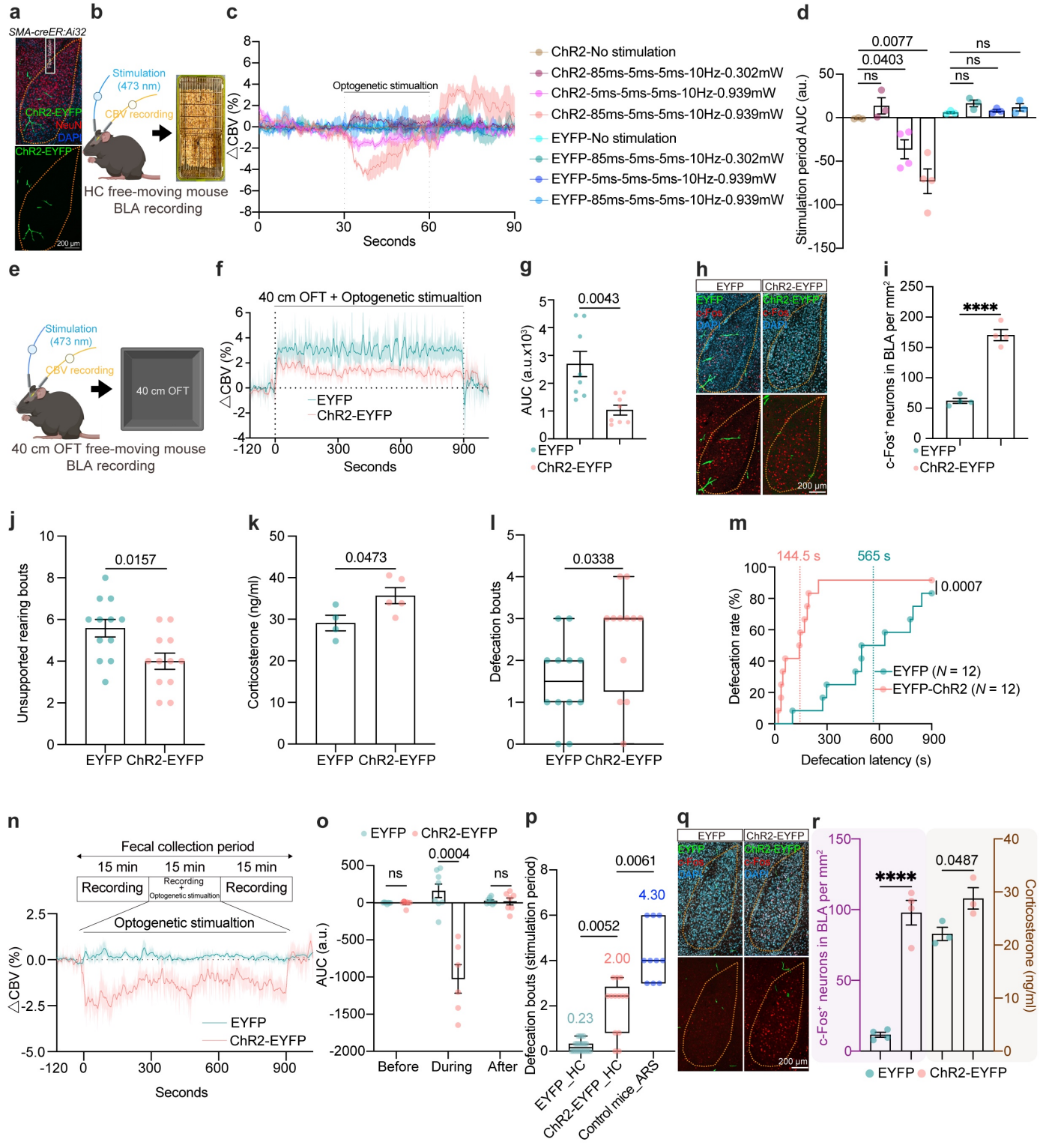

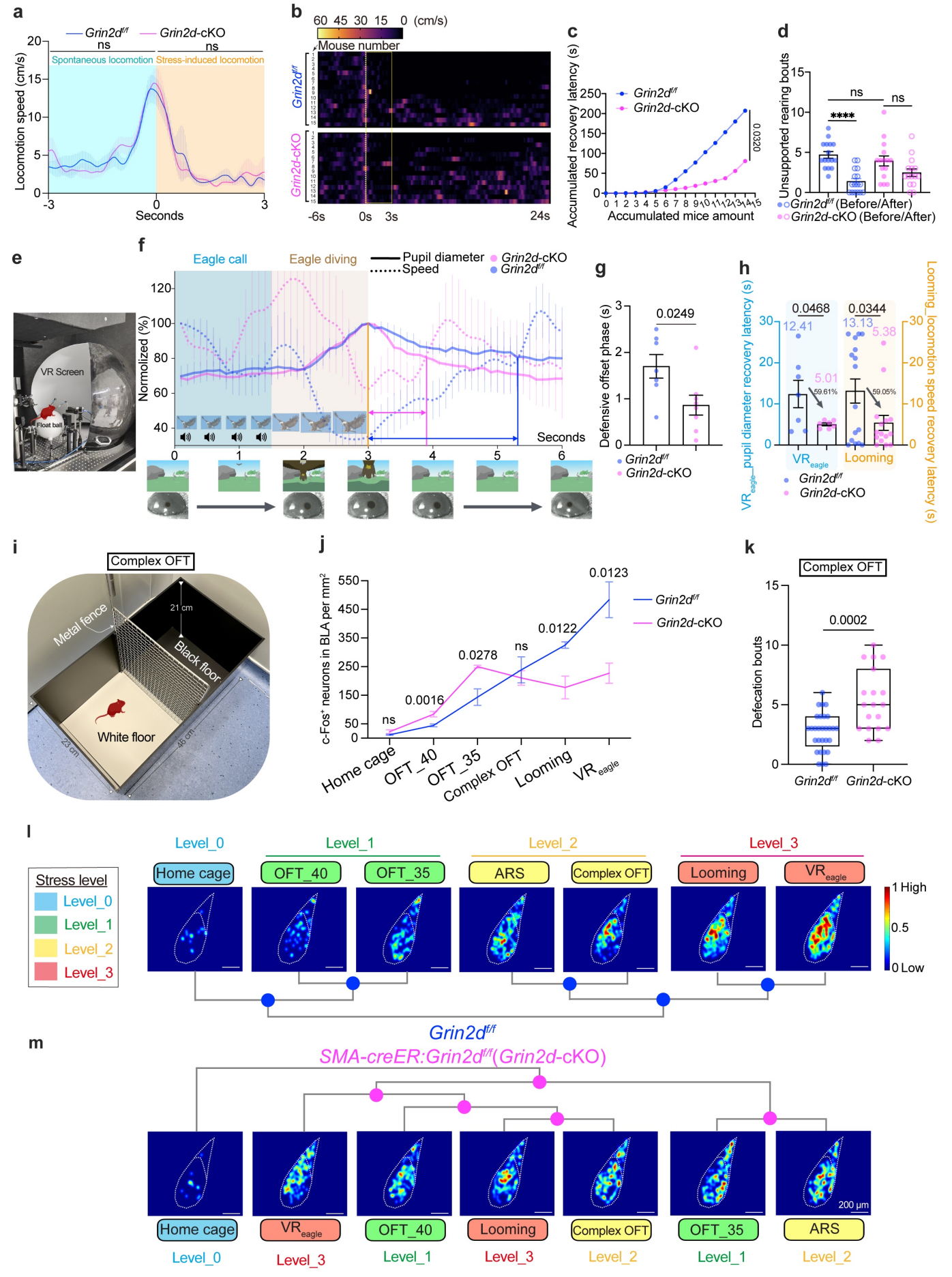
a
Grin2df/f
Grin2d-cKO
ns
ns
Spontaneous locomotion
Stress-induced locomotion
Locomotion speed (cm/s)
Seconds
b
60 45 30 15 0 (cm/s)
Mouse number
Grin2df/f
Grin2d-cKO
-6s 0s 3s 24s
c
Accumulated recovery latency (s)
Grin2df/f
Grin2d-cKO
0.0320
Accumulated mice amount
d
Unsupported rearing bouts
ns
ns
****
Grin2df/f (Before/After)
Grin2d-cKO (Before/After)
e
VR Screen
Float ball
f
Eagle call
Eagle diving
Pupil diameter
Speed
Grin2d-cKO
Grin2df/f
Normolized (%)
Seconds
g
Defensive offset phase (s)
0.0249
Grin2df/f
Grin2d-cKO
h
VReagle_pupil diameter recovery latency (s)
Looming_locomotion speed recovery latency (s)
0.0468
0.0344
12.41
5.01
59.61%
13.13
5.38
59.05%
VReagle
Looming
Grin2df/f
Grin2d-cKO
i
Complex OFT
Metal fence
21 cm
Black floor
White floor
23 cm
46 cm
j
c-Fos+ neurons in BLA per mm2
Grin2df/f
Grin2d-cKO
ns
0.0016
0.0278
ns
0.0122
0.0123
Home cage
OFT_40
OFT_35
Complex OFT
Looming
VReagle
k
Complex OFT
Defecation bouts
0.0002
Grin2df/f
Grin2d-cKO
l
Level_0
Level_1
Level_2
Level_3
Stress level
Level_0
Level_1
Level_2
Level_3
Home cage
OFT_40
OFT_35
ARS
Complex OFT
Looming
VReagle
1 High
0.5
0 Low
m
Grin2df/f
SMA-creER:Grin2df/f(Grin2d-cKO)
200 μm
Home cage
VReagle
OFT_40
Looming
Complex OFT
OFT_35
ARS
Level_0
Level_3
Level_1
Level_3
Level_2
Level_1
Level_2

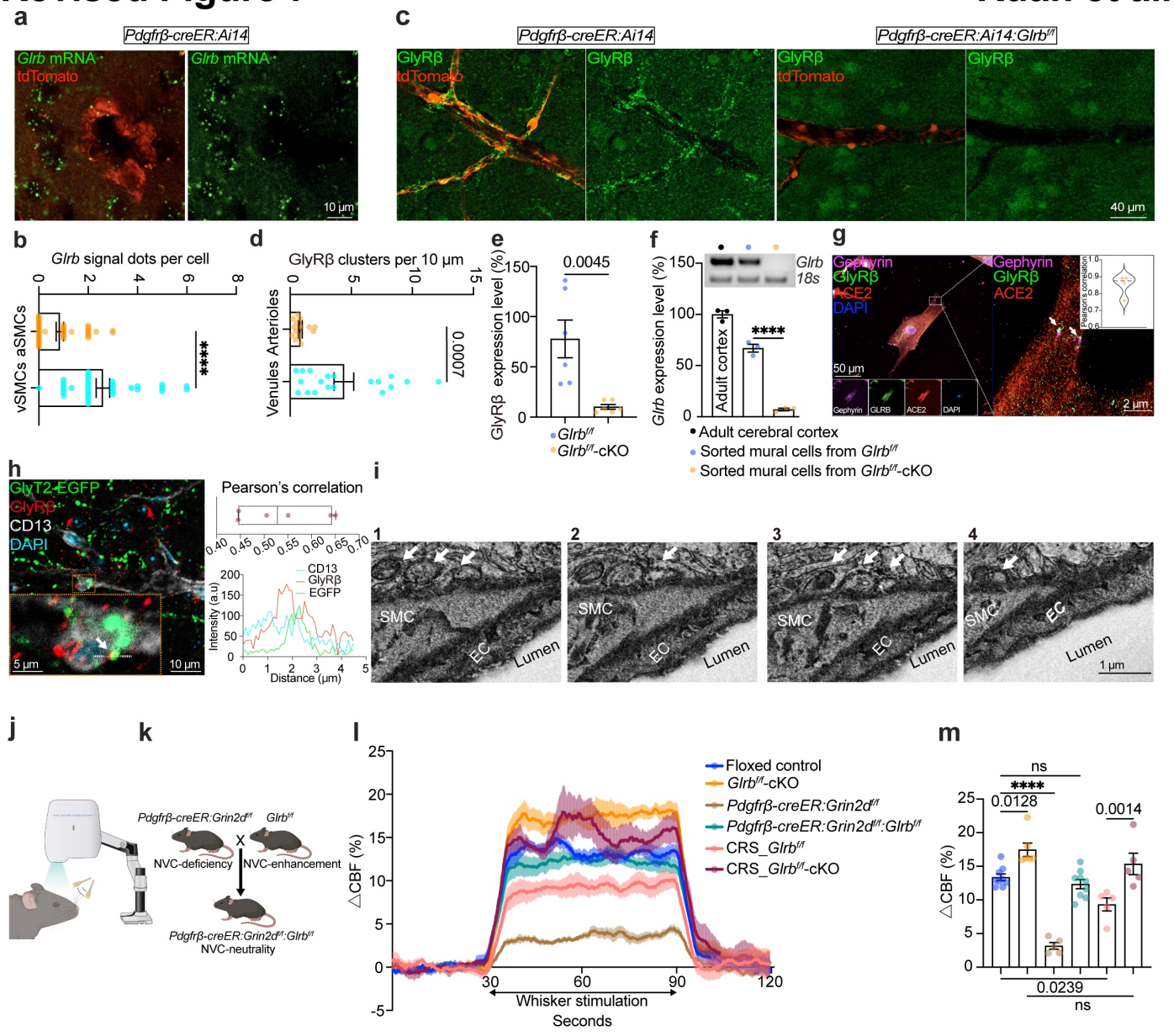
a
Pdgfrβ-creER:Ai14
Glrb mRNA
tdTomato
Glrb mRNA
10 μm
c
Pdgfrβ-creER:Ai14
Pdgfrβ-creER:Ai14:Glrb f/f
GlyRβ
tdTomato
GlyRβ
GlyRβ
tdTomato
GlyRβ
40 μm
b
Glrb signal dots per cell
vSMCs aSMCs
****
d
GlyRβ clusters per 10 μm
Venules Arterioles
0.0007
e
GlyRβ expression level (%)
0.0045
Glrb f/f
Glrb f/f-cKO
f
Glrb 18s
Glrb expression level (%)
Adult cortex
****
Adult cerebral cortex
Sorted mural cells from Glrb f/f
Sorted mural cells from Glrb f/f-cKO
g
Gephyrin
GlyRβ
ACE2
DAPI
Gephyrin
GlyRβ
ACE2
Pearson's Correlation
50 μm
2 μm
Gephyrin
GLRB
ACE2
DAPI
h
GlyT2-EGFP
GlyRβ
CD13
DAPI
5 μm
10 μm
Pearson's correlation
CD13
GlyRβ
EGFP
Intensity (a.u)
Distance (μm)
i
1
2
3
4
SMC
EC
Lumen
1 μm
j
k
Pdgfrβ-creER:Grin2d f/f
Glrb f/f
NVC-deficiency
NVC-enhancement
Pdgfrβ-creER:Grin2d f/f:Glrb f/f
NVC-neutrality
l
Floxed control
Glrb f/f-cKO
Pdgfrβ-creER:Grin2d f/f
Pdgfrβ-creER:Grin2d f/f:Glrb f/f
CRS_Glrb f/f
CRS_Glrb f/f-cKO
△CBF (%)
Whisker stimulation
Seconds
m
ns
****
0.0128
0.0014
△CBF (%)
0.0239
ns

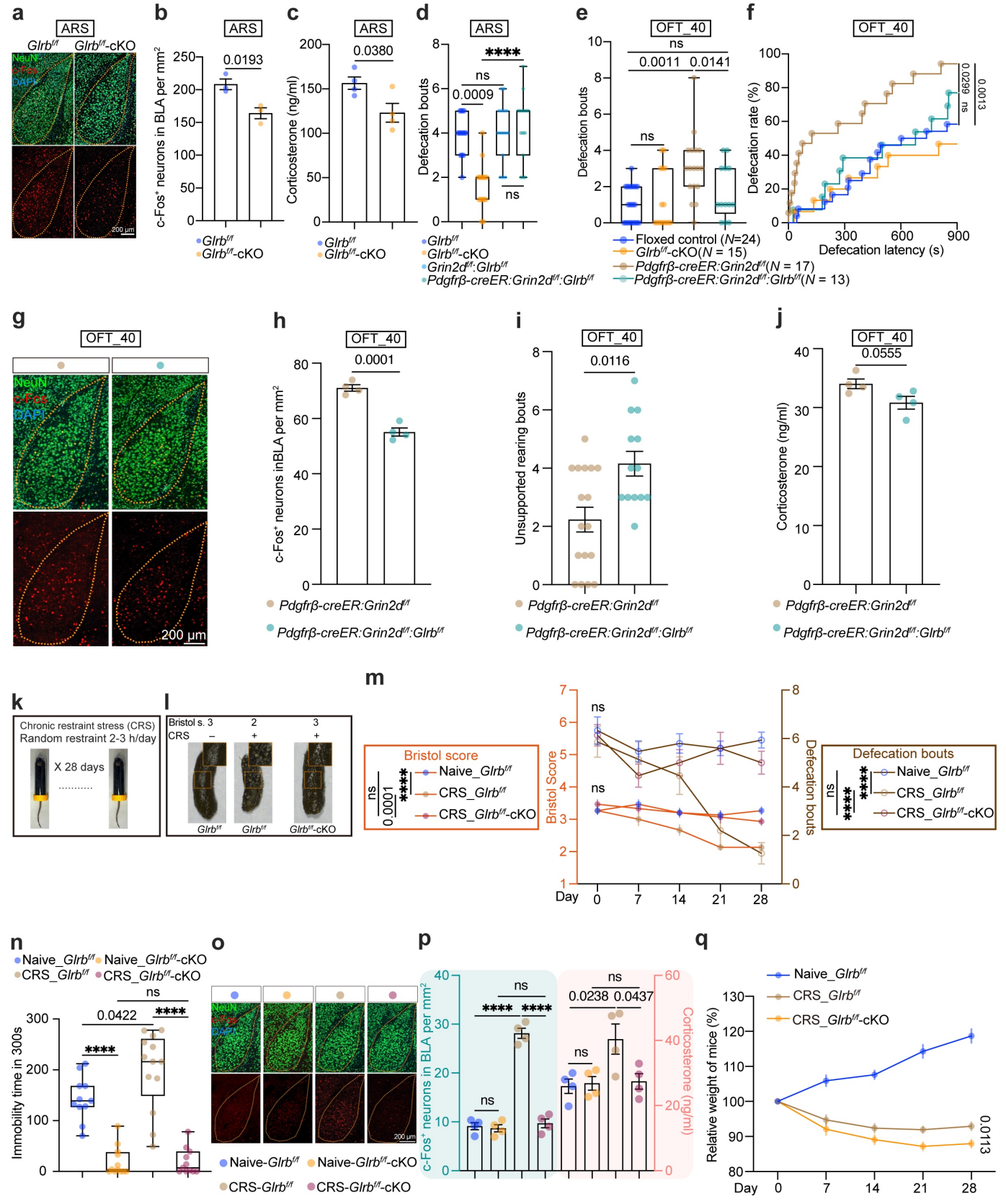
a
ARS
Glrb f/f
Glrb f/f-cKO
NeuN
c-Fos
DAPI
200 μm
b
ARS
c-Fos+ neurons in BLA per mm2
0.0193
Glrb f/f
Glrb f/f-cKO
c
ARS
Corticosterone (ng/ml)
0.0380
Glrb f/f
Glrb f/f-cKO
d
ARS
Defecation bouts
****
ns
0.0009
ns
Glrb f/f
Glrb f/f-cKO
Grin2d f/f:Glrb f/f
Pdgfrβ-creER:Grin2d f/f:Glrb f/f
e
OFT_40
Defecation bouts
ns
0.0011
0.0141
ns
f
OFT_40
Defecation rate (%)
0.0299
ns
0.0013
Defecation latency (s)
Floxed control (N=24)
Glrb f/f-cKO(N = 15)
Pdgfrβ-creER:Grin2d f/f(N = 17)
Pdgfrβ-creER:Grin2d f/f:Glrb f/f(N = 13)
g
OFT_40
NeuN
c-Fos
DAPI
200 μm
h
OFT_40
c-Fos+ neurons inBLA per mm2
0.0001
Pdgfrβ-creER:Grin2d f/f
Pdgfrβ-creER:Grin2d f/f:Glrb f/f
i
OFT_40
Unsupported rearing bouts
0.0116
Pdgfrβ-creER:Grin2d f/f
Pdgfrβ-creER:Grin2d f/f:Glrb f/f
j
OFT_40
Corticosterone (ng/ml)
0.0555
Pdgfrβ-creER:Grin2d f/f
Pdgfrβ-creER:Grin2d f/f:Glrb f/f
k
Chronic restraint stress (CRS)
Random restraint 2-3 h/day
X 28 days
l
Bristol s. 3
2
3
CRS
–
+
+
Glrb f/f
Glrb f/f
Glrb f/f-cKO
m
Bristol score
ns
0.0001
****
Naive_Glrb f/f
CRS_Glrb f/f
CRS_Glrb f/f-cKO
Bristol Score
Defecation bouts
ns
ns
Day
0
7
14
21
28
Defecation bouts
ns
****
****
Naive_Glrb f/f
CRS_Glrb f/f
CRS_Glrb f/f-cKO
n
Naive_Glrb f/f
Naive_Glrb f/f-cKO
CRS_Glrb f/f
CRS_Glrb f/f-cKO
Immobility time in 300s
ns
0.0422
****
****
o
NeuN
c-Fos
DAPI
200 μm
Naive-Glrb f/f
Naive-Glrb f/f-cKO
CRS-Glrb f/f
CRS-Glrb f/f-cKO
p
c-Fos+ neurons in BLA per mm2
ns
****
****
ns
Corticosterone (ng/ml)
ns
0.0238
0.0437
ns
q
Naive_Glrb f/f
CRS_Glrb f/f
CRS_Glrb f/f-cKO
Relative weight of mice (%)
0.0113
Day
0
7
14
21
28

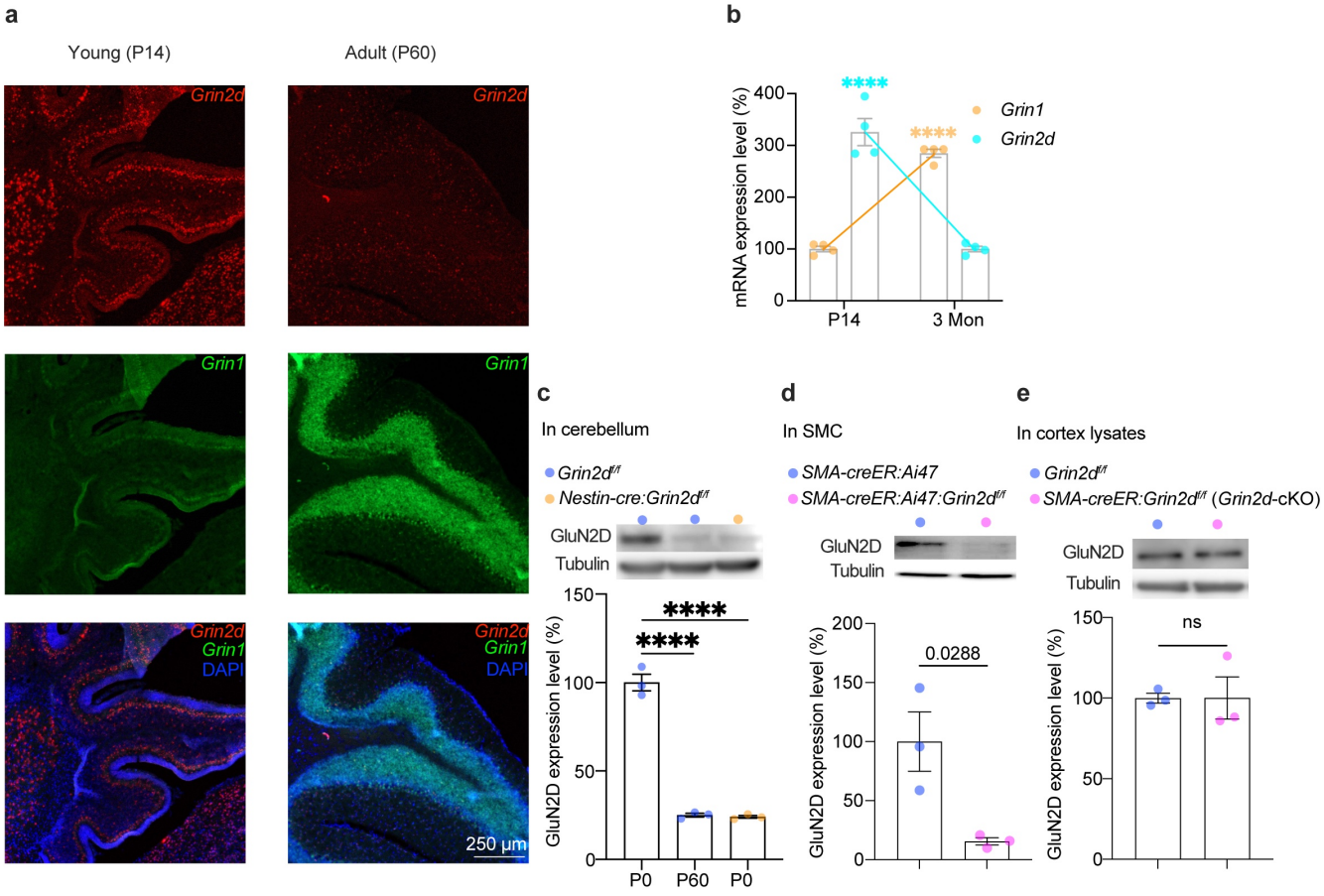
a
Young (P14)
Adult (P60)
Grin2d
Grin1
DAPI
250 μm
b
mRNA expression level (%)
400
300
200
100
0
P14
3 Mon
****
Grin1
Grin2d
c
In cerebellum
Grin2d f/f
Nestin-cre:Grin2d f/f
GluN2D
Tubulin
GluN2D expression level (%)
150
100
50
0
P0
P60
P0
d
In SMC
SMA-creER:Ai47
SMA-creER:Ai47:Grin2d f/f
200
0.0288
e
In cortex lysates
SMA-creER:Grin2d f/f (Grin2d-cKO)
ns

a

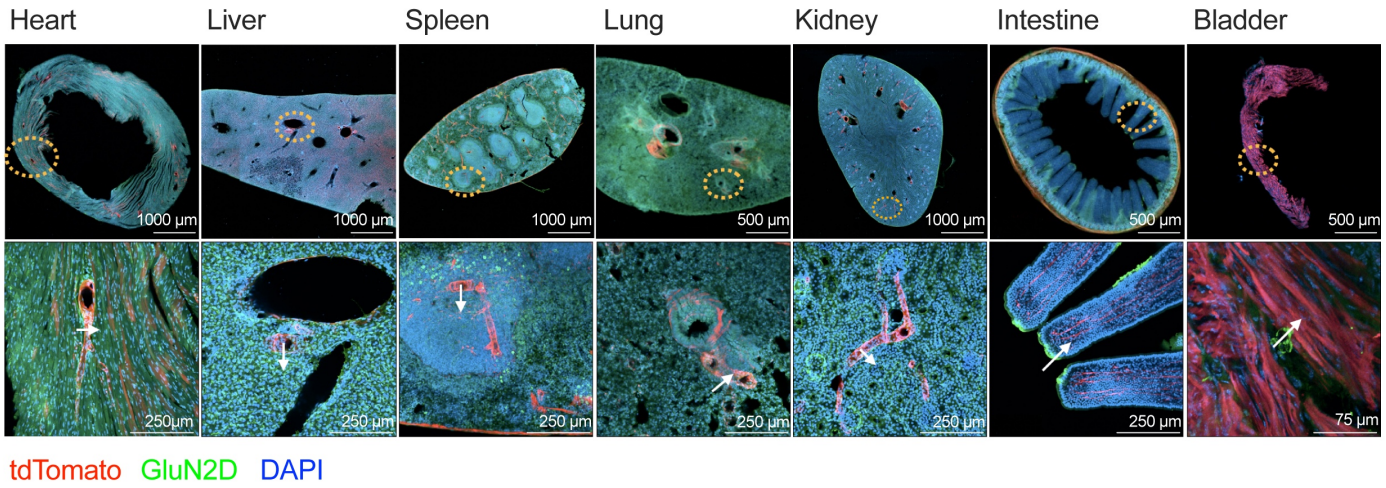
Heart
Liver
Spleen
Lung
Kidney
Intestine
Bladder
1000 μm
1000 μm
1000 μm
500 μm
1000 μm
500 μm
500 μm
250μm
250 μm
250 μm
250 μm
250 μm
250 μm
75 μm
tdTomato GluN2D DAPI

b

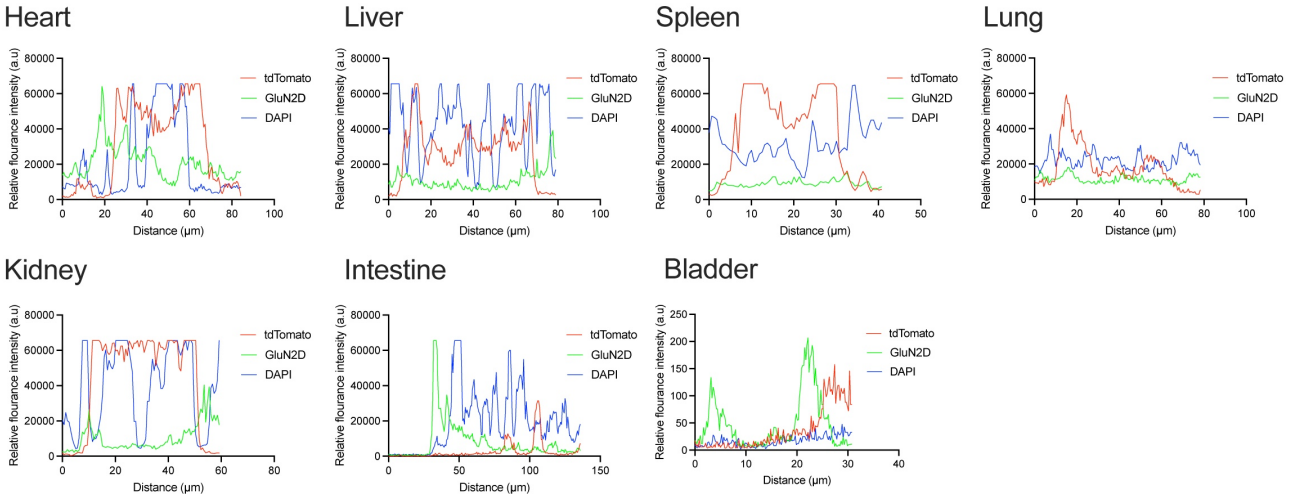
Heart
Liver
Spleen
Lung
Kidney
Intestine
Bladder
Relative flourance intensity (a.u)
Distance (μm)
tdTomato
GluN2D
DAPI

c

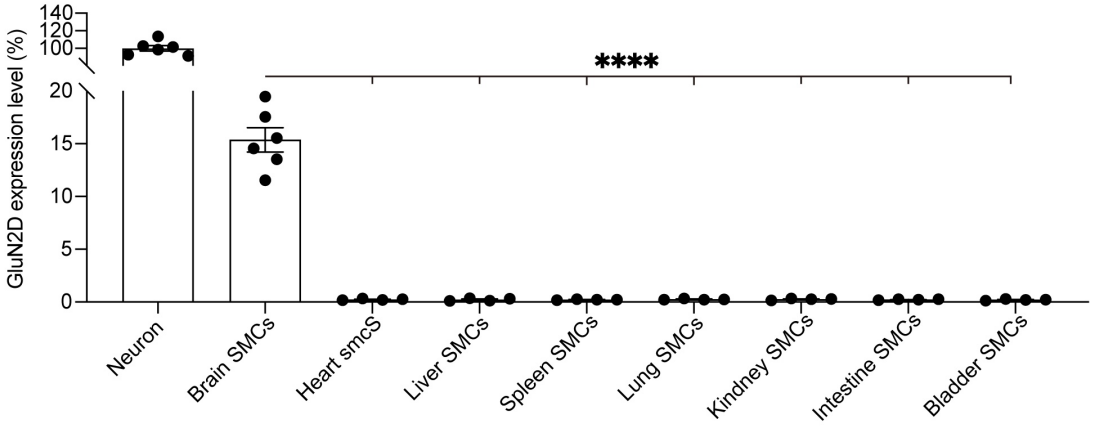
GluN2D expression level (%)
****
Neuron
Brain SMCs
Heart smcS
Liver SMCs
Spleen SMCs
Lung SMCs
Kindney SMCs
Intestine SMCs
Bladder SMCs

Revised Figure S3

Ruan et al.

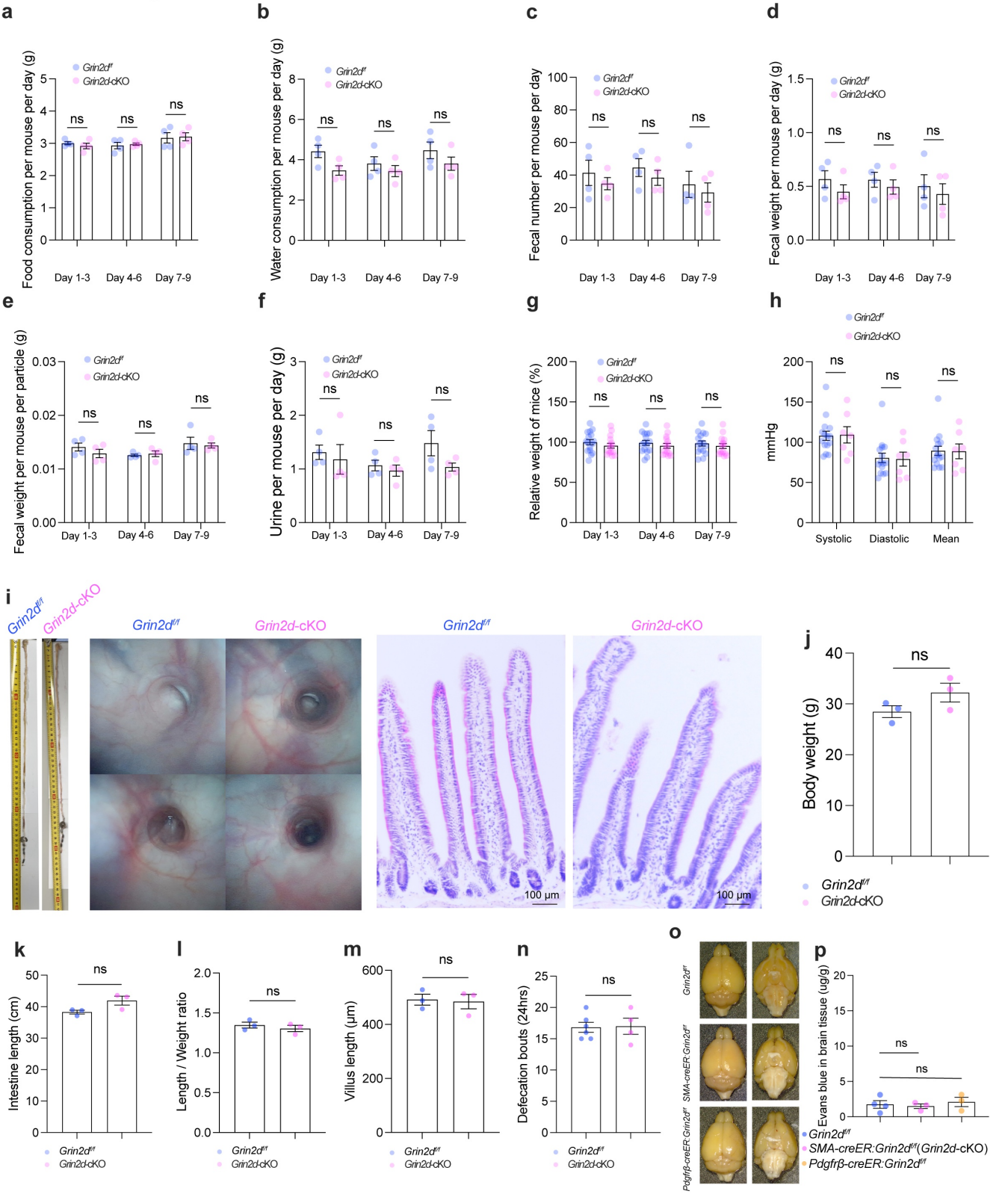

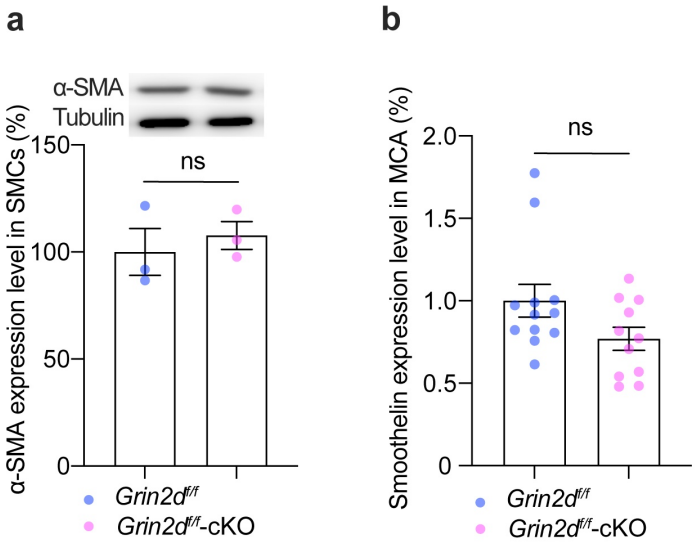
a
α-SMA
Tubulin
α-SMA expression level in SMCs (%)
150
100
50
0
ns
Grin2d f/f
Grin2d f/f-cKO
b
Smoothelin expression level in MCA (%)
2.0
1.5
1.0
0.5
0
ns
Grin2d f/f
Grin2d f/f-cKO

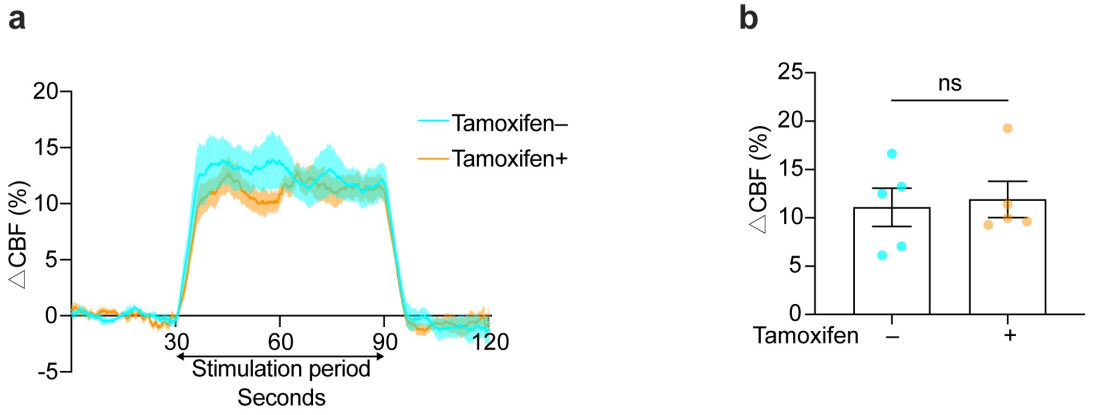
a
20
15
10
5
0
-5
△CBF (%)
Tamoxifen–
Tamoxifen+
30
60
90
120
Stimulation period
Seconds
b
25
20
15
10
5
0
△CBF (%)
ns
Tamoxifen
–
+

a

Ventral view

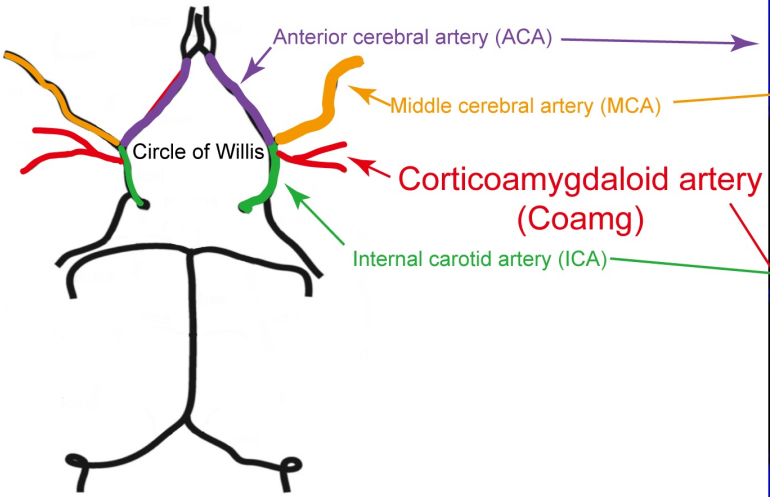

Ventral view
A single hemisphere

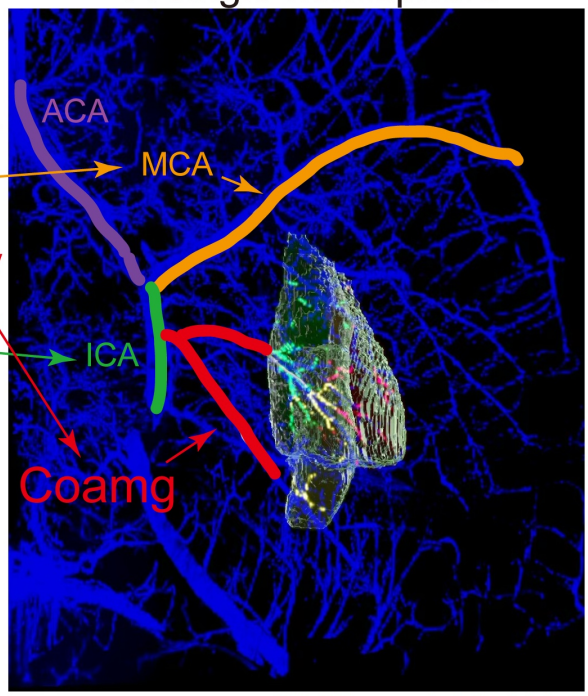

SMA-creER:Ai14

b

Coronal view (from the anterior side)

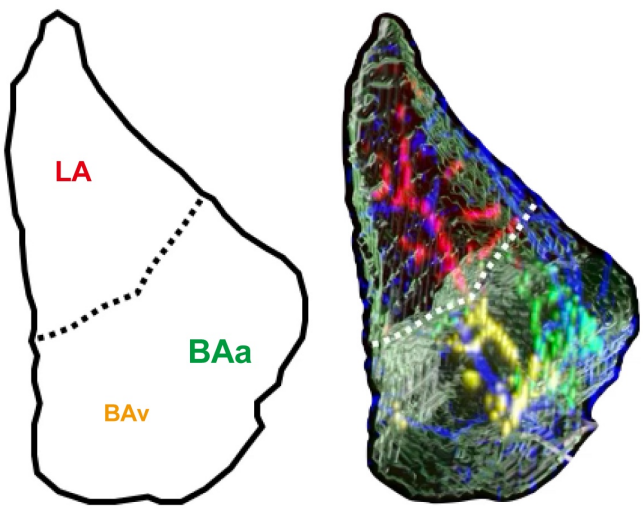

Revised Figure S7

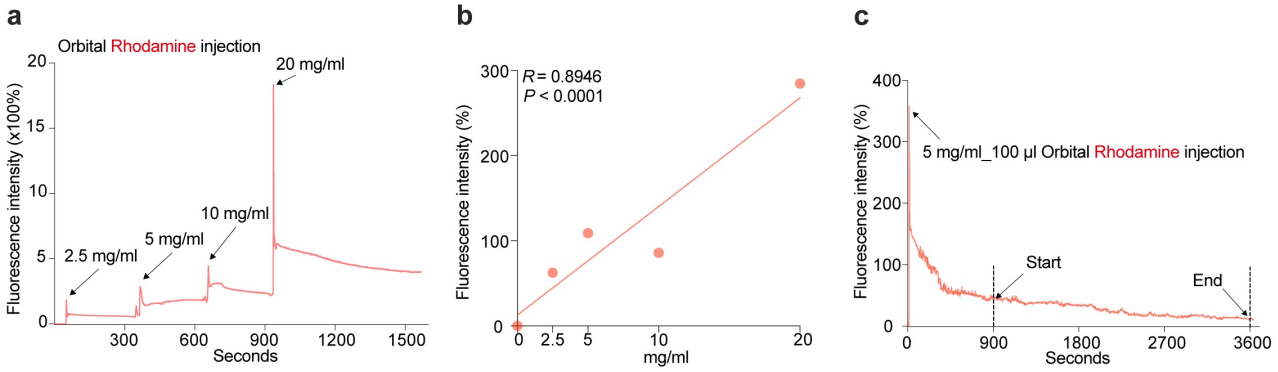

Revised Figure S8

Ruan et al.

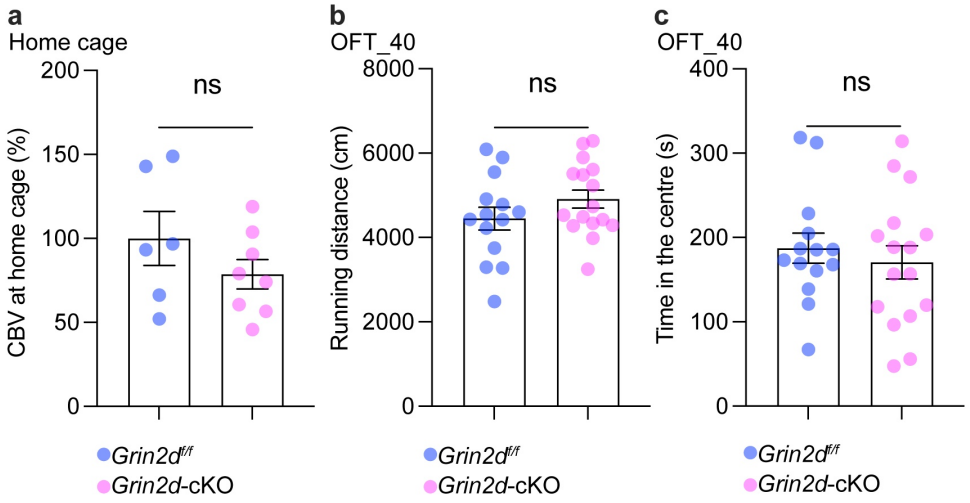

Revised Figure S9

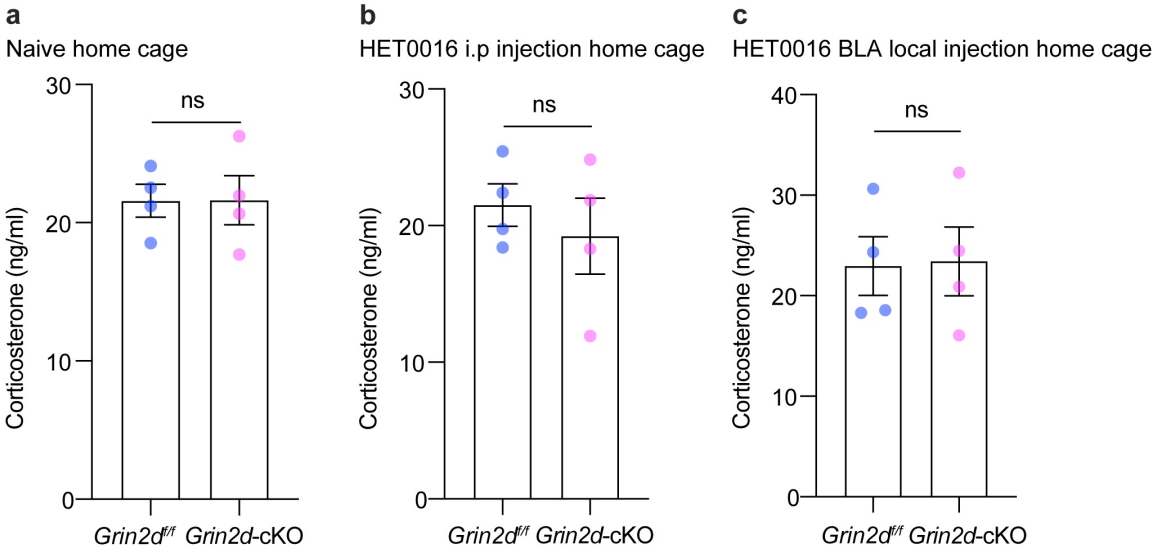

Revised Figure S10

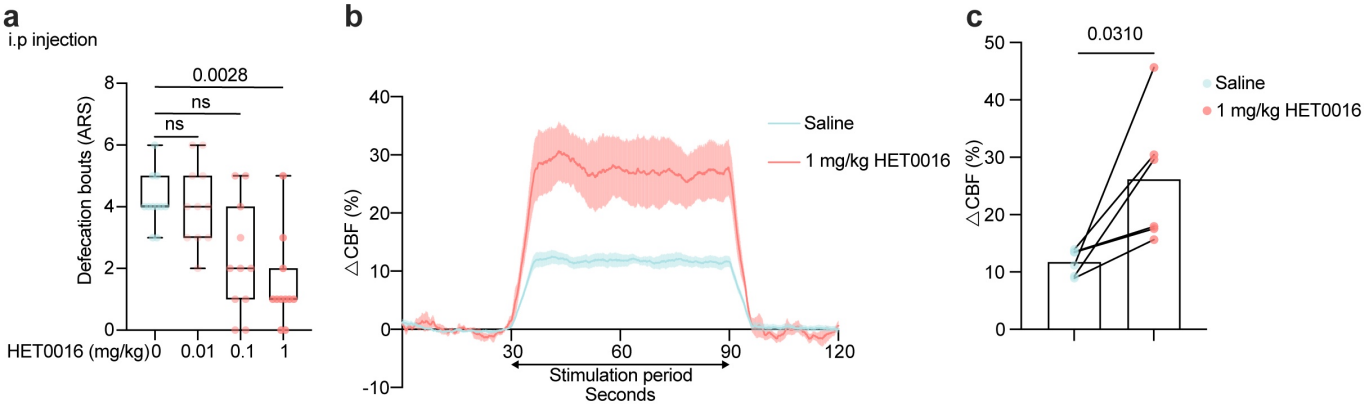

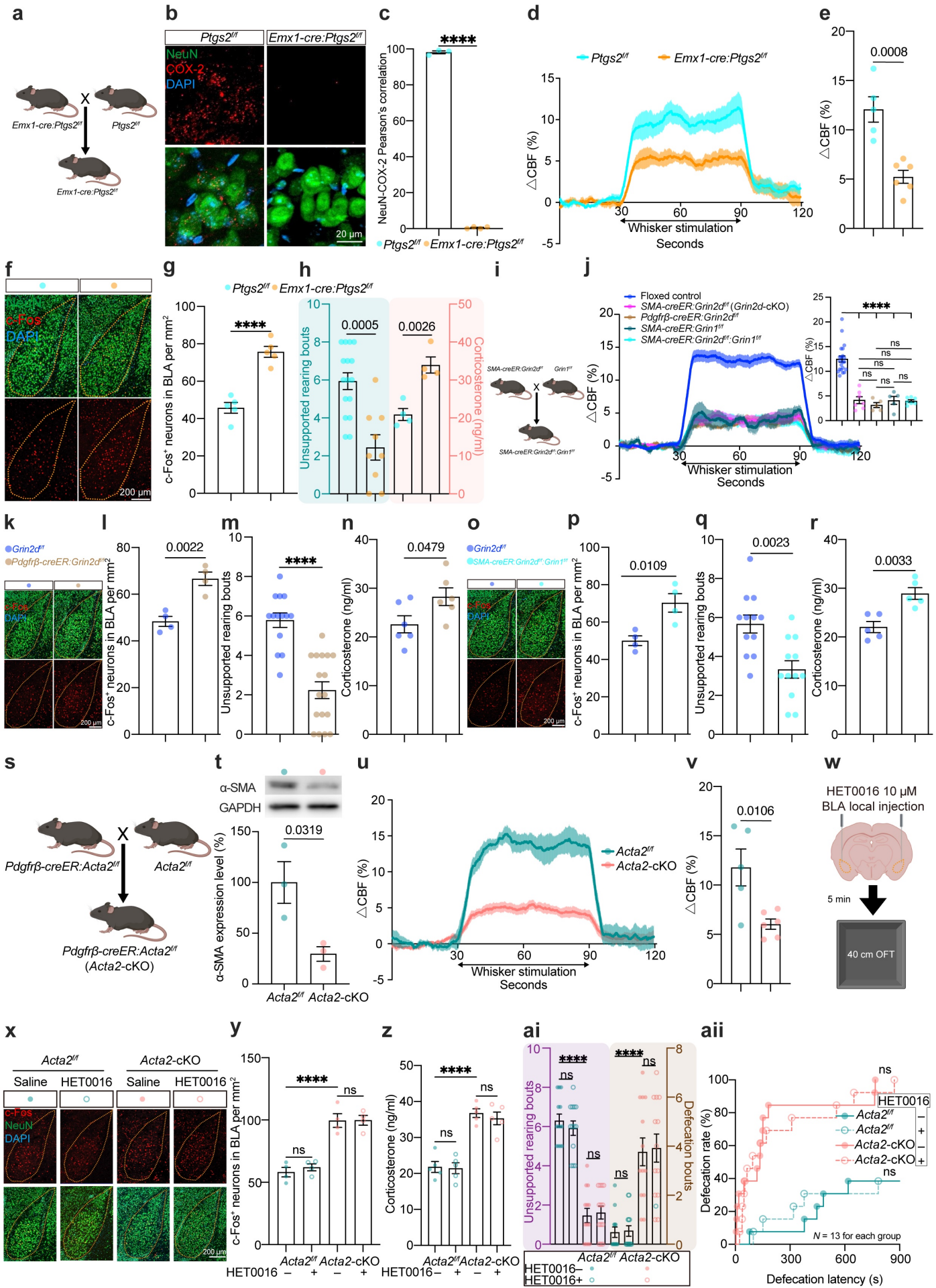
a
Emx1-cre:Ptgs2f/f
Ptgs2f/f
Emx1-cre:Ptgs2f/f
b
Ptgs2f/f
Emx1-cre:Ptgs2f/f
NeuN
COX-2
DAPI
20 μm
c
****
NeuN-COX-2 Pearson's correlation
Ptgs2f/f
Emx1-cre:Ptgs2f/f
d
Ptgs2f/f
Emx1-cre:Ptgs2f/f
△CBF (%)
Whisker stimulation
Seconds
e
0.0008
△CBF (%)
f
c-Fos
DAPI
200 μm
g
Ptgs2f/f
Emx1-cre:Ptgs2f/f
****
c-Fos+ neurons in BLA per mm2
h
0.0005
0.0026
Unsupported rearing bouts
Corticosterone (ng/ml)
i
SMA-creER:Grin2df/f
Grin1f/f
SMA-creER:Grin2df/f:Grin1f/f
j
Floxed control
SMA-creER:Grin2df/f (Grin2d-cKO)
Pdgfrβ-creER:Grin2df/f
SMA-creER:Grin1f/f
SMA-creER:Grin2df/f:Grin1f/f
△CBF (%)
Whisker stimulation
Seconds
****
ns
k
Grin2df/f
Pdgfrβ-creER:Grin2df/f
c-Fos
DAPI
200 μm
l
0.0022
c-Fos+ neurons in BLA per mm2
m
****
Unsupported rearing bouts
n
0.0479
Corticosterone (ng/ml)
o
Grin2df/f
SMA-creER:Grin2df/f:Grin1f/f
p
0.0109
c-Fos+ neurons in BLA per mm2
q
0.0023
Unsupported rearing bouts
r
0.0033
Corticosterone (ng/ml)
s
Pdgfrβ-creER:Acta2f/f
Acta2f/f
Pdgfrβ-creER:Acta2f/f
(Acta2-cKO)
t
α-SMA
GAPDH
0.0319
α-SMA expression level (%)
Acta2f/f
Acta2-cKO
u
Acta2f/f
Acta2-cKO
△CBF (%)
Whisker stimulation
Seconds
v
0.0106
△CBF (%)
w
HET0016 10 μM
BLA local injection
5 min
40 cm OFT
x
Acta2f/f
Acta2-cKO
Saline
HET0016
Saline
HET0016
c-Fos
NeuN
DAPI
200 μm
y
****
ns
c-Fos+ neurons in BLA per mm2
Acta2f/f
Acta2-cKO
HET0016
z
****
ns
Corticosterone (ng/ml)
Acta2f/f
Acta2-cKO
HET0016
ai
****
ns
Unsupported rearing bouts
Defecation bouts
Acta2f/f
Acta2-cKO
HET0016–
HET0016+
aii
HET0016
Acta2f/f
Acta2f/f
Acta2-cKO
Acta2-cKO
ns
Defecation rate (%)
N = 13 for each group
Defecation latency (s)

Revised Figure S12

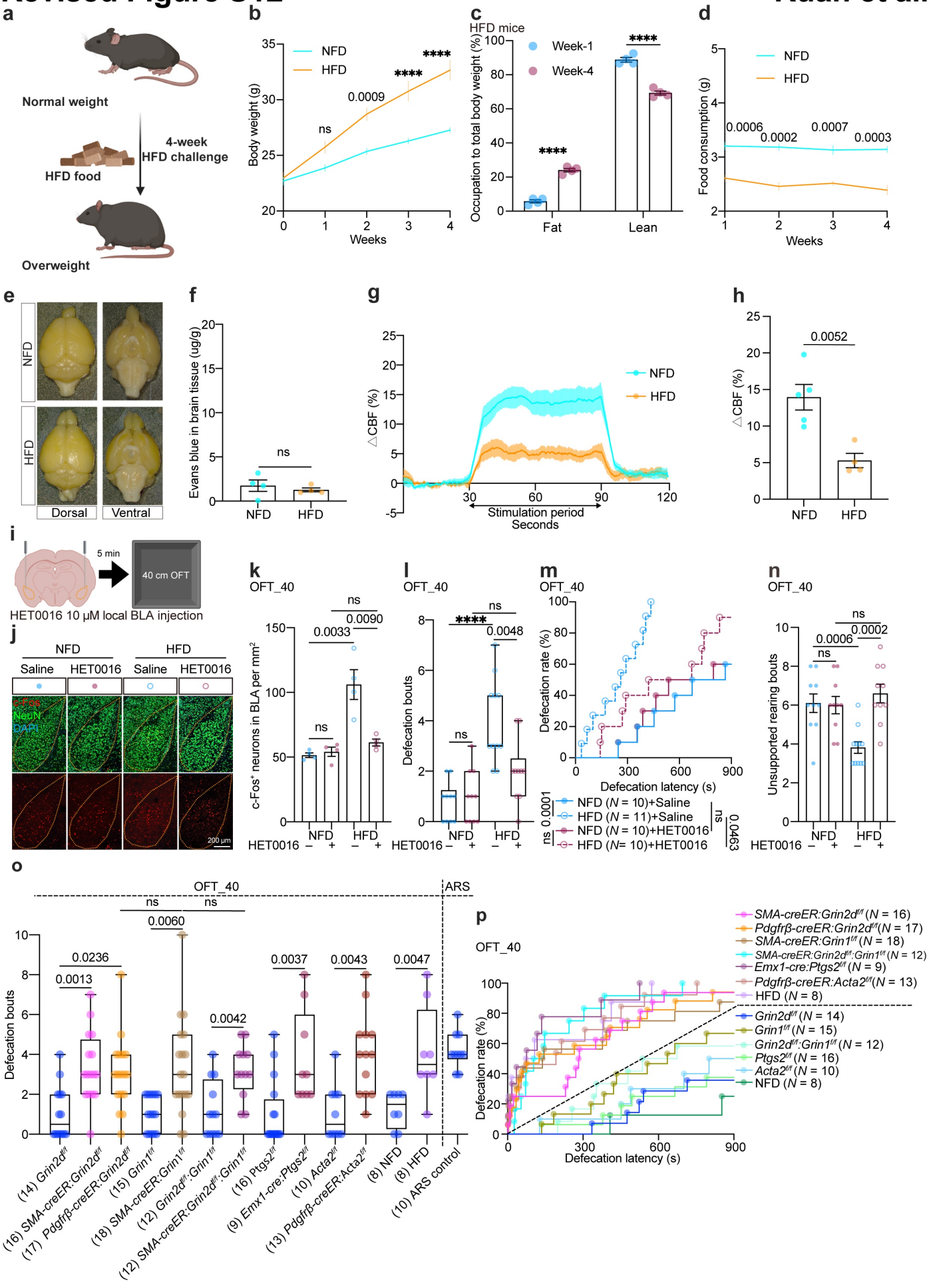

Revised Figure S13

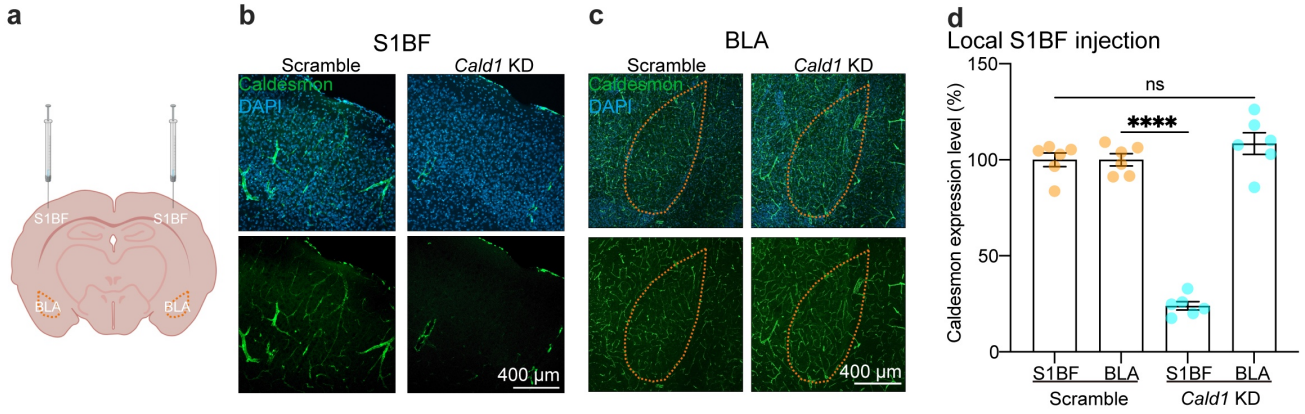

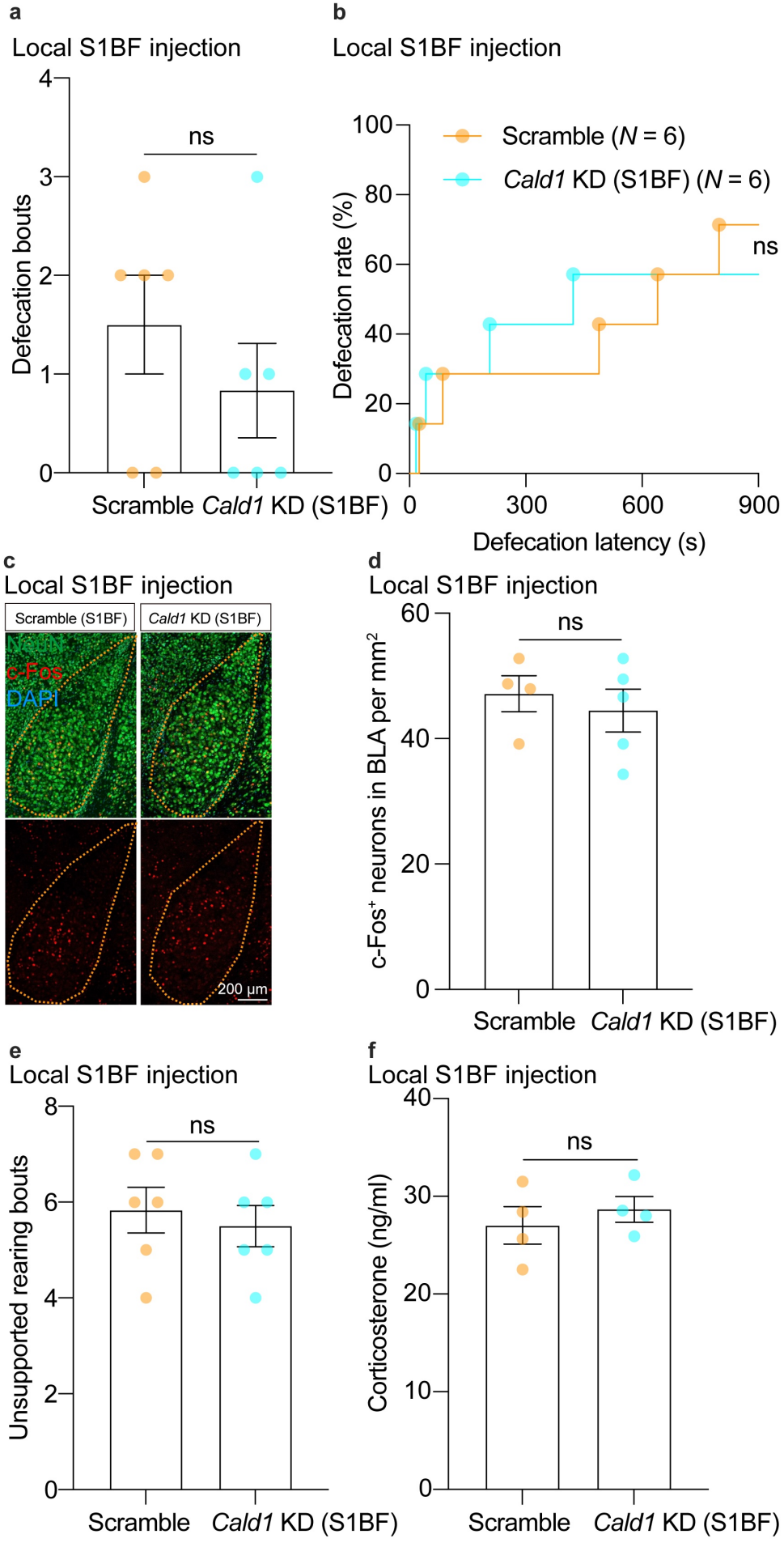
a
Local S1BF injection
Defecation bouts
ns
Scramble
Cald1 KD (S1BF)
b
Local S1BF injection
Defecation rate (%)
Scramble (N = 6)
Cald1 KD (S1BF) (N = 6)
ns
Defecation latency (s)
c
Local S1BF injection
Scramble (S1BF)
Cald1 KD (S1BF)
c-Fos
DAPI
200 μm
d
Local S1BF injection
c-Fos+ neurons in BLA per mm2
ns
Scramble
Cald1 KD (S1BF)
e
Local S1BF injection
Unsupported rearing bouts
ns
Scramble
Cald1 KD (S1BF)
f
Local S1BF injection
Corticosterone (ng/ml)
ns
Scramble
Cald1 KD (S1BF)

Revise Figure S15

Ruan et al.

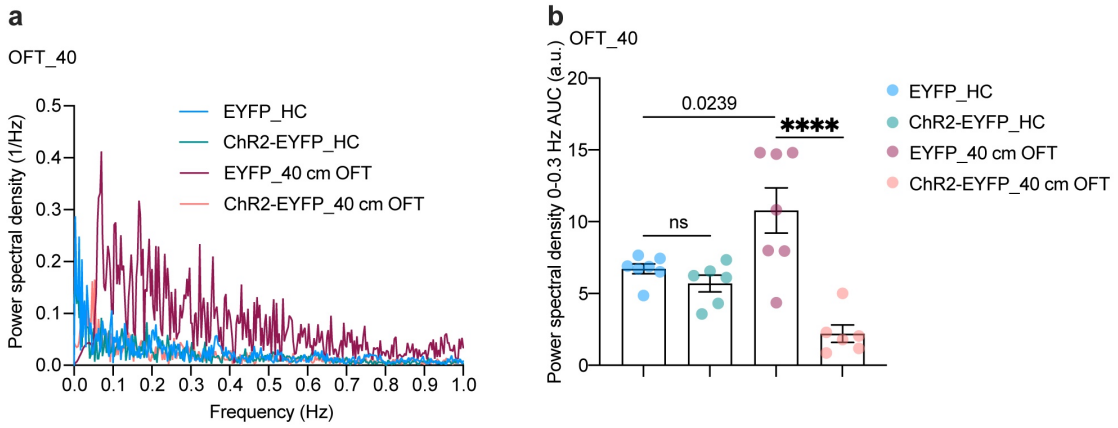

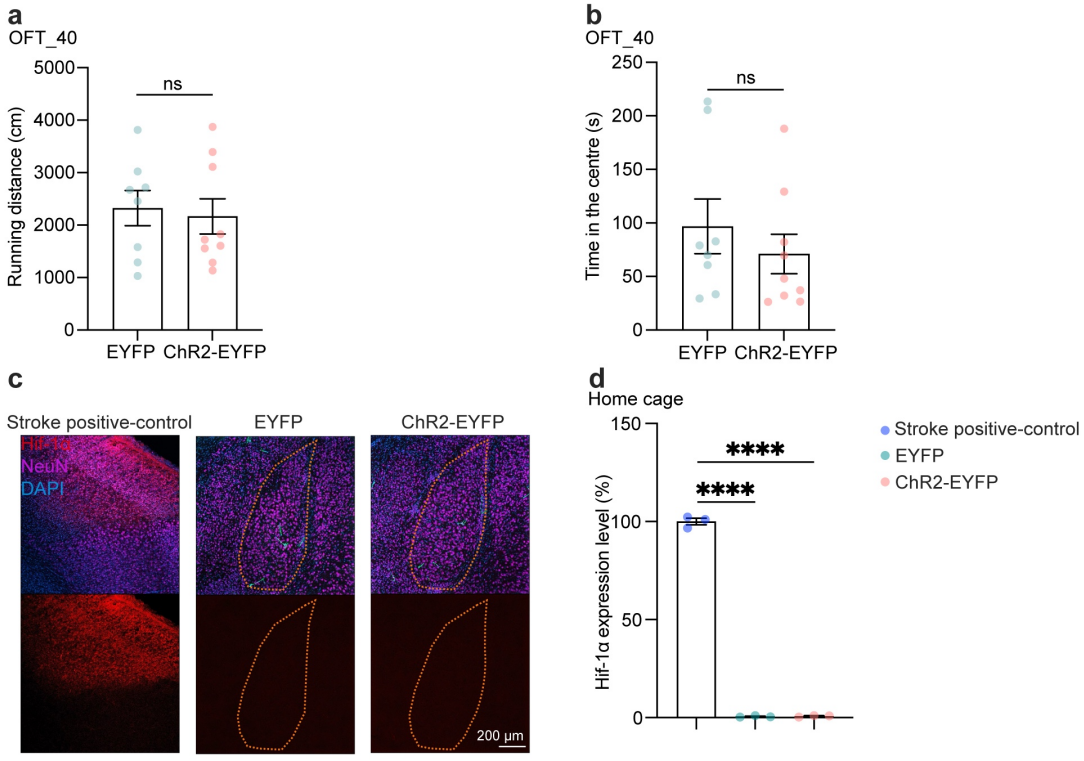
a
OFT_40
Running distance (cm)
5000
4000
3000
2000
1000
0
ns
EYFP
ChR2-EYFP
b
OFT_40
Time in the centre (s)
250
200
150
100
50
0
ns
EYFP
ChR2-EYFP
c
Stroke positive-control
EYFP
ChR2-EYFP
Hif-1α
NeuN
DAPI
200 μm
d
Home cage
Hif-1α expression level (%)
150
100
50
0
****
****
Stroke positive-control
EYFP
ChR2-EYFP

Revised Figure S17

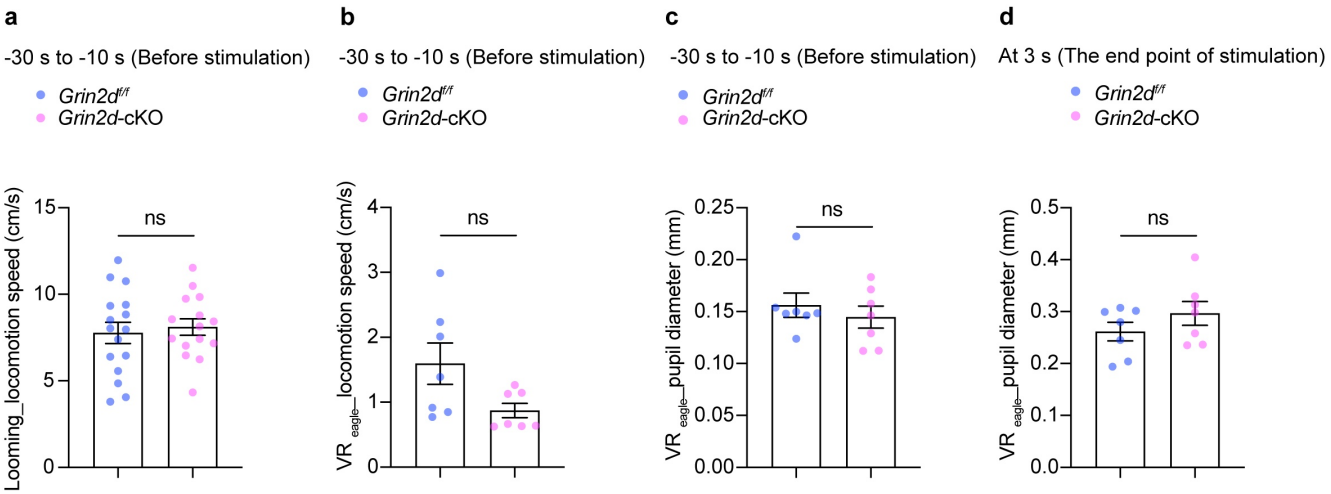

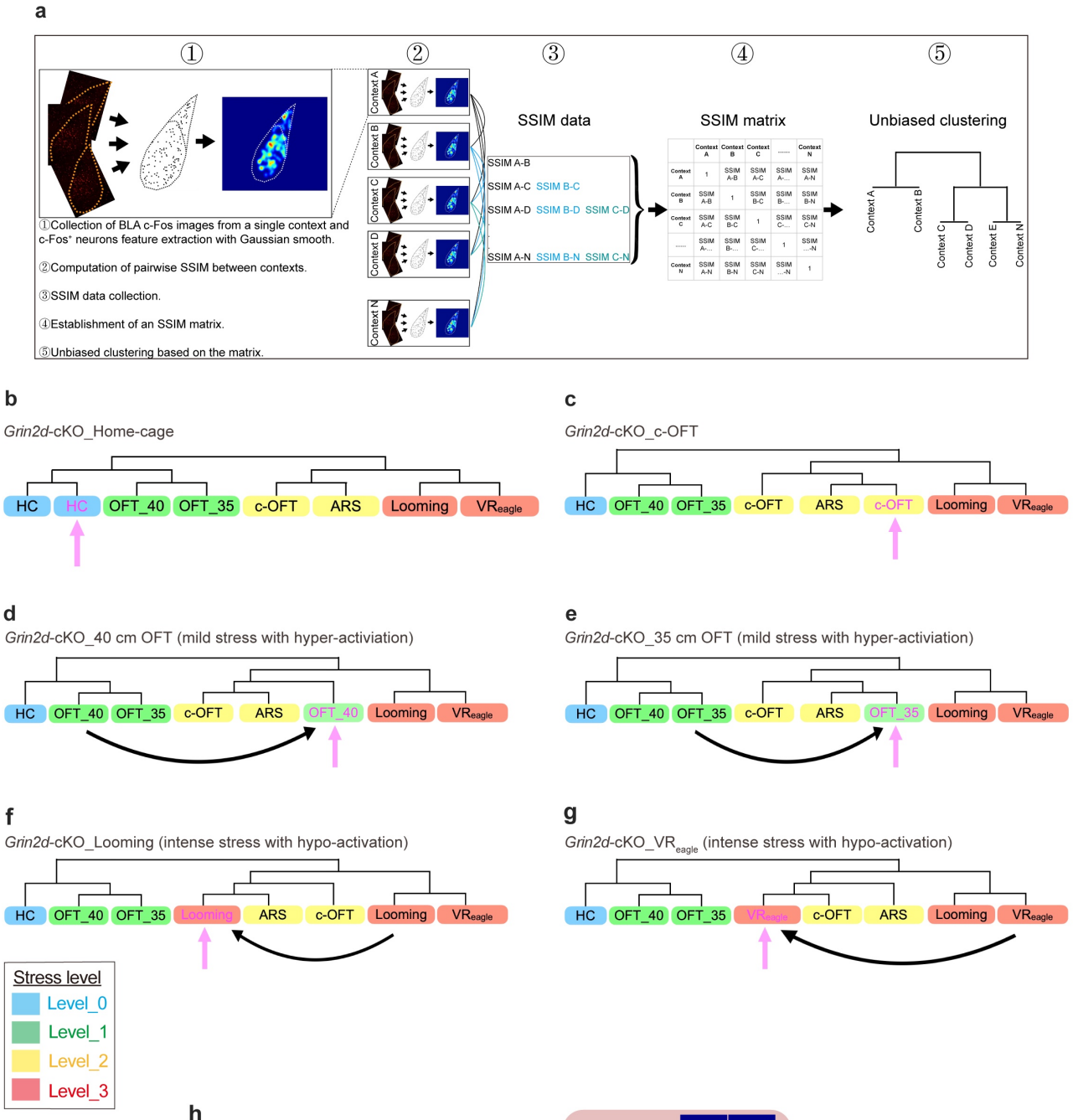
a
①
②
③
④
⑤
SSIM data
SSIM matrix
Unbiased clustering
Context A
Context B
Context C
Context D
Context N
SSIM A-B
SSIM A-C SSIM B-C
SSIM A-D SSIM B-D SSIM C-D
SSIM A-N SSIM B-N SSIM C-N
①Collection of BLA c-Fos images from a single context and c-Fos⁺ neurons feature extraction with Gaussian smooth.
②Computation of pairwise SSIM between contexts.
③SSIM data collection.
④Establishment of an SSIM matrix.
⑤Unbiased clustering based on the matrix.
b
Grin2d-cKO_Home-cage
HC HC OFT_40 OFT_35 c-OFT ARS Looming VReagle
c
Grin2d-cKO_c-OFT
HC OFT_40 OFT_35 c-OFT ARS c-OFT Looming VReagle
d
Grin2d-cKO_40 cm OFT (mild stress with hyper-activiation)
HC OFT_40 OFT_35 c-OFT ARS OFT_40 Looming VReagle
e
Grin2d-cKO_35 cm OFT (mild stress with hyper-activiation)
HC OFT_40 OFT_35 c-OFT ARS OFT_35 Looming VReagle
f
Grin2d-cKO_Looming (intense stress with hypo-activation)
HC OFT_40 OFT_35 Looming ARS c-OFT Looming VReagle
g
Grin2d-cKO_VReagle (intense stress with hypo-activation)
HC OFT_40 OFT_35 VReagle c-OFT ARS Looming VReagle
Stress level
Level_0
Level_1
Level_2
Level_3
h
Grin2d f/f
Grin2d-cKO
c-Fos⁺ neurons in BLA per mm²
800
700
600
500
400
300
200
100
0
Mild stress hyperactivated BLA
Strong stress hypoactivated BLA
p = 0.0017
p = 0.0278
P = 0.0122
P = 0.0123
40
35
OFTs
Looming
VReagle
Predator-like threats

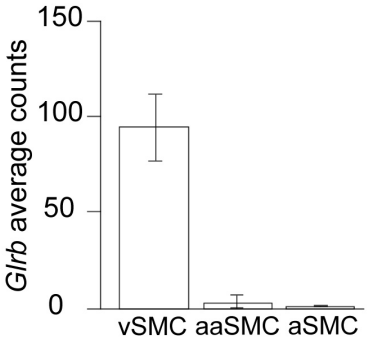

Vanlandewijck et al. Nature (2018)

Revised Figure S20

Ruan et al.

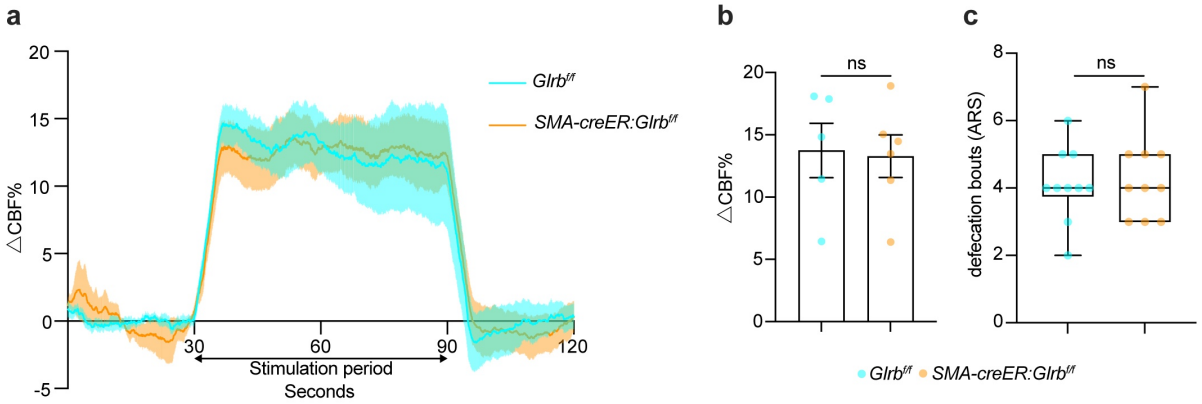

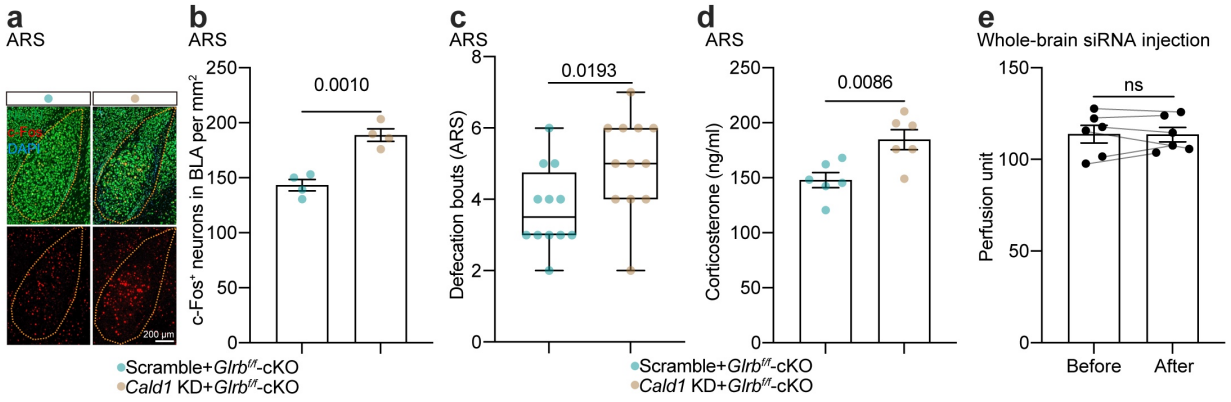
a
ARS
c-Fos
DAPI
200 μm
b
ARS
c-Fos⁺ neurons in BLA per mm²
0.0010
Scramble+Glrb f/f-cKO
Cald1 KD+Glrb f/f-cKO
c
ARS
Defecation bouts (ARS)
0.0193
d
ARS
Corticosterone (ng/ml)
0.0086
e
Whole-brain siRNA injection
Perfusion unit
ns
Before
After

Revised Figure S22

Ruan et al.

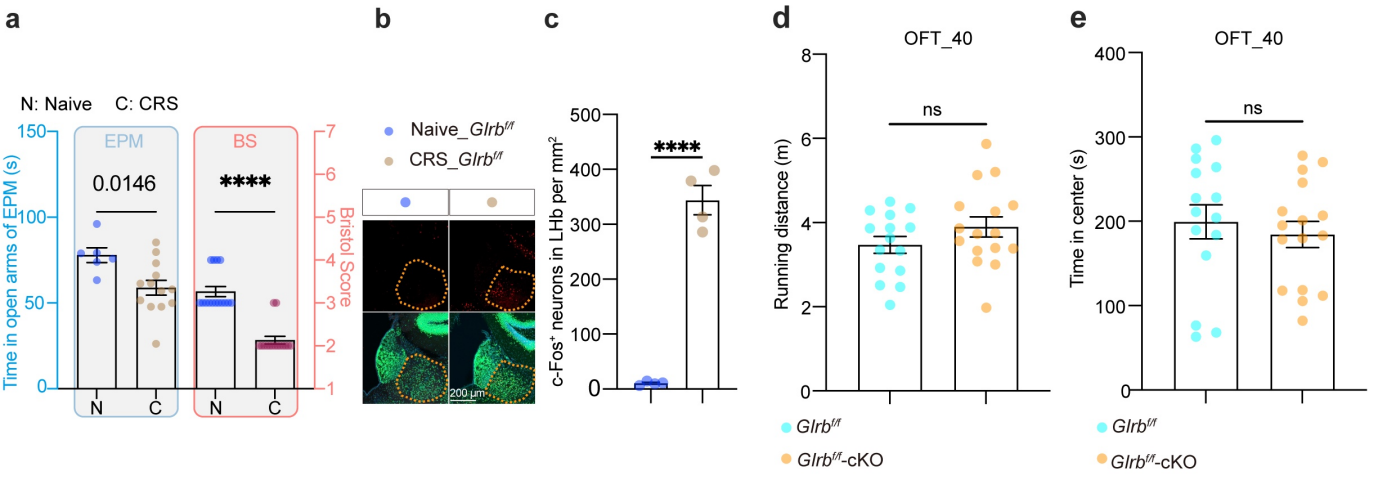

Revised Figure S23

Ruan et al.

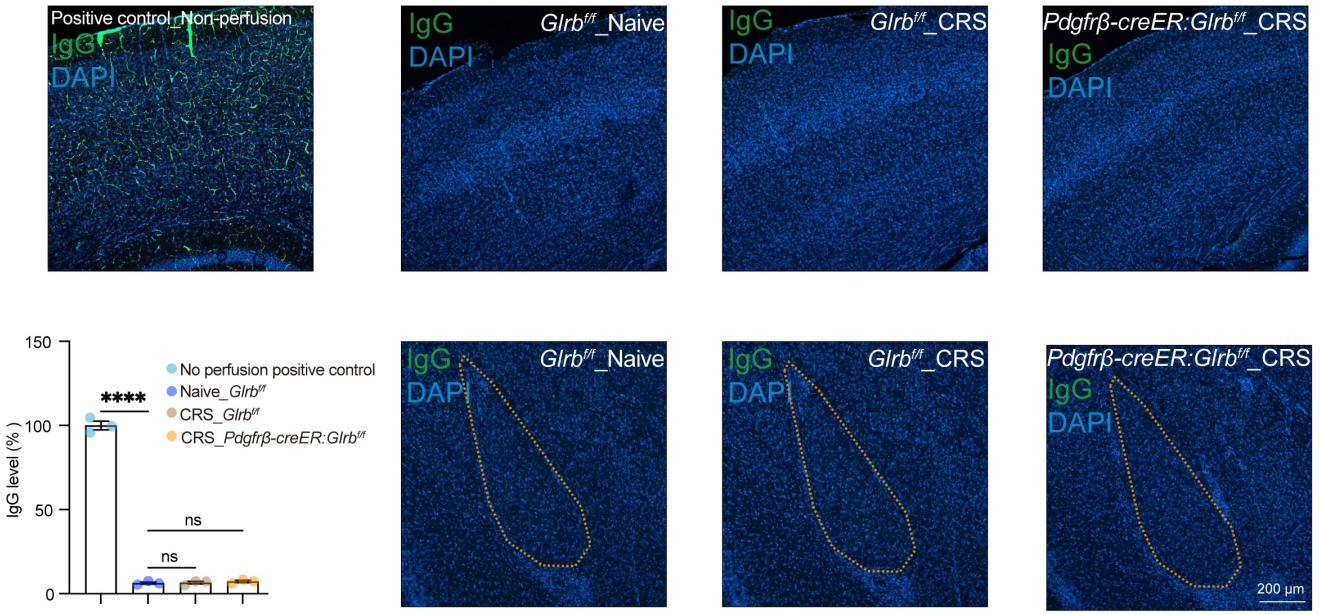

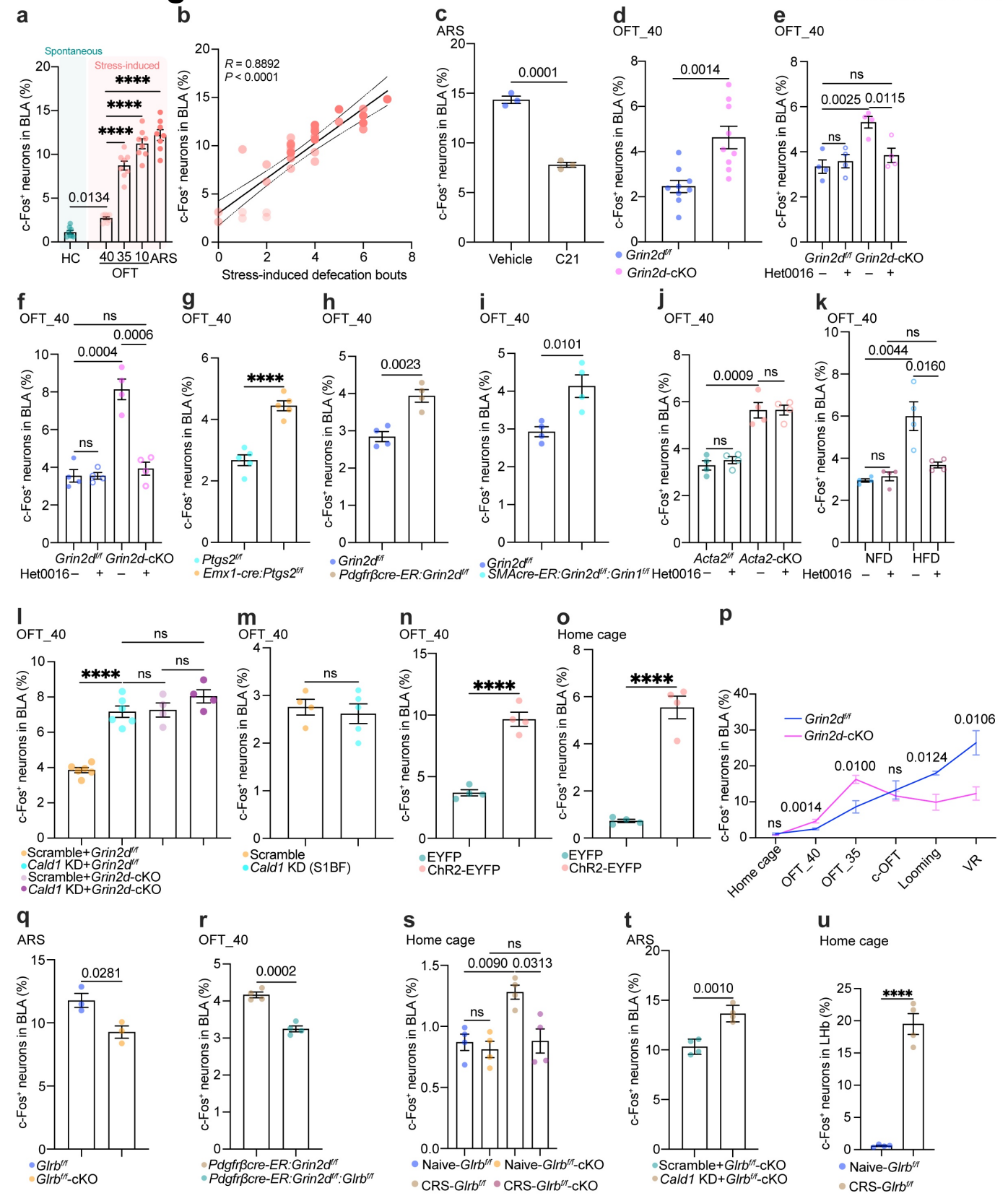
a
Spontaneous
Stress-induced
c-Fos+ neurons in BLA (%)
0.0134
****
HC
40 35 10 ARS
OFT
b
R = 0.8892
P < 0.0001
Stress-induced defecation bouts
c
ARS
0.0001
Vehicle
C21
d
OFT_40
0.0014
Grin2df/f
Grin2d-cKO
e
OFT_40
ns
0.0025
0.0115
Grin2df/f Grin2d-cKO
Het0016
f
OFT_40
0.0004
0.0006
Grin2df/f Grin2d-cKO
g
OFT_40
Ptgs2f/f
Emx1-cre:Ptgs2f/f
h
OFT_40
0.0023
Grin2df/f
Pdgfrβcre-ER:Grin2df/f
i
OFT_40
0.0101
Grin2df/f
SMAcre-ER:Grin2df/f:Grin1f/f
j
OFT_40
0.0009
Acta2f/f Acta2-cKO
k
OFT_40
0.0044
0.0160
NFD HFD
l
OFT_40
Scramble+Grin2df/f
Cald1 KD+Grin2df/f
Scramble+Grin2d-cKO
Cald1 KD+Grin2d-cKO
m
OFT_40
Scramble
Cald1 KD (S1BF)
n
OFT_40
EYFP
ChR2-EYFP
o
Home cage
p
Grin2df/f
Grin2d-cKO
0.0014
0.0100
0.0124
0.0106
Home cage
OFT_40
OFT_35
c-OFT
Looming
VR
q
ARS
0.0281
Glrbf/f
Glrbf/f-cKO
r
OFT_40
0.0002
Pdgfrβcre-ER:Grin2df/f
Pdgfrβcre-ER:Grin2df/f:Glrbf/f
s
Home cage
0.0090
0.0313
Naive-Glrbf/f
Naive-Glrbf/f-cKO
CRS-Glrbf/f
CRS-Glrbf/f-cKO
t
ARS
0.0010
Scramble+Glrbf/f-cKO
Cald1 KD+Glrbf/f-cKO
u
Home cage
c-Fos+ neurons in LHb (%)
Naive-Glrbf/f
CRS-Glrbf/f